Dark Matter
Signatures and Future Detection

Grothaus, Philipp

Awarding institution:
King's College London

Dark Matter:
Signatures and Future Detection

Author:

Philipp Grothaus

Supervisor:

Dr. Malcolm Fairbairn

A thesis submitted for the degree of Doctor of Philosophy

in the

Theoretical Particle Physics and Cosmology Group

Physics Department, King's College London

January 2016

Declaration of Authorship

I, Philipp Grothaus, declare that this thesis titled, 'Dark Matter: Signatures and Future Detection' and the work presented in it are my own. I confirm that:

- This work was done wholly or mainly while in candidature for a research degree at this University.
- Where any part of this thesis has previously been submitted for a degree or any other qualification at this University or any other institution, this has been clearly stated.
- Where I have consulted the published work of others, this is always clearly attributed.
- Where I have quoted from the work of others, the source is always given. With the exception of such quotations, this thesis is entirely my own work.
- I have acknowledged all main sources of help.
- Where the thesis is based on work done by myself jointly with others, I have made clear exactly what was done by others and what I have contributed myself.

Signed:

Date:

Abstract

Signatures of dark matter can be manifold. In the framework of weakly interacting massive particles they can come from annihilations in dark matter rich regions, from collisions of dark matter particles in terrestrial direct search experiments or from production of dark matter at particle accelerators. This thesis focuses on the latter two possibilities.

In the context of collider signatures, we discuss how deviations from background expectations can be interpreted in dark matter models. We look at two examples. First, we see how anomalies in searches for Supersymmetry point towards specific mass spectra in the Minimal Supersymmetric Standard Model (MSSM) at the example of a slight dilepton excess observed by CMS. These spectra are then constrained further by taking complementary analyses into account via a recasting of their limits. This recasting is necessary, because limits on the MSSM spectrum are strongly model dependent. Second, we investigate how deviations in the Higgs to diphoton decay rate can be explained by new vector-like leptons. As we will show, this model not only provides a valid dark matter candidate, but simultaneously leads to a strong first order electroweak phase transition that is necessary for the generation of the observed baryon asymmetry in electroweak baryogenesis scenarios.

Future direct dark matter experiments will be challenged by an irreducible background coming from coherent neutrino-nucleus elastic scattering events that mimic dark matter collisions. This creates a lower limit on accessible dark matter-nucleon cross sections. We show that information coming from the direction of the recoiling nucleus can serve as a strong discriminator between neutrino and dark matter events such that this neutrino bound can be avoided. Necessary exposures of directional searches to surpass this limit are computed.

Contents

List of Figures

List of Tables

Acknowledgements

Writing this dissertation, and especially performing the research that went into it, would not have been possible without the help of many people during the last three years.

Malcolm Fairbairn has been a great supervisor, and has found a good balance between giving me the freedom to perform research independently and develop my own ideas, and checking on me regularly to keep me on track such that the things get done and I don't get lost in the details.

The research itself would not have been possible without the help of my collaborators. These include, of course, Malcolm, who was part of all my publications, Robert Hogan, who has suffered greatly trying to get the Higgs to inflate the Universe, Jocelyn Monroe, who has made sure that we do not lose track of reality when it comes to detector performances, as well as Kazuki Sakurai and Seng Pei Liew with whom I have chased many and lost a few ambulances.

I thank the department as a whole to give me the opportunity to do my PhD at King's in the first place and in this context specifically John Ellis. I am grateful for the opportunities that I had to attend the ICTP summer school in Trieste and international conferences in Italy and Poland as well as many meetings in the UK, such as the Annual Theory Meeting in Durham or the Higgs Workshop in Edinburgh. Also, having free dinners in the last week of a PhD is extremely useful. I also thank the NMS school, the IOP and Daniel Snowden-Ifft making it possible for me to attend the Cygnus2015 conference in L.A.

My examiners, Céline M. Boehm and Frank F. Deppisch, I would like to thank for the thorough and constructive examination and the suggested amendments for the thesis.

I truly enjoyed the three years at King's especially because of the many friendships that have developed over the years. Without the good atmosphere between us PhD

students the work would have been much harder. I will keep the lunch breaks, drinks, poker nights, parties and so on in very good memory.
At this point, I want to thank Robert, Kathy, Chakrit, John, Krzysztof, Tevong and Kazuki for proof reading this dissertation.

For being such a stable backbone in my life, always supportive and understanding, I thank my family. I am relying a lot on your support and am very lucky with you. I am looking forward to get to know the new individual soon.

And, finally, Valeria, you have added even more stability and enjoyment to my life and made this past year in London the best one. I am very happy to have met you and that we share so much time together. This year was only possible because you changed your plans completely last summer and for that, and everything else, I am extremely thankful.

Chapter 1

Introduction

Since the early 20th century physicists have debated the nature of dark matter (DM). Indirect evidence can be found in measurements on scales ranging from the galactic all the way up to the cosmological. The elegance of a single solution to all these complementary findings strongly motivates the explanation in terms of a dark matter component and puts its existence beyond any reasonable doubt.

One of the most popular candidates for dark matter is the weakly interacting massive particle (WIMP). The correct dark matter relic abundance can be naturally explained within this framework via a thermal freeze-out mechanism in the early Universe. The fact that this candidate has weak interactions has motivated great experimental effort to constrain its exact properties.

Experiments include searches for the products of dark matter annihilation at the centre of galaxies and attempts to observe dark matter collisions in Earth-based, low-background direct searches, or the production of WIMPs at particle accelerators such as the Large Hadron Collider (LHC). So far, however, no definite signal has been observed and finding dark matter remains a challenge for the future.

Missing dark matter is by no means the only problem left unsolved by the Standard Model (SM). Phenomena such as the baryon asymmetry of the Universe (BAU) and the origin of neutrino masses remain unexplained. In addition, the exact mechanism

of inflation, a possible solution to the flatness and horizon problems of standard Big Bang cosmology, is unknown. The measurement of the Higgs mass at 125 GeV [1, 2] has also intensified the need for an explanation of why the electroweak scale is so much smaller than the Planck scale, the so-called "hierarchy problem".

It is interesting, and perhaps suggestive, that many of these problems have solutions at the electroweak scale and may be directly related to dark matter. This thesis will, on the one hand, describe how deviations in collider searches can help to form and constrain dark matter models and their relations to other electroweak phenomena and, on the other hand, examine future challenges for direct searches and propose potential solutions.

This introductory chapter will explain the evidence for dark matter, describe the freeze-out mechanism and discuss detection methods in greater detail. The problem of the BAU will be introduced along with a solution derived from the electroweak phase transition, electroweak baryogenesis (EWBG). Finally, the Minimal Supersymmetric Standard Model (MSSM) as a solution to the hierarchy problem will be presented.

1.1 Dark Matter

1.1.1 Evidence

Evidence for dark matter exists on various length scales, from galaxies through clusters up to the cosmological scale.

On galactic scales the evidence arises from rotation curves. A rotation curve describes the dependence of the tangential velocity component, v_T, of gas or stars rotating around the galaxy on its distance, r, to the centre. As most of the luminous matter is concentrated in the centre of the galaxy a decrease of v_T as $1/\sqrt{r}$ would be expected if this were the only matter present.

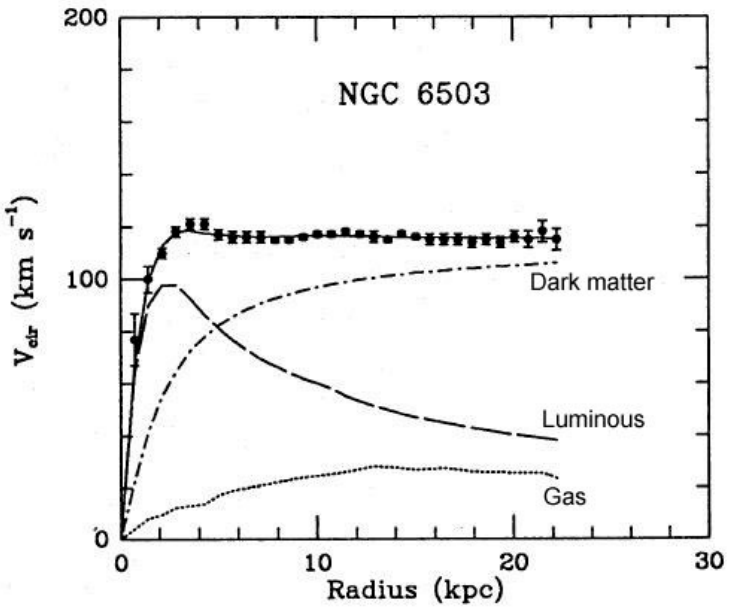

FIGURE 1.1: The rotation curve of galaxy NGC6503 as shown in [4].

However, the actual rotation curves tell a different story. The tangential velocity stays constant at large radii, see e.g. [3, 4]. An example of such a rotation curve is shown in figure 1.1. This behaviour can be explained if we postulate a new component of matter that has a different density distribution compared to the luminous matter. Hence, it is proposed that galaxies are embedded in dark matter halos. Perhaps the most popular density profile for the dark matter distribution is the Navarro-Frenk-White profile (NFW) [5], which was derived from pure cold dark matter (CDM) simulations,

$$\rho_{\mathrm{NFW}}(r) = \frac{\rho_0}{\frac{r}{R_s}(1+\frac{r}{R_s})^2}\,, \tag{1.1}$$

where ρ_0 is a characteristic density and R_s a scale radius. It has to be noted that this profile is not undisputed and some observations suggest a density profile that has a more constant, core-like profile, compare to e.g. [6, 7]. This "core-cusp" problem is an ongoing field of research, but in this thesis the most inner regions of the galaxies will not play a critical role. A possible solution to this problem might be that baryonic feedback expels dark matter from central regions through supernovae [8].

However, galactic rotation curves alone cannot directly tell us anything about the total amount of dark matter that is present in the Universe. To define this dark matter "relic abundance" we turn to the Friedmann equations that govern the expansion rate, H, of the Universe [9].

$$H^2 = \frac{8\pi G}{3}\rho + \frac{\Lambda}{3} - \frac{k}{a^2} = \frac{8\pi G}{3}\rho_{\mathrm{tot}} - \frac{k}{a^2}\,, \tag{1.2}$$

where a is the scale factor, $H = \dot{a}/a$ the Hubble parameter, ρ the matter and radiation energy density, Λ the cosmological constant, G the gravitational constant and k the curvature. We can define a critical energy density, ρ_{crit}, for which the Universe becomes flat, i.e. $k = 0$, as

$$\rho_{\mathrm{crit}} = \frac{3H^2}{8\pi G}\,. \tag{1.3}$$

Density parameters can then be expressed as ratios with the critical density, e.g. $\Omega_{\mathrm{DM}} = \rho_{\mathrm{DM}}/\rho_{\mathrm{crit}}$.

Measuring the dark matter abundance independently from baryons is not easy and, historically, it was the total matter density that was first constrained. Masses of galaxy clusters can be inferred via the velocity dispersions of the galaxies within. Zwicky used the Virial Theorem to estimate the mass of the Coma Cluster and was the first person to point out a mismatch between visible and total matter in 1933 [10]. These mass-to-light ratios can then be used to estimate the matter density, via

$$\Omega_m = \rho/\rho_c \approx \frac{M}{L} \Big/ \left(\frac{M}{L}\right)_{\mathrm{crit}}\,, \tag{1.4}$$

with the critical mass-to-light ratio, $(\frac{M}{L})_{\mathrm{crit}}$, that takes a value of 1136 ± 138 $h_0 M_\odot/L_\odot$ [11], where h_0 is today's Hubble parameter in units 100 km s^{-1} MPc^{-1} and $M_\odot$ and $L_\odot$ are solar mass and solar luminosity, respectively. Recent measurements have indicated mass-to-light ratios of around 200 $h_0 M_\odot/L_\odot$ that result in $\Omega_m \approx 0.19$, see e.g. [11].

More observational evidence from the cluster scale comes from X-ray measurements

of hot gas. Assuming that the gas is in hydrostatic equilibrium, the gravitational potential that binds it can be inferred and mass-to-light ratios of a few 100 $M_\odot/L_\odot$ are determined that again give $\Omega_m \approx 0.2$, see e.g. [12]. The fact that mass-to-light ratios from both independent techniques are much larger than unity suggests that there must be more mass present than only the visible matter. Additionally, gravitational lensing is used to reproduce the distribution of gravitating matter in clusters and again strongly suggests that there must be a dark component, see e.g. [13]. Similarly, gravitational lensing has also been used to constrain Ω_m to be around 0.2 [14].

Another significant piece of evidence comes from the observation of the Bullet Cluster, two colliding galaxy clusters, that shows a mismatch between the centre of mass of luminous matter, as obtained from X-ray measurements, and the overall centre of mass inferred from gravitational lensing [15]. This implies that there is more gravitating mass than just the luminous matter and also that their properties are different. During the collision, the baryonic matter undergoes scattering processes and loses energy, whereas the other gravitating component seems to be (almost) collisionless, with their centres of mass being more separated relative to the luminous ones. Many of these cluster collisions have been observed by now [16] and may even indicate self-interactions of dark matter [17].

It was shown in 1998 using supernova data that the Universe is undergoing accelerated expansion [18, 19]. Together with the measurements outlined above of Ω_m and results from the Boomerang experiment [20], a flat Universe was the best fit to the data with $\Omega_m = 0.28$ and $\Omega_\Lambda = 0.72$, a Universe that is dominated by a cosmological constant or "dark energy". However, all these measurements could not directly distinguish between dark and luminous matter. For this a complementary measurement is needed that comes from big bang nucleosynthesis (BBN). We will discuss BBN in more detail in section 1.2.1. Briefly, the abundance of light elements such as helium or deuterium depends on the number density of baryons that was present in the early Universe. This is used to constrain the baryon density as $\Omega_b \approx 0.05$ [21], a value much smaller than the previously determined matter

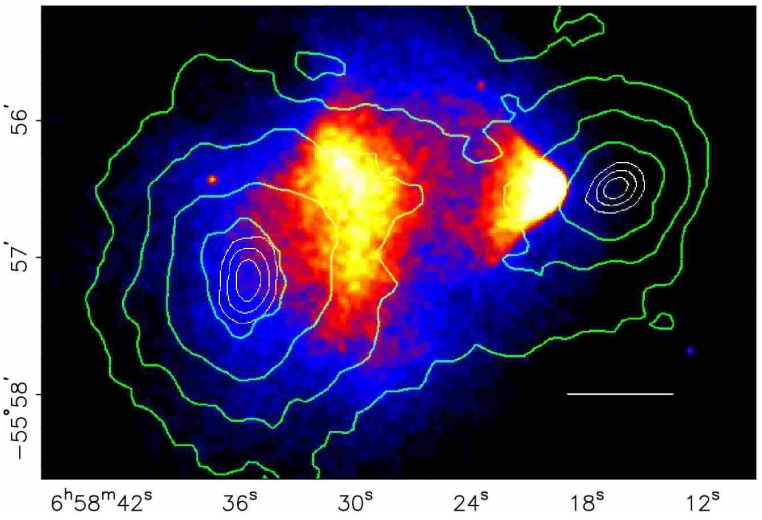

FIGURE 1.2: Bullet Cluster. The colour scale indicates the distribution of visible matter as observed with X-ray data, the green lines follow the distribution of all gravitating matter. Figure taken from [15].

densities. The difference must be in the form of non-baryonic, non-luminous dark matter.

Precise measurements of the cosmic microwave background (CMB) as conducted by the Planck collaboration [22, 23] have confirmed the picture we outlined above. The CMB is an isotropic background radiation with a perfect black-body spectrum at a temperature T = 2.73 K that was generated at the time of recombination. Temperature anisotropies in the CMB are extremely small, at a level of $\frac{\Delta T}{T} \approx 10^{-5}$, but play an important role, because they can be understood as tracing density variations in the very early Universe.

After matter-radiation equality dark matter dominated the energy density of the Universe and collapsed freely on all scales. Baryons and photons, on the other hand, were linked together because of Thomson scattering. The baryon-photon plasma followed the gravitational pull of dark matter overdensities, but at the same time felt thermal pressure such that density oscillations in the plasma occurred. At the time of recombination, when protons and electrons combined into neutral hydrogen and photons freely streamed, this thermal pressure was lost and the baryons traced the density fluctuations of dark matter. It is the temperature pattern of those freely streaming photons that we observe today.

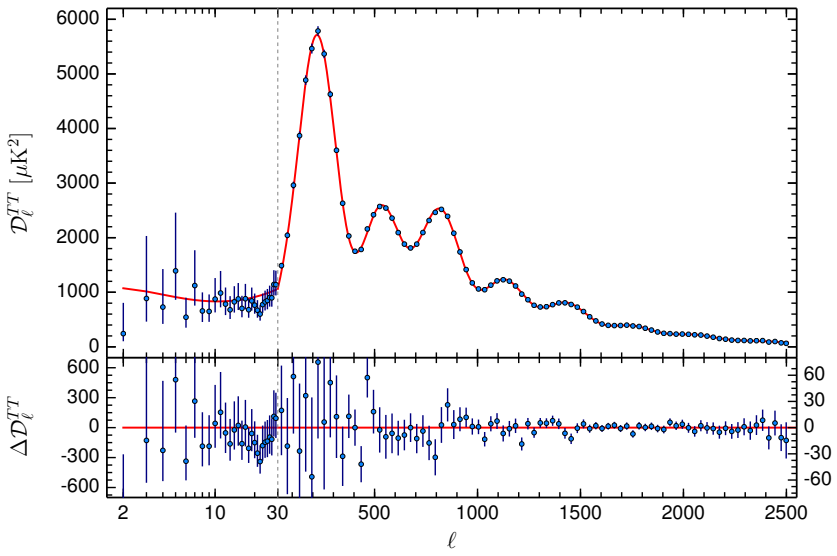

FIGURE 1.3: Temperature power spectrum of the CMB as measured by the PLANCK collaboration [23]. The multipole ℓ is a measure of the angular scale, larger values of ℓ correspond to smaller angular scales.

The temperature power spectrum of the CMB (see figure 1.3) has peaks at different angular scales. These correspond to oscillations in the baryon-photon plasma that, starting when they entered the horizon, reached either maximal or minimal compression at the time of recombination. The heights and locations of these peaks contain crucial information about our Universe and can be used to determine the amount of dark matter, measured to be $\Omega_{\mathrm{DM}}h^2 = 0.1194 \pm 0.0022$ [23], where h is the Hubble parameter in units of 100 km s^{-1} Mpc^{-1}.

All cosmological data can thus be explained in the context of a Universe whose energy density today is dominated by a cosmological constant (Λ) accompanied by a large cold dark matter (CDM) component; this is the so-called "ΛCDM model". Problems such as its flatness and isotropy can be explained dynamically by a theory called "inflation". During the inflationary phase the size of the Universe increased exponentially and the quantum fluctuations of the initial microscopic patch formed seeds for large scale structure formation. The exponential expansion also ensures that scales appearing in opposite directions on the sky now would have been in causal contact at early times.

This concludes our discussion of the evidence for dark matter and how its energy density has been measured. In the next section we will describe the freeze-out mechanism as one example of how this observed relic density can be achieved with electroweak physics.

1.1.2 Relic Density

After discussing the hints for dark matter and how measurements have arrived at $\Omega_{\rm DM}h^2 = 0.1194 \pm 0.0022$, we will present in this section one mechanism that can produce the correct relic density. This mechanism relies on the freeze-out of a non-relativistic species.

In the freeze-out mechanism it is assumed that the dark matter particle, χ, is in thermal equilibrium with other SM particles in the early Universe. Hence, there are both annihilation and creation processes taking place. While the Universe expands and cools, the rate of creation processes will decline because only particles with large enough energies can produce a dark matter particle pair. Annihilation on the other hand is still ongoing such that the number density of dark matter particles, n_χ, drops. At a certain point, the expansion rate of the Universe will be larger than the annihilation rate, Γ, such that annihilations also become extremely rare. Freeze-out occurs and the number density of dark matter drops as a^{-3}.

This qualitative discussion is formulated quantitatively in terms of a Boltzmann equation, see e.g. in [24]

$$\frac{dn_\chi}{dt} + 3Hn_\chi = -\langle\sigma_{\chi\bar{\chi}\to Y\bar{Y}}|v|\rangle[n_\chi^2 - (n_\chi^{EQ})^2] \ . \tag{1.5}$$

Here, $\langle\sigma_{\chi\bar{\chi}\to Y\bar{Y}}|v|\rangle$ is the thermally averaged annihilation cross section and n_χ^{EQ} the equilibrium number density of the non-relativistic dark matter particle, given by

$$n_\chi^{EQ} = g\left(\frac{m_\chi T}{2\pi}\right)^{3/2} e^{-m_\chi/T} \ , \tag{1.6}$$

with T as the temperature, m_χ the dark matter mass and g the number of degrees of freedom of χ. In the Boltzmann equation 1.5 the three effects that govern the behaviour of the number density are visible. There is dilution due to the expansion of the Universe, described by the term $3Hn_\chi$, annihilation processes that are proportional to the number density squared n_χ^2 as well as creation processes from particles in the thermal bath that follow the equilibrium number density n_χ^{EQ}. The temperature at which freeze-out occurs is characterised by $x_F = T_F/m_\chi$.

To find the relic density today equation 1.5 has to be solved numerically, which can be done with the help of open source projects such as micrOMEGAs [25]. It is useful, however, to look at approximate solutions. For GeV scale dark matter today's relic density becomes [26]

$$\Omega_{\mathrm{DM}}h^2 \approx \frac{3 \cdot 10^{-27}\mathrm{cm}^3\mathrm{s}^{-1}}{\langle\sigma v\rangle}\,. \tag{1.7}$$

For a weakly interacting particle one expects $\langle\sigma v\rangle \approx 10^{-26}\mathrm{cm}^3\mathrm{s}^{-1}$ which falls surprisingly close to the needed relic abundance. This is the "miracle" of weakly interacting massive particles and has attracted a lot of attention in DM model building. In equation 1.7 it can also be seen that the larger the annihilation cross section, the smaller the final relic abundance will be, because the freeze-out condition $\Gamma < H$ is fulfilled later, see figure 1.4. It should be noted that the real situation may be more complicated. Co-annihilations, processes in which the DM particle annihilates together with a different particle, have to be included in the calculation and may change the picture.

Other mechanisms to set the correct relic abundance are, for example, the freeze-in mechanism [28] or asymmetric dark matter [29]. The freeze-in mechanism is to some extent the inverse process of freeze-out. Instead of starting with dark matter in thermal equilibrium, it is assumed that the interactions are so weak that dark matter has never been in thermal equilibrium. The relic density grows over time and it grows faster the larger the cross section is. In asymmetric dark matter scenarios the DM particle has an anti-particle. In the original scenario these two

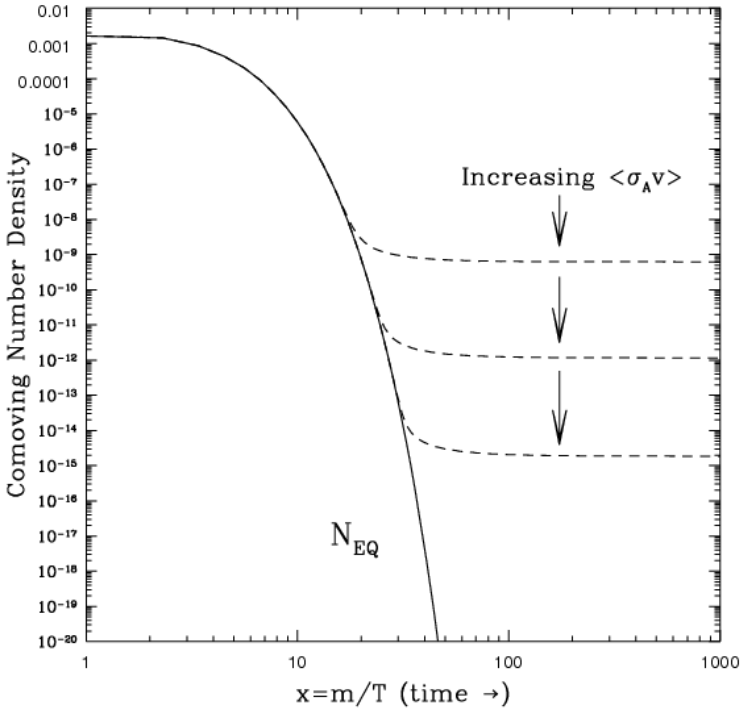

FIGURE 1.4: Dependence of the comoving number density on the thermally averaged annihilation cross section as presented in [27].

annihilate such that the final relic density is set by the asymmetry between them. Since such an asymmetry has to be generated, these models usually try to explain the BAU simultaneously. In this thesis we will use the freeze-out mechanism to set the correct relic abundance of a fermionic dark matter candidate in chapter 3.

After this discussion of how a WIMP produces the correct relic density, we will now present possible methods for its detection.

1.1.3 Detection

In the last section we saw that annihilation processes are crucial within the WIMP paradigm to set the correct relic abundance. Crossing symmetry thus ensures that WIMPs can scatter off SM particles and may also be produced at particle colliders. We will here explain how these three interactions may be used to search for WIMPs.

Indirect dark matter searches look for (decay products of) final states of DM annihilation processes. Since annihilation rates are proportional to the square of the number density, regions like the galactic centre or DM dominated objects such as dwarf spheroidal galaxies (dSphs) form promising regions for these indirect searches. Different experiments look for different final states, as e.g. gamma rays or positrons, and constrain the value of today's DM annihilation cross section.

The Fermi Large Area Telescope (Fermi LAT) has collected six years of data from 15 dSphs and found no significant excess in their data [30]. The sensitivity is so good that annihilation cross sections below the one of the canonical WIMP are tested for pure $b\bar{b}$ and $\tau\bar{\tau}$ final states. One should bear in mind that the thermally averaged cross section today can be very different to that at the time of freeze-out and this indirect constraint has to be evaluated for each model separately, as we will do for our DM candidate in chapter 3.

Intriguingly, an excess of gamma rays originating from the galactic centre has been found in Fermi LAT data [31, 32]. Studies found that this excess can be explained by dark matter annihilating into $b\bar{b}$ or leptons in the mass range of 30-40 GeV or 10 GeV, respectively, see e.g. [33, 34]. Heavier mass ranges up to 76 GeV are possible if DM annihilates first into on-shell particles present in the dark sector that subsequently decay into SM particles [35]. Other studies have suggested that the claimed excess is actually consistent with background expectations and that the leptonic explanation is inconsistent with cosmic ray and radio data [36].

The positron fraction in cosmic rays as observed by the AMS experiment [37] can put strong limits on the annihilation cross section of leptonically decaying dark matter [38, 39]. Again, the canonical WIMP cross section is tested for masses below 200 GeV, if the WIMP annihilates purely into electron/positron pairs. Note that the AMS experiment confirmed an anomalous rise of the positron fraction as first measured by the PAMELA experiment [40]. This excess can also be interpreted in a dark matter framework [41].

Another possibility is to construct Earth-based experiments that measure collisions of DM particles with ordinary matter. These recoils are expected to lie in the keV energy range making detection very challenging. Besides, WIMPs are only weakly interacting such that count rates are expected to be very small, of the order of one event per kg per year depending on detector material and applied energy thresholds. Hence, background rejection is extremely important in these detectors. Whereas current experiments have with great success managed to minimise reducible backgrounds to an extraordinary level, future experiments will inevitably observe coherent neutrino-nucleus elastic scattering, an irreducible background, which will limit their reach [42]. This so-called "neutrino bound" is a problem because WIMP-nucleon cross sections, σ_p, can be suppressed generically in dark matter models. If a mixing angle is present in the dark sector or if destructive interference occurs between different contributions, σ_p may be quite small such that neutrino contamination will play a role. We will present a way to avoid this bound in chapter 4, where we discuss the impact that directional information can have on distinguishing signal from background.

In figure 1.5 we show a summary plot of all currently running or proposed direct detection experiments and the neutrino bound as presented at the Cosmic Frontier Workshop 2013 [43]. Published limits are indicated by a collaboration name accompanied by a year. At the moment, the strongest limits on dark matter-nucleon interaction rates arise from liquid noble element detectors. The LUX (Large Underground Xenon) dark matter experiment published the latest limits in October 2013 [44] indicated in the plot by a light-green dashed line.[1]

At low dark matter masses (around 10 GeV) and WIMP-nucleon cross sections around $10^{-41}\,\mathrm{cm}^2$, many collaborations have claimed the observation of a dark matter signal. The DAMA/LIBRA (Dark Matter/Large Sodium Iodide Bulk for Rare Processes) project has observed an annual modulation signal with the correct phase at 9.3σ [45]. The CoGeNT experiment (Coherent Germanium Neutrino

[1]Note that these are not the current limits, as limits have moved somewhat since 2013, but the change is not significant.

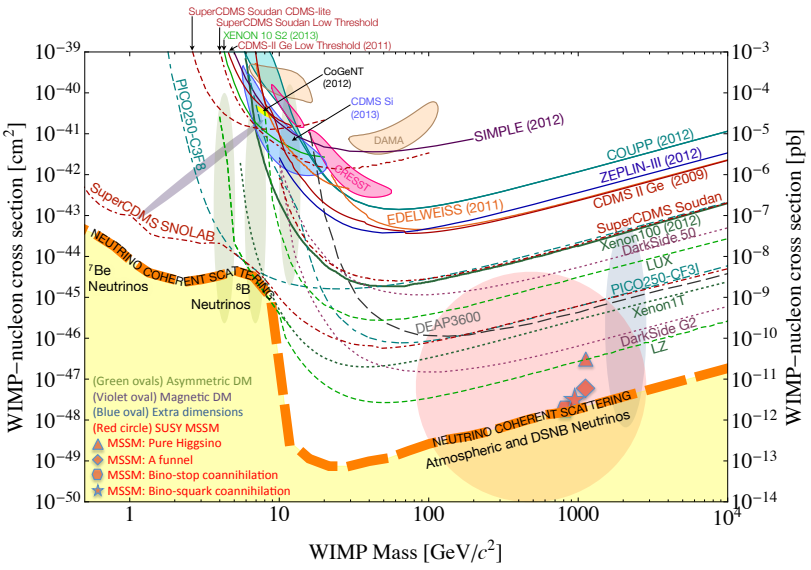

FIGURE 1.5: Summary of past, current and future dark matter direct detection experiments and the neutrino background. Figure taken from [43].

Technology) has observed an excess in the low-energy part of their spectrum that remains unexplained [46], but doubts have risen in the literature about its significance [47]. The CDMS collaboration (Cryogenic Dark Matter Search) has found three candidate WIMP events in their data set with a best fit at $m_{\mathrm{DM}} = 8.6$ GeV and $\sigma_p = 1.9 \times 10^{-41}$ cm^2. All claims are inconsistent with the LUX results, at least in the context of isospin-invariant dark matter models.

A third possibility to detect dark matter is its production at colliders. The typical signal would be events with large missing energy. One such example is mono-jet searches, where initial state radiation of an incoming parton creates a jet that serves as a trigger and, as the final state is completely invisible, large missing energy is present in the event. These searches can be interpreted in a model-independent approach using effective operators [48]. However, care must be taken about the validity of this approach [49].

Mono-jet searches look for a "smoking gun" signal of dark matter production, but the signal rate ultimately depends on the combination of the dark matter mass and

its couplings. It might be that the DM-SM coupling is suppressed such that direct production and, by the same token, direct and indirect searches, are unlikely to yield results.

In such a situation new physics connected to dark matter could instead leave its first traces in accelerators and give insights on the dark matter candidate in a more indirect way. If additional, heavier states are present in the hidden sector their couplings may be less suppressed and lead to deviations from SM predictions in experiments. We discuss in chapter 2 and 3 how deviations in SUSY searches and the Higgs sector may prove to be the first step to find dark matter at a collider.

In this section we summarised possible methods for dark matter detection and outlined how these will be discussed further in this thesis. We will now explain other electroweak phenomena that may be related to dark matter. We start by discussing electroweak baryogenesis.

1.2 Electroweak Baryogenesis

We have discussed previously that there is evidence for a dark matter component in our Universe and that solutions exist at the electroweak scale. However, the SM has several problems. One other problem is that the SM fails to explain why there is matter present at all, or why there is a baryon asymmetry. Any initial asymmetry would, disregarding the necessity of fine-tuning, be diluted by inflation and the hot big bang is expected to produce matter and anti-matter in equal amounts, such that they would mainly annihilate. In addition, sphaleron processes, which we will introduce in section 1.2.3, would destroy any asymmetry until they fall out of equilibrium. The idea of separating matter and anti-matter into different regions would create a diffuse γ-ray background at their interfaces that is not observed. Physicists are thus faced with the need for a dynamical explanation which was first realised by Sakharov in 1967 [50]. Here we will introduce the main idea behind

baryogenesis at the electroweak scale. We start by summarising the experimental evidence for the BAU coming from big bang nucleosynthesis (BBN) and the CMB.

1.2.1 Baryon Asymmetry of the Universe

We define the measure of asymmetry, η, as the ratio between the difference of baryon and anti-baryon number densities and the number density of photons,

$$\eta = \frac{n_B - n_{\bar{B}}}{n_\gamma} \,. \tag{1.8}$$

At late times this measure stays constant, because all three number densities drop as a^{-3}. In early times annihilation of baryons or leptons increased the number density of photons.

The mass fraction, X_A, of a nucleus with atomic number A depends on its binding energy, E_B, and on the baryon number density, thus on η [24], as

$$X_A \propto \eta^{A-1} e^{E_B/T} \,. \tag{1.9}$$

Due to the large entropy of the Universe (which is another way of saying that η is very small) nuclei only bind at temperatures less than a MeV [24]. By that time weak interactions that transformed protons into neutrons and vice-versa have fallen out of equilibrium such that neutrons started to decay into protons. The neutron per proton ratio dropped to a value of about 1/7 when production of helium bound all free neutrons.

The abundances of light elements can serve as a way to constrain η and currently its allowed range is $5.7 \cdot 10^{-10} < \eta < 6.7 \cdot 10^{-10}$ [51]. A complementary measurement can be obtained from the CMB. The temperature power spectrum is sensitive to η with a best fit value of $\eta = 6.047 \pm 0.074$ [22]. The agreement between these two measurements is remarkable given that they are based on completely different physics.

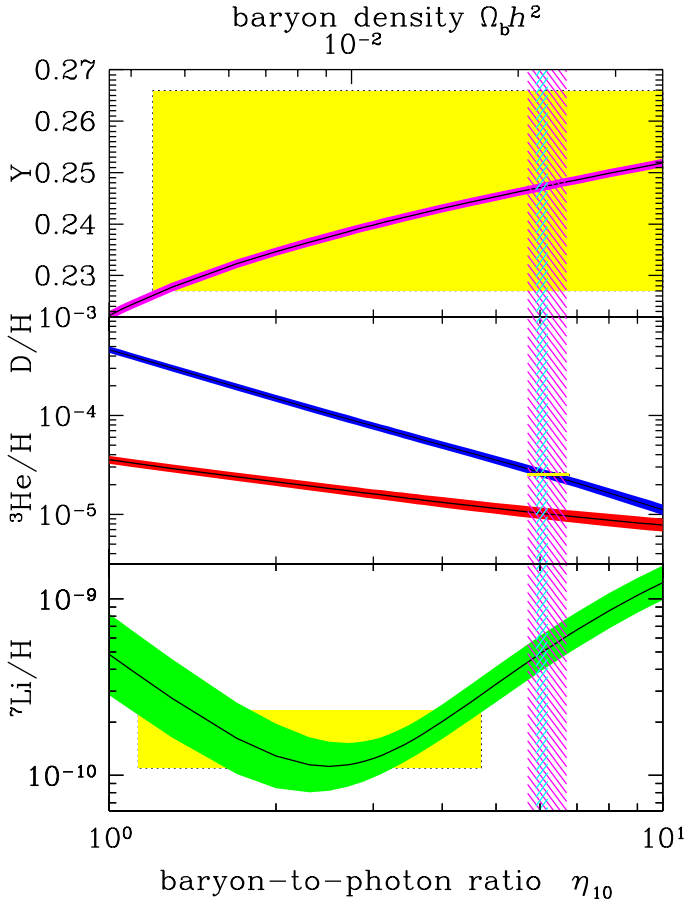

FIGURE 1.6: Dependence of light element abundances on the asymmetry parameter $\eta_{10} = \eta \cdot 10^{10}$ as predicted by BBN. Yellow boxes indicate measurements with their uncertainties. The purple band is the best fit to the measured abundances, the blue band indicates the consistent measurement coming from the CMB, Y is the mass fraction of ^{4}He, as shown in [51].

In figure 1.6 we show the predictions from BBN for the abundances of light nuclei depending on η and their measurements. It is noteworthy that the predictions for the abundances span many orders of magnitude and are still, except for the Lithium abundance, in good agreement with the measurements. The inferred value for η from the CMB is also indicated in the plot. The mismatch of the Lithium abundance is called the "Lithium problem" and has initiated a lot of research, see e.g. [52].

This concludes the discussion on measuring η and in the next section we continue with describing the necessary ingredients of any dynamical solution of the BAU.

1.2.2 Sakharov conditions

In the last section we established that there is a BAU and that there is the need for a dynamical explanation. Here we will present necessary conditions that any solution must fulfil, as described by Sakharov [50]. The three conditions are

(1) B number violation,

(2) C and CP violation,

(3) deviation from thermal equilibrium.

The fact that baryon number (B) violating processes have to occur is rather clear, otherwise no asymmetry can be formed.

Let us assume that there is a B number violating process $X \to Y + B$, i.e. a baryon creating process. If charge symmetry (C) is respected and X and Y are states with zero baryon number, we have $\Gamma(X \to Y + B) = \Gamma(\bar{X} \to \bar{Y} + \bar{B})$, such that the net baryon number is still zero. If furthermore C is violated but CP respected, there will still not be any asymmetry. We can see this if we write a hypothetical process as $X \to q_L + q_L$ and $X \to q_R + q_R$. With charge violation we have $\Gamma(X \to q_L + q_L) \neq \Gamma(\bar{X} \to \bar{q}_L + \bar{q}_L)$, but with CP symmetry we do have $\Gamma(X \to q_L + q_L) = \Gamma(\bar{X} \to \bar{q}_R + \bar{q}_R)$. Hence, all processes together will still result in vanishing baryon number and CP must also be violated.

Lastly, in thermal equilibrium any process has the same rate as its inverse, such that for every process that violates B the inverse reaction will destroy any produced net baryon number.

These are the three Sakharov conditions. We will now investigate if these conditions are fulfilled in the SM.

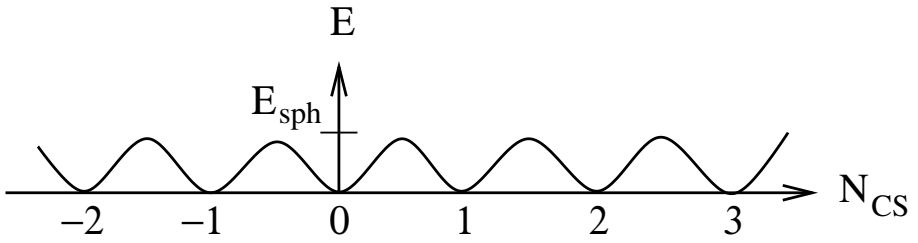

FIGURE 1.7: Visualisation of the different SU(2)-vacua characterised by the Chern-Simons number, N_{CS}, and the energy barrier as shown in [54].

1.2.3 The Standard Model and Baryogenesis

We will now discuss whether the Sakharov conditions that we outlined in the previous section are fulfilled in the SM. In 1976, t'Hooft realised that non-perturbative processes induce baryon number violation in the SM [53]. Two ingredients went into this result.

First, the vacuum structure of SU(2) is non-trivial. There exists an infinite number of pure gauge configurations (gauge configurations of null-fields) with zero energy that cannot be rotated into each other via a series of infinitesimal transformations. These states are characterised by a topological winding number, the Chern-Simons number N_{CS}.[2] Whereas the energy of the individual vacua are zero, intermediate configurations between two vacua have non-zero energy. Hence, there are energy barriers between the states with a height $E_{\text{sph}} \approx 16\pi v/(\sqrt{2}g)$. This is visualised in figure 1.7.

The second ingredient in t'Hoofts argument is the triangle anomaly [55, 56] of the (left-handed) baryon plus lepton current

$$\partial_\mu J^\mu_{B+L} = \frac{3g^2}{32\pi^2}\epsilon_{\alpha\beta\gamma\delta}W_a^{\alpha\beta}W_a^{\gamma\delta}\,. \tag{1.10}$$

He has shown the important result that this anomaly induces a change in baryon and lepton number during a transition between two vacua,

$$\Delta B = \Delta L = n_f \Delta N_{CS}\,, \tag{1.11}$$

[2]The same is true for SU(3) and gives rise to the Θ-term in the QCD Lagrangian.

where n_f is the number of families. Tunnelling processes between the vacua are called "instatons" and would allow for B and L generation. Unfortunately, their amplitude

$$A \propto e^{-16\pi^2/g^2} \propto e^{-173}\,, \tag{1.12}$$

is highly suppressed and they cannot account for the observed BAU. However, Kuzmin, Rubakov and Shaposhnikov showed in 1985 that at finite temperature transitions become unsuppressed [57]. The additional thermal energy can help the field configuration to reach the top of the energy barrier and then fall to an adjacent minima. These configurations are called "sphalerons". Their rate before and after electroweak symmetry breaking (EWSB) is

$$\Gamma \propto \begin{cases} (\alpha_{\rm EW} T)^4 & \text{before EWSB}\,, \\ e^{-E_{\rm sph}/T} & \text{after EWSB}\,. \end{cases} \tag{1.13}$$

Hence, after EWSB sphaleron transitions may be suppressed if $E_{\rm sph}$ is large enough.

Interestingly, the electroweak phase transition (EWPT) now offers a unique opportunity. If the phase transition (PT) is first order, two distinct phases would appear and establish the out-of-equilibrium requirement. Hence, it should be investigated whether the Higgs potential develops a barrier at finite temperatures that separates the two minima. If this is the case, a critical temperature, T_c, can be defined as the temperature at which both minima are degenerate. The order parameter may be defined as the ratio between the vacuum expectation value (vev) of the second minima at T_c, v_c, and the critical temperature, v_c/T_c.

The general idea behind EWBG can be summarised as follows. During the PT the two phases are separated by bubble walls that expand and eventually fill all of space. CP-violating interactions with the bubble walls give different transmission and reflection coefficients for pairs of CP conjugates when they collide with the walls. This leads to an excess of left-handed anti-fermions ($\bar{f}_L$) and right-handed fermions (f_R) in front of the wall and an excess of $\bar{f}_R$ and f_L inside the bubble. After EWSB sphaleron transitions can be suppressed, such that they are inactive inside

the bubble, but still active outside. Because there are relatively more $\bar{f}_L$ than f_L outside the bubble, sphalerons will mainly remove left-handed anti-fermions, such that a positive baryon number is generated. When the bubbles fill all of space, this excess will also enter the broken phase.

It has been established via a combination of lattice and numeric calculations that the phase transition in the SM with a 125 GeV Higgs is not first order, but a mere cross-over. Indeed, the requirement of a first order phase transition is not enough, because sphaleron rates must be suppressed sufficiently to prevent wash-out. This can be translated into the criterion that the order parameter, v_c/T_c, must be greater than unity [58], which would require the Higgs to be lighter than 32 GeV [59]. Also, even though there is CP violation in the SM arising from a complex phase in the Cabbibo-Kobayashi-Maskawa (CKM) matrix, it is commonly agreed upon that this is not enough for successful EWBG [54]. Hence, there must be beyond the Standard Model (BSM) physics to explain the BAU.

In chapter 3 we will present a successful implementation of EWBG which adds new fermions to the SM. These will alter the finite temperature Higgs potential and allow for a strongly first order PT. At the same time they provide a valid dark matter candidate and can influence Higgs decays such that they could be observed at the LHC.

Baryogenesis at the electroweak scale is by no means the only possibility. Another popular mechanism is leptogenesis [60]. In this scenario one introduces right-handed, heavy neutrinos such that SM neutrinos obtain their light masses via the Seesaw mechanism [61–64]. Majorana mass terms of these new states introduce lepton number violating interactions by two units and the new Yukawa couplings can serve as sources for CP violation. Initially, a lepton number asymmetry is created by the out-of-equilibrium decay of the right-handed neutrinos that is then transferred to a baryon asymmetry via sphaleron processes. The viability of leptogenesis can e.g. be tested by observation of neutrinoless double beta decays [65] or lepton number violating processes at the LHC [66, 67]. If observed at low energies,

washout processes could potentially erase a baryon asymmetry that was generated at a higher scale.

In Grand Unified Theories (GUTs) baryogenesis may be realised via the decay of heavy bosonic states [68]. New gauge bosons related to the unifying symmetry mediate B and L violating interactions such that their out-of-equilibrium decay can in principle generate a baryon asymmetry. However, these type of models have problems to avoid washout through sphaleron processes, which are in general in equilibrium until electroweak symmetry breaking.

This ends our discussion of baryogenesis. We will address another problem facing the SM, the hierarchy problem, in the next section and introduce Supersymmetry as a possible solution.

1.3 Supersymmetry

We have seen, using as examples the problem of dark matter and the BAU, that the SM must be incomplete. This section will discuss an additional challenge for the SM that arises when the theory is embedded into another quantum field theory, the so-called hierarchy problem. As all fundamental scalars, the Higgs receives loop corrections that are proportional to the square of any cut-off scale, $\Lambda_{\rm UV}$, of loop-integrals and to the square of the mass of the heaviest particle that the Higgs couples to,

$$\Delta m_h^2 = \frac{\lambda_S}{16\pi^2}\left[\Lambda_{\rm UV}^2 - 2m_S^2 \log\left(\frac{\Lambda_{\rm UV}}{m_S}\right) + \dots\right], \tag{1.14}$$

where we chose the example of a new scalar field, S, with coupling λ_S to the Higgs. Even when a direct coupling between the Higgs and the new state is absent, two loop contributions would result in a similar expression, compare to [69]. Hence, it is hard to imagine a situation in which the Higgs receives no corrections at all once new physics is postulated. We are then left with the puzzle why its mass is relatively small, at only 125 GeV.

An elegant solution, at least in an idealistic application, is Supersymmetry (SUSY). Supersymmetry is a new symmetry that relates bosons and fermions. As a space-time symmetry it is a loophole to the Coleman-Mandula theorem [70], which quotes that the symmetries of any 4-dimensional quantum field theory can only be the direct product of internal symmetries and the Poincaré group. This theorem was extended into the Haag-Lopuszanski-Sohnius theorem [71] allowing also for the Supersymmetry algebra, and thus, Supersymmetry is the only known way to extend the Poincaré group.

In unbroken Supersymmetry each particle has a superpartner with the same mass. Therefore any loop contribution to the Higgs would get cancelled due to the relative signs of boson and fermion loops. As there has been no observation of any superpartner so far, we know that if SUSY exists it must be broken and the solution of the hierarchy problem is not perfect.

In the following section we will introduce the simplest, consistent supersymmetric version of the SM, the Minimal Supersymmetric Standard Model.

1.3.1 The Minimal Supersymmetric Standard Model

In this section we will discuss the particle content of the MSSM. Each fermion obtains a superpartner, called a *sfermion*. The scalar superpartners are *squarks* like the *stop*, and *sleptons* like the *smuon*. In shorthand notation, the superpartners obtain a tilde over their symbols. Because SM fermions have different quantum numbers depending on their handedness, it is common, and we will follow this notation here, to denote the scalar superpartners with a handedness as well. For example, the superpartner of the left-handed muon is denoted as $\widetilde{\mu}_L$.

For the Higgs boson it turns out that in order to guarantee anomaly cancellation and that the superpotential is holomorphic two doublets have to be introduced, such that the MSSM falls into the class of two Higgs doublet models. The fermionic

Names		spin 0	spin 1/2	$SU(3)_C$, $SU(2)_L$, $U(1)_Y$
squarks, quarks	Q	$(\widetilde{u}_L \;\; \widetilde{d}_L)$	$(u_L \;\; d_L)$	$(\mathbf{3}, \mathbf{2}, \frac{1}{6})$
(×3 families)	$\overline{u}$	$\widetilde{u}^*_R$	$u^\dagger_R$	$(\overline{\mathbf{3}}, \mathbf{1}, -\frac{2}{3})$
	$\overline{d}$	$\widetilde{d}^*_R$	$d^\dagger_R$	$(\overline{\mathbf{3}}, \mathbf{1}, \frac{1}{3})$
sleptons, leptons	L	$(\widetilde{\nu} \;\; \widetilde{e}_L)$	$(\nu \;\; e_L)$	$(\mathbf{1}, \mathbf{2}, -\frac{1}{2})$
(×3 families)	$\overline{e}$	$\widetilde{e}^*_R$	$e^\dagger_R$	$(\mathbf{1}, \mathbf{1}, 1)$
Higgs, higgsinos	H_u	$(H^+_u \;\; H^0_u)$	$(\widetilde{H}^+_u \;\; \widetilde{H}^0_u)$	$(\mathbf{1}, \mathbf{2}, +\frac{1}{2})$
	H_d	$(H^0_d \;\; H^-_d)$	$(\widetilde{H}^0_d \;\; \widetilde{H}^-_d)$	$(\mathbf{1}, \mathbf{2}, -\frac{1}{2})$

TABLE 1.1: Chiral supermultiplets in the Minimal Supersymmetric Standard Model as presented in [69].

superpartners are called *higgsinos*. We summarise these *chiral supermultiplets* in table 1.1.

The superpartners of SM gauge bosons are called *gauginos*. For the gluon we have the *gluinos*, for the W^+, W^- and W^0 of the SU(2) symmetry there are the *winos* and the superpartner of the U(1) gauge boson B^0 is the *bino*. We summarise their quantum numbers in table 1.2.

Since we have two Higgs doublets with overall eight degrees of freedom (dof) of which three get eaten by the gauge bosons five Higgs scalars remain after electroweak symmetry is broken. Two of them are neutral and CP even, one is neutral and CP odd and the other two carry electromagnetic charge. One of the two neutral, CP even states must be the Higgs boson of the SM with a mass of 125 GeV.

The neutral higgsinos will mix with the neutral gauginos to form *neutralinos* and the charged higgsinos will mix with the charged gauginos to form *charginos*. We will denote their lightest states with $\tilde{\chi}^0_1$ and $\tilde{\chi}^\pm_1$, respectively. The neutralino mixing matrix is [69],

Names	spin 1/2	spin 1	$SU(3)_C$, $SU(2)_L$, $U(1)_Y$
gluino, gluon	$\widetilde{g}$	g	(**8**, **1** , 0)
winos, W bosons	$\widetilde{W}^{\pm}$ $\widetilde{W}^{0}$	$W^{\pm}$ W^{0}	(**1**, **3** , 0)
bino, B boson	$\widetilde{B}^{0}$	B^{0}	(**1**, **1** , 0)

TABLE 1.2: Gauge supermultiplets in the Minimal Supersymmetric Standard Model as presented in [69].

$$\mathbf{M}_{\tilde{\chi}_1^0} = \begin{pmatrix} M_1 & 0 & -c_\beta\, s_W\, m_Z & s_\beta\, s_W\, m_Z \\ 0 & M_2 & c_\beta\, c_W\, m_Z & -s_\beta\, c_W\, m_Z \\ -c_\beta\, s_W\, m_Z & c_\beta\, c_W\, m_Z & 0 & -\mu \\ s_\beta\, s_W\, m_Z & -s_\beta\, c_W\, m_Z & -\mu & 0 \end{pmatrix}, \tag{1.15}$$

where M_1 is the bino mass parameter, M_2 the wino mass parameter, μ the higgsino mass parameter, m_Z the Z boson mass, and s_W and c_W are the sine and cosine of the weak mixing angle, respectively. We define $\tan\beta$ as the ratio of the up- and down-type Higgs vacuum expectation values, $\tan\beta = v_u/v_d$, and have accordingly $s_\beta = \sin\beta$ and $c_\beta = \cos\beta$. To obtain the mass eigenvalues, the matrix can be diagonalised by a unitary matrix, $\mathbf{N}$, such that we have as the lightest neutralino,

$$\tilde{\chi}_1^0 = N_{11}\widetilde{B}^0 + N_{12}\widetilde{W}^0 + N_{13}\widetilde{H}_u^0 + N_{14}\widetilde{H}_d^0\,, \tag{1.16}$$

where N_{ij} are elements of the neutralino mixing matrix. We call $\tilde{\chi}_1^0$ "bino-like" if N_{11} is much greater than any other element (this is true if $M_1 \ll M_2, \mu$). This rule generalises to terms like "wino-like" or "higgsino-like" for all four neutralinos and both charginos.

Similarly, in the stop sector we have a mass matrix that mixes the left and right handed stops. In the basis,

$$\Phi = (\widetilde{t}_L, \widetilde{t}_R)\ , \tag{1.17}$$

and,

$$\mathcal{L} \supset \Phi^* \ \mathbf{m}_{\tilde{\mathbf{t}}}^{\mathbf{2}} \ \Phi^T \ , \tag{1.18}$$

we have [69],

$$\mathbf{m}_{\tilde{\mathbf{t}}}^{\mathbf{2}} = \begin{pmatrix} m_{Q_3}^2 + m_t^2 + \Delta_{\tilde{u}_L} & v(a_t^* \sin\beta - \mu y_t \cos\beta) \\ v(a_t \sin\beta - \mu^* y_t \cos\beta) & m_{\overline{u}_3}^2 + m_t^2 + \Delta_{\tilde{u}_R} \end{pmatrix} \ , \tag{1.19}$$

In this matrix, $m_{Q_3}^2$ is the explicit soft-SUSY breaking mass term for the scalar superpartner of the left-handed top quark and $m_{\overline{u}_3}^2$ is the corresponding term for the superpartner of the right-handed top quark. The terms proportional to m_t^2 originate from quartic scalar interactions of two stops and two Higgs particles that are proportional to the Yukawa couplings. The terms $\Delta_{\tilde{u}_L,\tilde{u}_R}$ arise from requiring that the gauge sector is invariant under supersymmetric transformations and are fixed by the gauge couplings, $\Delta_{\tilde{q}} = (T_{3,\tilde{q}}\ g^2 - Y_{\tilde{q}}\ g'^2)(v_d^2 - v_u^2)$. Here, $\tilde{q}$ denotes the squark, T_3 and Y are the third component of the weak isospin and weak hypercharge, respectively, and g and g' are the SU(2) and U(1) gauge coupling strengths. The off-diagonal elements come from triple scalar couplings proportional to the Yukawa coupling and the Higgsino mass parameter or, alternatively, to the supersymmetry breaking, tri-linear couplings, a_t.

In the sbottom sector a very similar matrix exists:

$$\mathbf{m}_{\tilde{\mathbf{b}}}^{\mathbf{2}} = \begin{pmatrix} m_{Q_3}^2 + \Delta_{\tilde{d}_L} & v(a_b^* \cos\beta - \mu y_b \sin\beta) \\ v(a_b \cos\beta - \mu^* y_b \sin\beta) & m_{\overline{d}_3}^2 + \Delta_{\tilde{d}_R} \ . \end{pmatrix} \tag{1.20}$$

Here, we have $m_{\overline{d}_3}^2$ as the soft-SUSY breaking mass term for scalar superpartner of the right-handed bottom quark and the bottom Yukawa coupling, y_b, appears alongside the tri-linear couplings a_b in the off-diagonal elements.

The lightest stop (sbottom) may be purely left handed if $m_{Q_3}^2$ is much smaller than $m_{\overline{u}_3}^2$ ($m_{\overline{d}_3}^2$). Mixing plays a role if the off-diagonal terms are not negligible and will

reduce the mass of the lightest stop (sbottom). Choices of these parameters will play an important role in Chapter 2, where we will discuss how they influence the decay chains.

To avoid proton decay, the MSSM is equipped with an additional symmetry called R-parity, effectively a $\mathbb{Z}_2$ symmetry under which SM particles and SUSY particles transform with opposite sign. This has immediate consequences. At a particle accelerator SUSY particles can only be produced in pairs and the lightest SUSY particle (LSP) is stable and, therefore, forms an ideal dark matter candidate. Because the DM particle has to be neutral there are two options in the MSSM, either the lightest neutralino or the lightest sneutrino. From these two options the sneutrino is ruled out by direct detection searches due to its rather strong coupling with the Z-boson. Neutralino dark matter is a vast area of research and realisations consistent with the relic abundance, direct dark matter searches, indirect and collider searches exist on a wide range of masses.

The quest to find SUSY has so far been unsuccessful and the elegance of the original solution to the hierarchy problem is under question. However, because of the numerous parameters in the MSSM it is too early to discard the theory already. It is especially important to note that published limits on the superpartner masses are highly model dependent and should be recast for each realisation separately. We will present one such approach in chapter 2 in the context of interpreting an observed dilepton excess in CMS in terms of the MSSM.

1.4 Thesis outline

In this chapter we have given an overview over three problems that the SM is currently facing. These were the question of what dark matter is, how the baryon asymmetry is generated dynamically and why the Higgs mass is so light. For each of these problems we described ideas that can solve them. These included the weakly interacting massive particle as a dark matter candidate that freezes out

in the early Universe, electroweak baryogenesis that strengthens the electroweak phase transition such that sphaleron processes are switched off inside the bubbles to prevent washout and Supersymmetry that may cancel loop corrections to masses of fundamental scalars. This thesis will incorporate these ideas and relations among them in the following way:

In Chapter 2 we will suggest SUSY models to fit an observed dilepton excess as observed by the CMS experiment. We will take this excess as an example to show how limits from complementary collider searches can be recast onto a specific SUSY model such that a solid statement about its validity can be made. In this way we will test whether it is possible to explain this excess in terms of SUSY and whether valid spectra are consistent with dark matter searches. This chapter is based on [72].

Chapter 3, based on [73], will focus on relations between dark matter and baryogenesis. We will prove that both phenomena can be explained simultaneously by adding vector-like fermions to the SM and will confront the model with constraints arising from dark matter experiments, electroweak precision tests and collider searches. We will also address an enhancement of the Higgs decay rate to two photons that was observed by ATLAS and CMS.

In Chapter 4 we will propose the use of directional information to overcome the neutrino bound that will limit future direct dark matter searches. We will show how coherent neutrino-nucleus elastic scattering leads to this bound, compare the scaling behaviour of directional and non-directional searches and calculate necessary exposures to surpass this limit. This chapter is based on [74].

We conclude in chapter 5.

Chapter 2

Deviations in SUSY searches

One major goal of the Large Hadron Collider is to search for Supersymmetry which is one of the most popular frameworks of physics beyond the Standard Model. If SUSY is realised in nature, the minimal supersymmetric Standard Model forms the most basic application of this framework to the SM. Many dedicated searches for the MSSM are being carried out, but no definite evidence has been found up to date putting pressure on low-energy SUSY. However, it is too early to write the MSSM off quite yet, as we discuss in this chapter.

The constraints published by the LHC experiments are highly model dependent as production cross-sections and branching ratios depend strongly on the MSSM parameters. For example, in the left panel of figure 2.1 we show limits on electroweak chargino-neutralino pair production. Depending on the decay mode of the electroweakinos the limits can be more or less stringent. For wino-like light electroweakinos that decay via left-handed sleptons current limits can reach up to 700 GeV for charginos and 400 GeV for the lightest neutralino [75]. If they decay via W or Z bosons, the limits are weakened to approximately 400 GeV for charginos and only 160 GeV for the LSP [76]. The situation is similar for stop production that is shown in the right panel of the same figure.

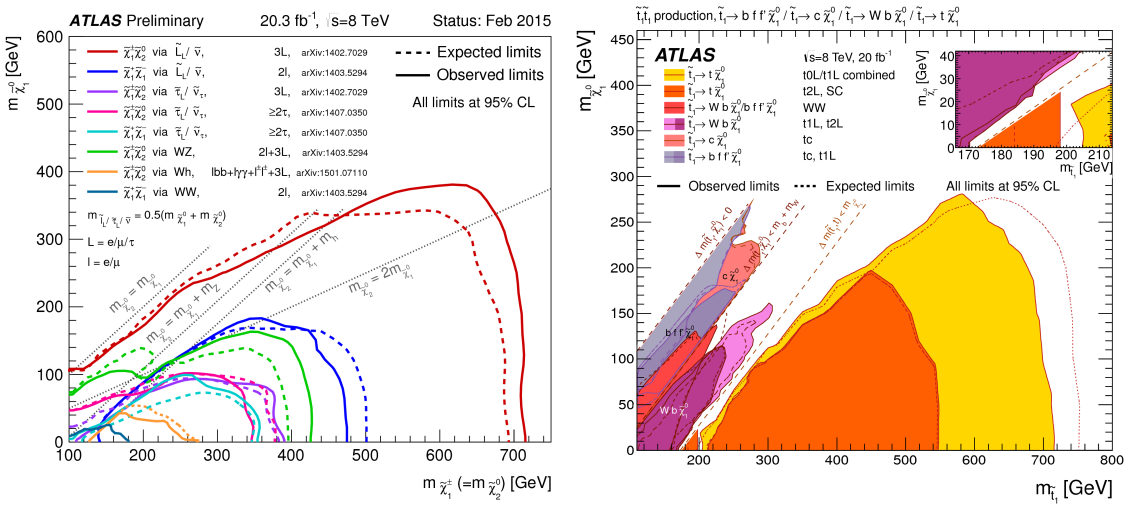

FIGURE 2.1: Exclusion limits on electroweak chargino-neutralino and direct stop pair production in the left and right panel, respectively. These summary plots were taken from the ATLAS collaboration [77].

Applying published limits to the MSSM is therefore not straight forward. Ideally, each search should be reinterpreted for each given realisation of the MSSM to get a trustworthy statement about its validity. This is a complex undertaking and not possible in every study, however, we will present one such approach in this chapter.

Despite the lack of convincing evidence there are slight excesses that, while statistically non-significant, could form the first hint of SUSY or the MSSM. It is interesting to investigate these excesses to see what can be learned from them about the MSSM spectrum and which other channels could form complementary tests. In this chapter we will investigate an excess found by the CMS (Compact Muon Solenoid) collaboration in a final state consisting of two leptons, jets and missing energy. An excess in the invariant mass distribution of the opposite-sign same-flavour (OSSF) lepton pair has been observed at a significance of 2.6σ [78, 79].

It should be mentioned that it is statistically expected that some LHC studies deviate from the expected results simply by the mere number of performed searches. However, slight deviations always trigger detailed phenomenological studies and serve as a source of creativity. Ultimately, each possible signal will start as a non-significant excess, such that detailed investigations are interesting and important.

We will start with defining relevant quantities used in LHC searches and presenting the CMS and ATLAS (A Toroidal LHC Apparatus) detectors. Then, we outline SUSY production at the LHC.

2.1 Introduction

The ATLAS and CMS detectors are general purpose detectors that are designed to detect a wide range of new particles. The identification of particles in such a particle detector occurs in many layers. Around the interaction point vertex detectors try to find secondary vertices, i.e. the decays of particles that were produced at the initial proton-proton interaction. Tracking systems around this layer record the track of charged particles and, together with the magnetic field B, the ratio of charge, Q, to momentum, p can be measured by the curvature, r, of the track via $r \propto QB/p$. To identify the particle the energy loss, dE/dx is helpful which possesses a proportionality as $dE/dx \propto (Q/\beta)^2$, where $\beta = v/c$. The combined measurement of β from the energy loss and of p from the curvature can then be used to determine the mass of a particle with unit charge.

The following two layers, the electromagnetic and hadronic calorimeters measure the total energy of particles. In an ideal situation the particle will be stopped completely in the corresponding calorimeter such that its total energy is measured. In the electromagnetic calorimeter electrons and photons are stopped that lose their energy mainly via Bremsstrahlung and pair production, respectively. Hadrons are measured in the hadronic calorimeter where they mainly ionise the material. Particles that have only small energy losses in the detector and pass through all these layers, like muons, can leave traces in the outer "muon chambers".

In this section we will define basic quantities used in LHC analysis and present both the ATLAS and CMS detectors.

2.1.1 Collider basics

In both detectors the origin of the coordinate system is the interaction point. The x-coordinate points towards the centre of the LHC, the y-axis is directed upwards and the z-axis follows the direction of the anti-clockwise running (proton) beam such that a right-handed coordinate system is defined.

The polar angle θ is defined as the angle measured from the positive z-axis in the z-y-plane. The pseudorapidity is then given by $\eta = -\log(\tan(\theta/2))$. The azimuthal angle ϕ is measured around the beam axis in the x-y-plane. Then, a distance in the angle space may be defined as $\Delta R = \sqrt{(\Delta\eta)^2 + (\Delta\phi)^2}$. Transverse quantities, like transverse momentum p_T or energy E_T and missing transverse energy $\not{E}_T$, relate to the x-y-plane.

The invariant mass is defined as the squared sum of the momentum four vectors of the final state particles,

$$m_{\text{inv}}^2 = \left(\sum_{i=1}^{n} p_i\right)^2 , \tag{2.1}$$

and is generally used when looking for a s-channel resonance.

The invariant mass of a new resonance cannot be reconstructed if some final state particles are invisible, e.g. in the semi-invisibly decay of the W boson, $W \to \bar{\nu_e} e$. In such a case missing transverse momentum can be defined as,

$$\vec{\not{p}}_T = -\sum_i \vec{p}_{T,i,\text{obs}} \, . \tag{2.2}$$

A better way to find the mass of such a resonance is the transverse mass [80],

$$m_T^2(\vec{p}_1, \vec{p}_2) = (E_{1,T} + E_{2,T})^2 - (\vec{p}_{1,T} + \vec{p}_{2,T})^2 \, , \tag{2.3}$$

In the case of the leptonically decaying W boson $\vec{p}_1$ and $\vec{p}_2$ are the lepton and missing momentum vector, respectively. Then, the distribution of m_T^2 is cut off sharply at the mass of the W which can be used to infer its mass.

In this chapter, another mass variable will play a role, the so-called *stransverse mass*, m_{T2} [81, 82]. It is a generalisation of the transverse mass when a pair of semi-invisibly decaying particles is produced and defined as,

$$m_{T2}(\vec{p}_{T,1}, \vec{p}_{T,2}, \vec{q}_T) = \min_{\vec{q}_{1,T}+\vec{q}_{2,T}=\vec{q}_T} \max[m_T(\vec{p}_1, \vec{q}_1), m_T(\vec{p}_2, \vec{q}_2)]\,. \tag{2.4}$$

In the case of a leptonically decaying W boson pair, $\vec{q}_T$ would be the missing momentum vector and $\vec{p}_{1,T}$ and $\vec{p}_{2,T}$ the momenta of the final state leptons. In this case the distribution of m_{T2} is again bounded by the mass of the decaying particle.

After defining relevant quantities, we will present the ATLAS and CMS detectors in the next section.

2.1.2 The ATLAS detector

The ATLAS detector [83] is the largest detector at the LHC. Its dimensions, that measure 44m in length and 25m in height, are determined by the large muon chambers. The muon chambers consist of 3 layers of tracking chambers with two end-cap and one long barrel toroidal magnetic systems generating a strong magnetic field of around 4T for track bending. The muon spectrometer has a coverage of $|\eta| \leq 2.7$.

The inner part of the detector contains pixel detectors as well as transition radiation and semiconductor trackers that are surrounded by a superconducting solenoid magnet with a field strength of 2.6T. Tracking of charged particles occurs in these inner regions for $|\eta| < 2.5$. The electromagnetic calorimeter uses liquid argon (LAr) technology and covers a pseudorapidity range of $|\eta| \leq 3.2$. Hadronic calorimetry is performed in a scintillator-tile calorimeter with a range $|\eta| \leq 1.7$. Additionally there are end-cap LAr calorimeters that extend the range of electromagnetic and hadronic energy measurements. A sketch of the ATLAS detector is shown in figure 2.2.

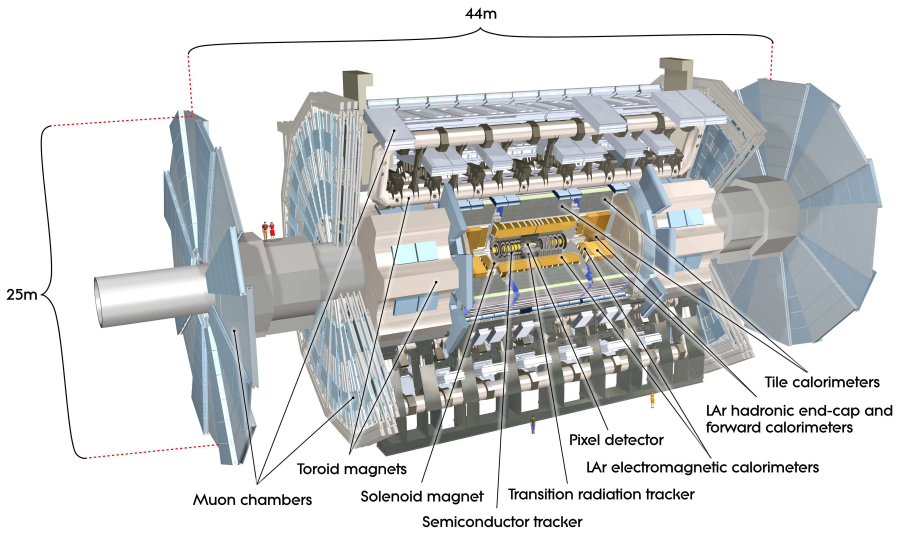

FIGURE 2.2: Schematic view of the ATLAS detector as shown in [83]

2.1.3 The CMS detector

The central superconducting magnet in the CMS experiment [84] is a 13m long solenoid establishing a 4T field. In its interior there are pixel detectors and silicon trackers that allow for charged particle tracking in a range $|\eta| \leq 2.5$. The electromagnetic and hadronic calorimeter are placed inside this solenoid. In the electromagnetic calorimeter lead tungstate ($PbWO_4$) crystals are used whose scintillation light is detected by avalanche photodiodes. The covered range is $|\eta| \leq 3.0$. There are pre-shower silicon detectors with lead absorbers.

The surrounding hadronic calorimeter (including end-cap) is made out of alternating layers of brass and plastic scintillators covering a range $|\eta| \leq 3.0$. The scintillation light passes through wavelength shifters to photo diodes for read-out. An additional very-forward calorimeter is attached to extend coverage to $|\eta| \leq 5.0$. Its layers are alternating iron and quartz-fibre. The latter ones emit Cherenkov radiation that is detected in photomultipliers.

The muon detectors, placed around the solenoid, are a collection of drift tubes, cathode strip chambers and plate chambers that altogether cover a range $|\eta| \leq 2.4$. They are embedded with a steel yoke that guides the outer magnetic field lines of the solenoid. We show a sketch of the CMS detector in figure 2.3.

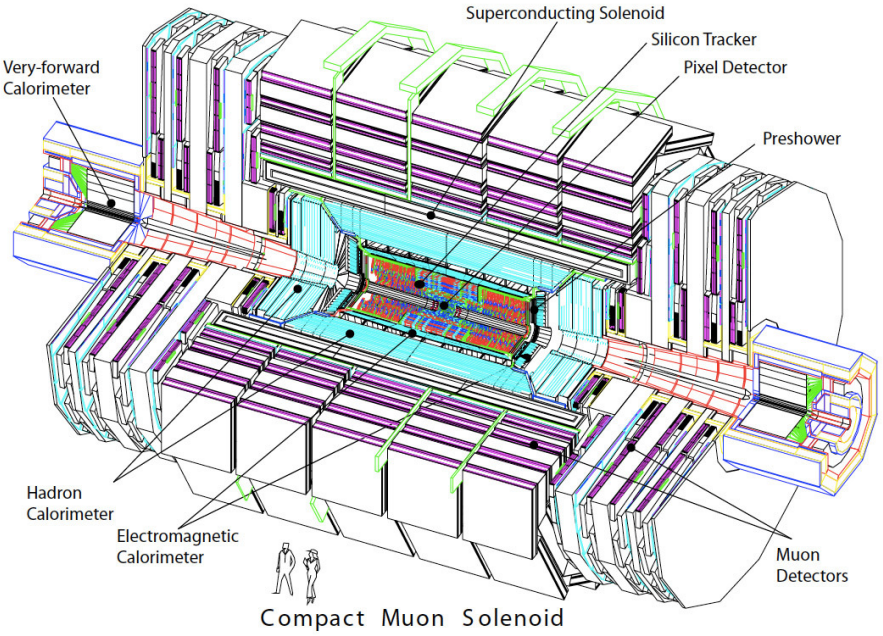

FIGURE 2.3: Schematic view of the CMS detector as shown in [84].

Having presented both general purpose detectors, we will give an introduction of SUSY production at the LHC in the next section.

2.1.4 SUSY production at the LHC

In this section we discuss the production of SUSY particles at the LHC. The analysis in this chapter will be mainly focused on squark/squark or squark/anti-squark production such that we focus on these production channels here.

Squark/anti-squark pairs can be produced via gluon fusion processes either through an s-channel gluon or a t-channel squark exchange, or through a four point interaction between two gluons and a squark anti-squark pair. Another possibility is quark/anti-quark annihilation via a s-channel gluon or t-channel gluino exchange. Squark/squark production proceeds via t-channel gluino exchange of an incoming quark/quark pair.

Production of light squarks has to be treated separately from stop or sbottom production. With light squarks we refer to the superpartners of the four lightest

quarks. These superpartners are not necessarily lighter than sbottoms or stops. Left-right mixing, that is proportional to the Yukawa coupling, can be neglected in the light squark sector, whereas significant mixing can occur in the heavy squark sector. Furthermore, it is usually assumed that the six soft SUSY breaking mass parameters of the light squarks are degenerate. Hence, the production cross section of the light squarks can usually be combined. In the heavy squark sector, on the other hand, large Yukawa couplings may introduce large mixing effects (especially for the stop sector) and lead to substantial mass gaps between both mass eigenstates.

Another difference between light and heavy squark flavours comes from the parton distribution function (pdf), which describes how much of the proton's momentum is carried by a given parton depending on the energy scale of the scattering process. Even though the LHC is mainly colliding gluons at these high energies, the final SUSY production cross section will be a combination of all possible processes. Since there are no top or bottom valence quarks in the proton, all t-channel production processes with quark/(anti)quark pairs as initial state are suppressed for third generation squarks.

We show in figure 2.4 the total cross section for pair production of strongly interacting SUSY particles in picobarns. It is visible that stop-quark production is smaller because of the pdf suppression. Since the LHC is a hadron collider, the production of electroweak particles like charginos or neutralinos, is usually much smaller and we will neglect it in our analyses. Note that this ultimately depends on the masses of the charginos/neutralinos and should be considered separately in each spectrum. We will point to electroweak production when it may be of importance throughout this chapter.

The calculation of SUSY production cross sections contains uncertainties due to the finite number of loops that are calculated and the resulting dependence on the chosen factorisation scale, μ_F, and renormalisation scale, μ_R. Renormalisation is a prescription to ensure finiteness of observable quantities in a quantum field theory.

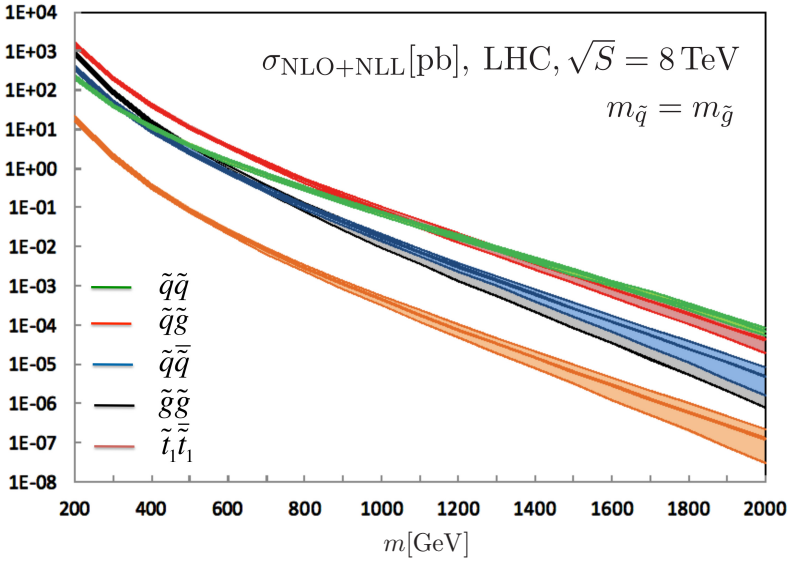

FIGURE 2.4: Production cross section of strongly interacting SUSY particles at the LHC at $\sqrt{s} = 8$ TeV as presented by the LHC SUSY Cross Section Working Group [85].

The energy point at which this prescription is applied has to be chosen by hand and introduces a renormalisation scale dependence. Factorisation is a method in QCD calculations that separates short distance physics (i.e. parton interactions) from long distance phenomena (i.e. hadronisation). A complete cross section calculation has to include both processes and thus introduces the matching scale μ_F. The dependence of the parton distribution functions on this energy scale is described by the DGLAP (Dokshitzer–Gribov–Lipatov–Altarelli–Parisi) equations [86–88]. As only a finite number of loops is calculated these scale dependences remain and theoretical uncertainties on cross sections are introduced. One expects this scale dependence to become smaller when higher loops are evaluated. The uncertainties from scale variations are typically of the order 10% [89].

Next to these theoretical difficulties, there are experimental errors on the pdf measurements, such as deep inelastic scattering. Uncertainties in the pdfs can range from around 5% for squark production to 15-30% for gluino production [89].

In this chapter, we will focus on the production of third generation squarks, stops

and sbottoms, with decoupled light squarks and gluinos. For the cross section we use calculations of the LHC SUSY Cross Section Working Group [85] that are based on NLL-fast [90–92].

Having presented the ATLAS and CMS detectors and outlined SUSY production at the LHC, in the next section we will present a CMS analysis that observed an excess in the dilepton plus jets and missing energy topology. We will also suggest MSSM models that could explain such an excess.

2.2 The dilepton edge

In the last section we have defined relevant quantities of LHC analyses and described the ATLAS and CMS detectors. We have also explained SUSY production cross sections and their uncertainties. In the following chapter we will present a CMS analysis that measured an excess in the dilepton invariant mass distribution and propose simplified MSSM models that can give such a signal.

2.2.1 CMS dilepton analysis

CMS has reported an excess of events in the dilepton plus missing energy channel [78, 79] in the 8 TeV, 19.4 fb^{-1} data. The analysis requires an opposite-sign same-flavour (OSSF) lepton pair with $p_T > 20$ GeV. It also requires two or more jets with $p_T > 40$ GeV and $\not{E}_T > 150$ GeV or three or more jets with $p_T > 40$ GeV and $\not{E}_T > 100$ GeV. The excess is observed in the central region where both leptons satisfy $|\eta_{\text{lep}}| < 1.4$. It exhibits an edge in the dilepton invariant mass distribution around $m_{\ell\ell} = 78$ GeV. The counting experiment in the $m_{\ell\ell} \in [20, 70]$ GeV region shows an excess of ~ 130 events over the Standard Model expectation, which corresponds to a standard deviation of 2.6σ.

The excess of the signal is fitted kinematically as a triangular-shape edge at $m_{\ell\ell} = 78.7 \pm 1.4$ GeV. Such a kinematic edge is a characteristic signal of SUSY, where a

SUSY particle undergoes a two-stage two-body decay. The kinematic edge formed by a pair of leptons can be interpreted as the cascade decay of a neutralino: $\tilde{\chi}_2^0 \to \tilde{\ell}^{\pm}\ell^{\mp} \to \ell^{\pm}\ell^{\mp}\tilde{\chi}_1^0$ (on-shell slepton decay) [93]. The edge would appear at [94–97]

$$m_{\text{edge}} = m_{\tilde{\chi}_2^0}\sqrt{\left(1-\frac{m_{\tilde{\ell}}^2}{m_{\tilde{\chi}_2^0}^2}\right)\left(1-\frac{m_{\tilde{\chi}_1^0}^2}{m_{\tilde{\ell}}^2}\right)}: \quad \tilde{\chi}_2^0 \to \tilde{\ell}^{\pm}\ell^{\mp} \to \ell^{\pm}\ell^{\mp}\tilde{\chi}_1^0\,. \tag{2.5}$$

It is also possible to interpret the edge as a three-body decay signal of a neutralino, $\tilde{\chi}_2^0 \to \ell^{\pm}\ell^{\mp}\tilde{\chi}_1^0$, where the lepton pair is produced via an off-shell Z (off-shell Z decay). The shape of the edge would be more rounded compared to the two-stage two-body decay, but as shown in the original CMS analysis, the three-body decay still provides a good fit. It appears simply at

$$m_{\text{edge}} = m_{\tilde{\chi}_2^0} - m_{\tilde{\chi}_1^0}: \quad \tilde{\chi}_2^0 \to \ell^{\pm}\ell^{\mp}\tilde{\chi}_1^0\,. \tag{2.6}$$

In order to have two or more high p_T jets as required in the event selection, and to boost the direct production of $\tilde{\chi}_2^0$ we consider production of coloured SUSY particles, which subsequently decay into $\tilde{\chi}_2^0$. The final CMS analysis [79] reported that most of the excessive events are associated with at least one b-jet. This information rules out light squark scenarios and disfavours pure electroweak production. Thus, we will concentrate on an explanation in terms of bottom squark production.

The ATLAS experiment also released an analysis of the jets plus OSSF dilepton channel [98]. They explicitly looked at the signal region employed in the CMS dilepton analysis but did not find any significant excess. This casts a doubt that the observed dilepton excess is merely due to the statistical fluctuation or background mismodeling. The next run of the LHC will provide a definitive answer to this question. It should be noted, that the ATLAS team did not constrain the leptons to be central which may be important for a signal.

We take a bottom-up approach by considering simplified SUSY models with minimal particle content at low energy to reproduce the excess optimally. Some SUSY

models have already been studied in earlier works [93, 99], but a detailed collider study is still missing.[1] We will fill this gap here. In the next section we present the considered sbottom models.

2.2.2 Sbottom scenarios

One way to interpret the CMS dilepton excess that we presented in the previous section is to assume that the observed dileptons in the excessive events come from cascade decays of bottom squarks. The decay mode to charginos, $\tilde{b}_1 \to t\tilde{\chi}_1^\pm$, is kinematically forbidden if $m_{\tilde{b}_1} < m_t + m_{\tilde{\chi}_1^\pm}$, which we consider here because the emergence of top quarks would increase constraints. We will look at two possible scenarios, the *on-shell slepton* and the *off-shell Z* models that differ in the $\tilde{\chi}_2^0$ decay mode.

In the on-shell slepton scenario the $\tilde{\chi}_2^0$ may decay either via a right-handed charged slepton or a left-handed charged slepton and sneutrino. We will treat these two cases separately in our analysis.

If the mediating slepton is right-handed, $\tilde{\chi}_2^0$ predominantly decays into two charged leptons and $\tilde{\chi}_1^0$ via its higgsino component, and the events tend to have more than two leptons in the final state. Such models are severely constrained by the multi-lepton plus missing energy searches. To avoid these constraints, we assume 70 % of sbottoms decay into a bottom quark and a $\tilde{\chi}_1^0$ and the rest of sbottoms decay into a bottom quark and a $\tilde{\chi}_2^0$. This situation can be achieved if $\tilde{\chi}_2^0$ is wino-like and $\tilde{b}_1$ has a large component of $\tilde{b}_R$. We have the following decay chains in the sbottom with on-shell slepton model.

$$\begin{aligned} \tilde{b}_1 \to b\tilde{\chi}_2^0 \to b\ell^\pm\tilde{\ell}^\mp \to b\ell^\pm\ell^\mp\tilde{\chi}_1^0 \quad &: \quad 30\,\%, \\ \tilde{b}_1 \to b\tilde{\chi}_1^0 \quad &: \quad 70\,\%. \end{aligned}$$

[1] See [100] for a non-SUSY interpretation of the observed excess.

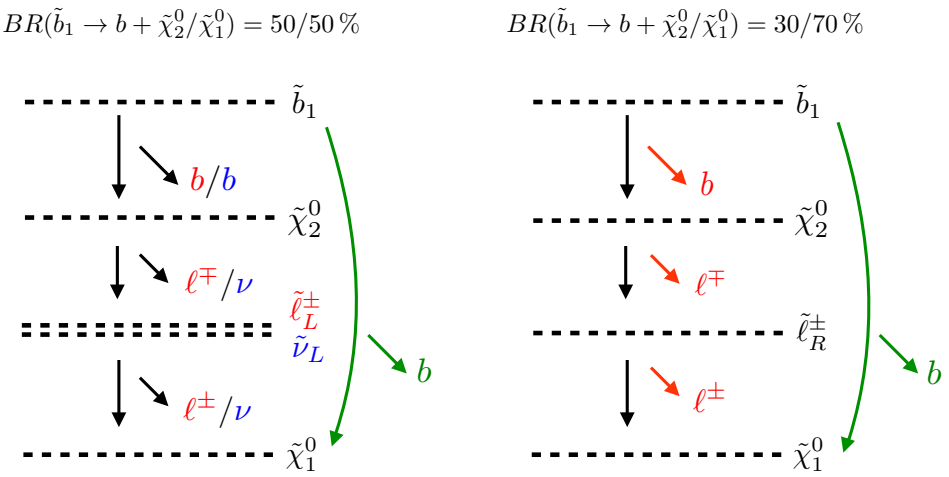

FIGURE 2.5: Decay chains of on-shell slepton mediated sbottom scenarios (*left*: left-handed slepton model, *right*: right-handed slepton model).

In the case where the mediating slepton is left-handed, sneutrinos are introduced as SU(2) partners of charged sleptons. We assume that sneutrinos and charged sleptons are mass degenerate and $\tilde{\chi}_2^0$ decays democratically into charged sleptons and sneutrinos.

$$\begin{aligned} \tilde{b}_1 \to b\tilde{\chi}_2^0 \to b\ell^\pm\tilde{\ell}^\mp \to b\ell^\pm\ell^\mp\tilde{\chi}_1^0 \quad &: \quad 25\,\%, \\ \tilde{b}_1 \to b\tilde{\chi}_2^0 \to b\nu\tilde{\nu} \to b\nu\nu\tilde{\chi}_1^0 \quad &: \quad 25\,\%, \\ \tilde{b}_1 \to b\tilde{\chi}_1^0 \quad &: \quad 50\,\%. \end{aligned}$$

The schematic picture of these cases is shown in Fig. 2.5.

We will now discuss the off-shell Z model for the sbottom scenario, in which the $\tilde{\chi}_2^0$ undergoes a 3-body decay via an off-shell Z. Because of the small branching ratio of the Z into leptons (about 7% into electron and muon pairs), we need sbottoms to have a sizeable decay branching ratio to $\tilde{\chi}_2^0$. Otherwise the dilepton event rate would be too small. One way to realise this situation is to have a higgsino-like $\tilde{\chi}_2^0$, a mostly right-handed $\tilde{b}_1$ and to assume a large sbottom-bottom-higgsino coupling due to a large tanβ. It is shown in [99] that for tan$\beta = 50$, $m_{\tilde{b}_1} \simeq 330$ GeV and a higgsino mass parameter $\mu \simeq 290$ GeV around 44% of sbottoms decay to the roughly mass-degenerate $\tilde{\chi}_2^0$ and $\tilde{\chi}_3^0$. This model point predicts about 1σ less events than the

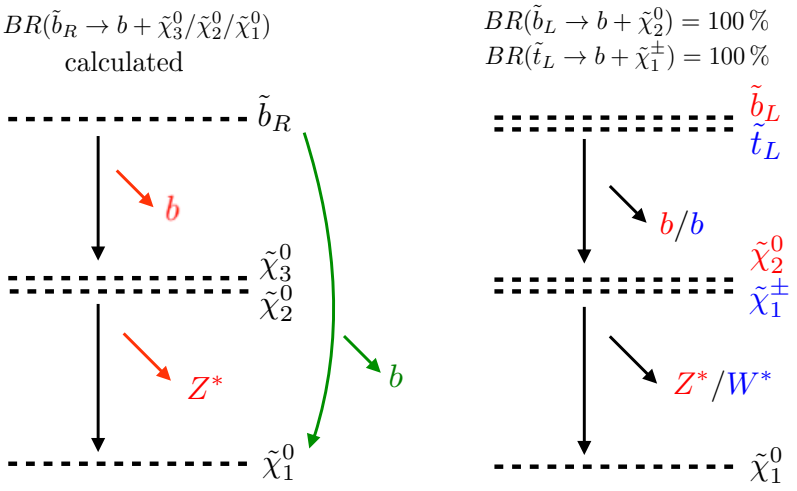

FIGURE 2.6: Decay chains of off-shell Z mediated sbottom scenarios (*left*: right-handed sbottom model, *right*: left-handed sbottom model).

central fit without being excluded. In order to explore the parameter region that could possibly contribute to the excess in more detail, we expand the study of this scenario by varying the parameters M_1, μ and $m_{\tilde{b}_1}$, while fixing $\tan\beta = 50$. The mass spectrum and particle decay branching ratios of this simplified model are calculated using `SPheno` [101, 102].

Alternatively one can obtain a large branching ratio of sbottom decaying to $\tilde{\chi}_2^0$ by assuming that $\tilde{b}_1$ is left-handed and $\tilde{\chi}_2^0$ is wino-like. Due to $SU(2)$ gauge invariance a left-handed top squark, $\tilde{t}_1$, is necessarily included in the low energy spectrum. For simplicity, we assume $m_{\tilde{b}_1} = m_{\tilde{t}_1}$. We consider the following decay chains for the left-handed sbottom with off-shell Z model.

$$\begin{aligned} \tilde{b}_1 \to b\tilde{\chi}_2^0 \to bf\bar{f}\tilde{\chi}_1^0 \text{ (via } Z^*) \quad &: \quad 100\,\%, \\ \tilde{t}_1 \to b\tilde{\chi}_1^\pm \to bf\bar{f}'\tilde{\chi}_1^0 \text{ (via } W^*) \quad &: \quad 100\,\%. \end{aligned}$$

A schematic picture of the off-shell Z sbottom scenarios is shown in Fig. 2.6.

The sbottom scenarios are the priorities of this work, but let us also touch on the possibilities of explaining the dilepton excess with the remaining coloured sparticles in SUSY, namely gluino and stop. Gluinos can decay into $\tilde{\chi}_2^0$ via an intermediate squark and will thus not be very much different from the sbottom scenario other

than a larger jet multiplicity. Stops decay into a top quark and would lead to an extra lepton that plays no role in explaining the dilepton excess. It is not clear how gluinos or stops could explain the dilepton excess without inducing additional jet or leptonic constraints, and hence we are not going to study these scenarios further in this analysis.

We will confront the suggested sbottom scenarios with a comprehensive list of other LHC constraints originating from ATLAS and CMS direct SUSY searches. In order to accurately estimate the LHC constraints and simulate many analyses systematically, we use the automated simulation tool `Atom` [103]. In the following section we describe that simulation in greater detail.

2.3 The simulation setup

After presenting the CMS analysis and suggesting sbottom scenarios that can explain the excess, in this section we will describe our procedure to calculate the contribution to the CMS dilepton excess and the constraints from other ATLAS and CMS SUSY searches.

For the stop and sbottom production cross sections, σ_{prod}, we use results from the LHC SUSY Cross Section Working Group based on [85]. We create SUSY Les Houches Accord (SLHA) files of our simplified models for the event generation and pass them to `Pythia 6.4` [104] to generate $10 \cdot \sigma_{\text{prod}} \cdot \mathcal{L}$ events with a maximum of $5 \cdot 10^5$, where $\mathcal{L} = 19.4$ fb^{-1} is the integrated luminosity at the CMS dilepton analysis. We then run `Atom` [103] on the generated event files in HepMC format to estimate the efficiencies, ϵ, of the signal regions defined in all the ATLAS and CMS analyses that will be used in this work. Application examples and validation of `Atom` can be found in [105–107]. We have implemented the CMS dilepton analysis in `Atom` and validated it using the cut-flow tables given by the CMS collaboration based on the $\tilde{b}_1 \to b\tilde{\chi}_2^0 \to b\ell^+\ell^-\tilde{\chi}_1^0$ simplified model. The comparison in the number

channel	search for	arXiv or CONF-ID	refs
$2{-}6j + 0\ell + \not{E}_T$	$\tilde{q}, \tilde{g}$	ATLAS-CONF-2013-047	[109]
		1405.7875	[110]
$2b + 0\ell + \not{E}_T$	$\tilde{t}, \tilde{b}$	1308.2631	[111]
$4j + 1\ell + \not{E}_T$	$\tilde{t}$	ATLAS-CONF-2013-037	[112]
$\geq 2j + \geq 1\ell + \not{E}_T$	$\tilde{q}, \tilde{g}$ (1 or 2ℓ)	ATLAS-CONF-2013-062	[113]
$2j + 2\ell + \not{E}_T$	dilepton edge	CMS-PAS-SUS-12-019	[78, 79]
$2j + \ell^{\pm}\ell^{\pm} + \not{E}_T$	$\tilde{q}, \tilde{g}, \tilde{t}, \tilde{b}$ (SS lepton)	ATLAS-CONF-2013-007	[114]
$2j + 2\ell + \not{E}_T$	$\tilde{t}(2\ell)$	ATLAS-CONF-2013-048	[115]
		1403.4853	[116]
$2, 3\ell + \not{E}_T$	$\tilde{\chi}^{\pm}, \tilde{\chi}^0, \tilde{\ell}$	1404.2500	[117]
		1405.7570	[118]
$3\ell + \not{E}_T$	$\tilde{\chi}^{\pm}, \tilde{\chi}^0$	1402.7029	[75]
$\geq 3\ell + \not{E}_T$	$\tilde{\chi}^{\pm}, \tilde{\chi}^0$	CMS-PAS-SUS-13-002	[119]

TABLE 2.1: Complementary LHC searches used to test the viability of the simplified models.

of expected signal events calculated by `Atom` and CMS is shown in Appendix A. We also cross-checked some of the analyses with `CheckMATE` [108].

From the obtained cross section and efficiency, the SUSY contribution to the CMS dilepton excess is calculated as $N_{\ell\ell} = \sigma_{\text{eff}} \cdot \mathcal{L}$, where the effective cross section, σ_{eff}, is defined as the cross section after the event selection: $\sigma_{\text{eff}} = \epsilon \cdot \sigma_{\text{prod}}$. For the other ATLAS and CMS analyses the 95 % CL upper limit on σ_{eff}, σ_{UL}, is reported for each signal region by the collaborations. We define a useful measure for exclusion as $R = \sigma_{\text{eff}}/\sigma_{\text{UL}}$. The model is likely to be excluded if $R > 1$ is found for one of the signal regions. To draw a definite conclusion one should combine all signal regions statistically. Non-trivial correlations among them originating from the uncertainties on, *e.g.*, the jet energy scale or the lepton efficiencies, do not allow us to combine the signal regions correctly. Instead, we will look at the exclusion measure R of each signal region individually to understand which searches are most sensitive to the model points.

In Table 2.1 we list the ATLAS and CMS analyses we consider in this work. We

include the multi-jet [109, 110] and di-b jet [111] analyses, jets plus single [112] or two lepton [78, 79, 114] (including same-sign (SS) dilepton [114]) analyses [113] and multi-lepton analyses [75, 117–119].

In the next section we investigate whether the suggested SUSY models can fit the CMS dilepton excess and at the same time avoid constraints arising from these analyses.

2.4 Results

We have presented the simulation setup in the last section and explained the recasting of SUSY limits via an estimation of the efficiencies of the different signal regions. In this section we present the results for the sbottom scenarios. We start with the on-shell left-handed slepton model.

2.4.1 On-shell slepton models

In Fig. 2.7 we show $N_{\ell\ell}/130$ and R of the most constraining signal regions as functions of $m_{\tilde{b}_1}$. As discussed previously, we assume $m_{\tilde{\chi}_2^0} < m_{\tilde{b}_1} - m_t$ to avoid tops in the decay chains which would lead to more stringent constraints. Within this condition we examine four different mass gaps: $\Delta m \equiv m_{\tilde{b}_1} - m_{\tilde{\chi}_2^0} = 50$, 90, 130 and 170 GeV. The left-handed slepton mass is fixed at $m_{\tilde{\ell}_L} = m_{\tilde{\chi}_2^0} - 40$ GeV, which we found to maximise the contribution to the dilepton edge, and $m_{\tilde{\chi}_1^0}$ is set for each combination of $m_{\tilde{\chi}_2^0}$ and $m_{\tilde{\ell}_L}$ such that m_{edge} in Eq. (2.5) is 78 GeV. The intermediate slepton can either be a sneutrino or a charged slepton and the branching ratio of $\tilde{\chi}_2^0$ into these states is assumed to be equal. Therefore, only half of the produced $\tilde{\chi}_2^0$ decay into an OSSF dilepton pair and a $\tilde{\chi}_1^0$.

In Fig. 2.7 we see that a good fit can be obtained for sbottom masses between 420 and 520 GeV, depending on Δm. However, these model points are strongly disfavoured by the L100 and L110 signal regions of the ATLAS stop search [116].

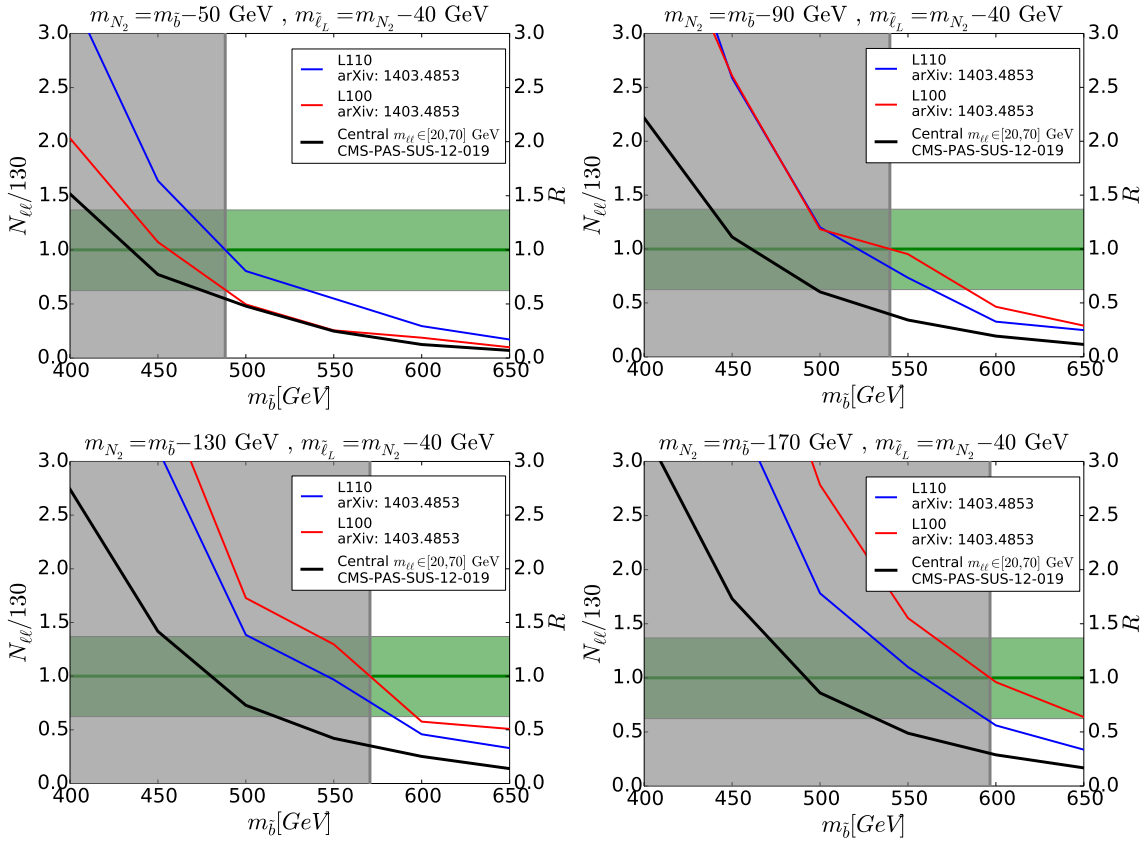

FIGURE 2.7: Signal rate and R-values for the on-shell left-handed slepton mediated sbottom models. The black line indicates the contribution to the dilepton signal region, the red and blue solid lines represent the exclusion limits from the L100 and L110 signal region of the ATLAS stop search [116], respectively. The green shaded area is the 1σ region around the best fit to the excess, whereas the grey shaded areas are disfavoured by the complementary searches.

The L110 signal region requires the same final state ($2j + 2\ell + \not{E}_T$) as the CMS dilepton analysis, in particular an OS lepton pair with $p_T > 25$ GeV and at least two jets with $p_T > 20$ GeV. The condition $m_{T2} > 110$ GeV is also imposed, which is very effective in reducing the $t\bar{t}$ and WW+jets backgrounds. The event selection in the L100 signal region is very similar to the L110 signal region. The difference is that the lepton p_T requirement is raised to $(p_T^{\ell 1}, p_T^{\ell 2}) > (100, 50)$ GeV and $m_{T2} > 100$ GeV is imposed. As the lepton p_T requirement is raised with respect to L110, L100 is especially sensitive to larger mass gaps.

In Fig. 2.8 we show the contribution to the excess and the constraints from other

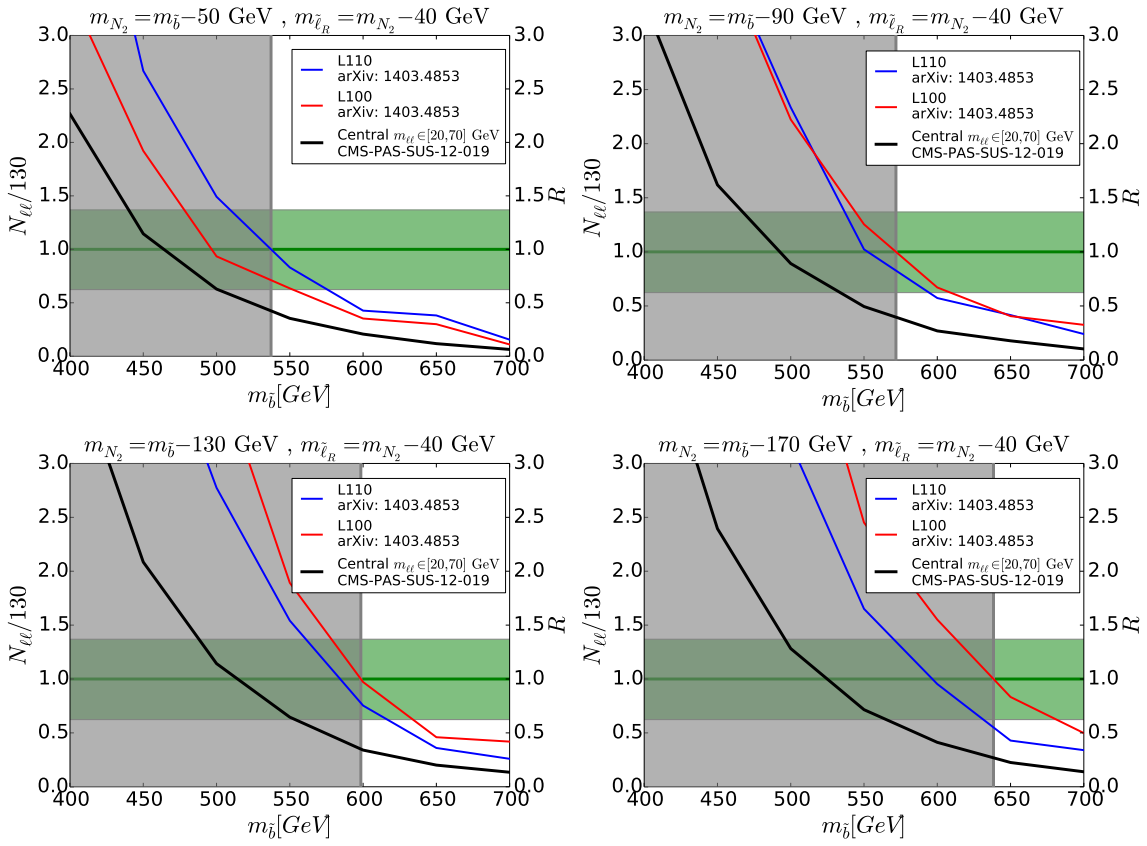

FIGURE 2.8: Signal rate and R-values for the on-shell right-handed slepton mediated sbottom models. Coloured lines and shaded regions are the same as before.

searches in the on-shell right-handed slepton model for the four different Δm, similarly to Fig. 2.7. In this scenario $\tilde{\chi}_2^0$ decays into an OSSF dilepton and a $\tilde{\chi}_1^0$ with the branching ratio of 100 %. The results are similar to the left-handed slepton case and the region where the model gives a good fit is strongly disfavoured by the L110 and L100 signal regions of the ATLAS stop search. The similarity of the results amongst the left- and right-handed slepton scenarios can be understood because the kinematics of the dilepton events are similar for these scenarios. Our choice of branching ratios within the slepton models was ad hoc when we proposed the models. Since the strongest constraints on these models arise from the stop search that has the same topology as the CMS dilepton analysis, this choice is however irrelevant to our conclusions. Changing the branching ratios of the sbottom decays would affect the dilepton signal region and L100/L110 from the stop search in the same way. We conclude that it is difficult to attribute the CMS dilepton excess to

the sbottom with on-shell slepton models if the constraint from the ATLAS stop search [116] is taken into account.

2.4.2 Off-shell Z models

We now turn to the sbottom with off-shell Z models. The first model we investigate is the right-handed sbottom model where $\tilde{\chi}_2^0$ and $\tilde{\chi}_3^0$ are mostly higgsino-like and $\tilde{\chi}_1^0$ is mostly bino-like. In this model the masses of three lightest neutralinos are calculated from the parameters, μ, M_1 and $\tan\beta$, fixing M_2 at 3.5 TeV. Since we assume $\mu > M_1$, we have $m_{\tilde{\chi}_3^0} \sim m_{\tilde{\chi}_2^0} \sim \mu$ and $m_{\tilde{\chi}_1^0} \sim M_1$ and both $\tilde{\chi}_2^0$ and $\tilde{\chi}_3^0$ can contribute to the excess through their decays into an off-shell Z boson and a $\tilde{\chi}_1^0$. The decay rate of the sbottom into the higgsino states is dictated by the sbottom-bottom-higgsino coupling which is proportional to $\tan\beta$. In order to have a large signal rate, we take $\tan\beta = 50$ in our numerical scan. We again examine four different mass gaps Δm = 50, 90, 130, and 170 GeV between the sbottom and $\tilde{\chi}_2^0$. To this end we vary μ such that $\tilde{\chi}_2^0$ takes the desired mass set by Δm. M_1 is chosen such that $m_{\tilde{\chi}_2^0} - m_{\tilde{\chi}_1^0} = 70$ GeV. The mass of the lightest sbottom is calculated from given parameters fixing the left-handed third generation squarks mass, $m_{\tilde{Q}_3}$, at 1.5 TeV. A table with parameter values for each model point can be found in the Appendix B.

In Fig. 2.9 we show our results again in terms of $N_{\ell\ell}/130$ and R. First we note that the strong constraint from L100 and L110 observed in the on-shell slepton models is relaxed. To understand this we compare the distributions of m_{T2} between the on-shell right-handed slepton (blue) and off-shell Z models (red) in Fig. 2.10 at similar mass spectra. We take $(m_{\tilde{b}_1}, m_{\tilde{\chi}_2^0}) = (400, 230)$ GeV and fix $m_{\tilde{\chi}_1^0}$ such that $m_{\rm edge} \simeq 78$ GeV for both models, and for the on-shell slepton model we take $m_{\tilde{\ell}} = 190$ GeV. In Fig. 2.10 we see that the off-shell Z model tends to give smaller m_{T2} compared to the on-shell slepton model. The solid (dashed) vertical black line represents the event selection cut on the m_{T2} variable employed in the L100 (L110)

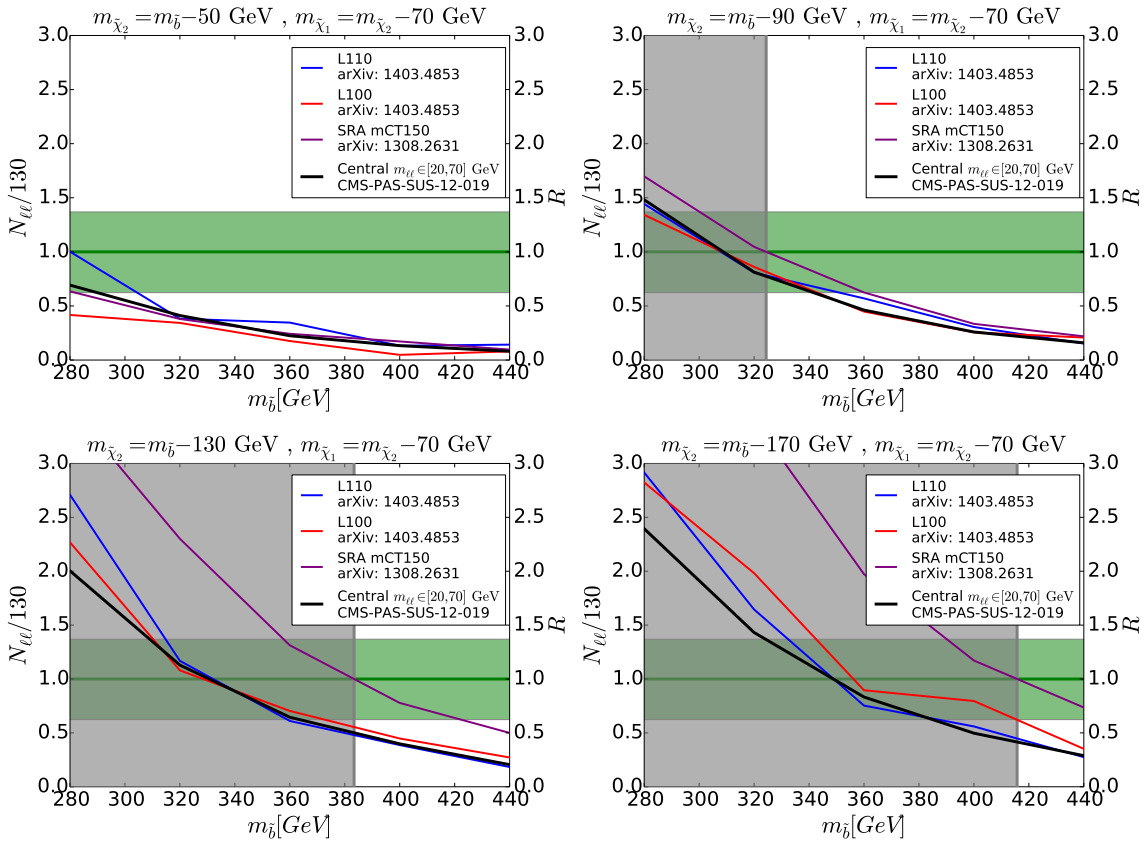

FIGURE 2.9: Signal rate and R-values for the off-shell Z-mediated right-handed sbottom-higgsino models. The purple line indicates the exclusion limit from the SRA mCT150 signal region of the ATLAS di-bottom analysis [111]. Other coloured lines and shaded areas are the same as before.

signal region. As can be seen, the off-shell Z model is less sensitive to the the L100 and L110 signal regions than the on-shell slepton model.

Figure 2.9 also shows that for $\Delta m > 90$ GeV the SRA mCT150 signal region in the ATLAS di-bottom analysis [111] is the most constraining and much of the preferred region of the dilepton excess is indeed disfavoured by this signal region. This search looks for two energetic b-jets with $p_T > 130$ and 50 GeV in events with $m_{\mathrm{CT}} > 150$ GeV [2] and $\not{E}_T > 150$. Events containing an electron ($p_T > 7$ GeV) or a muon ($p_T > 6$ GeV) are rejected in this analysis. This signal region is more constraining for larger Δm because the event selection requires two energetic b-jets.

[2] $m_{\mathrm{CT}} \equiv \sqrt{(E_T^{b_1} + E_T^{b_2})^2 - (\mathbf{p}_T^{b_1} - \mathbf{p}_T^{b_2})^2}$, where E_T and $\mathbf{p}_T$ are the transverse energy and the transverse momentum vector, respectively.

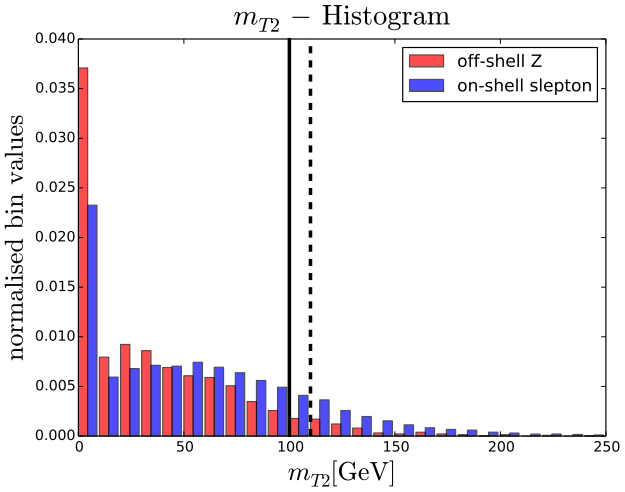

FIGURE 2.10: Histogram of m_{T2}-distribution for sbottom production for both the off-shell Z and on-shell RH-slepton mediated case. The sbottom mass is 400 GeV and $m_{\tilde{\chi}_2^0} = 230$ GeV. For the off-shell slepton mediated case we have $m_{\tilde{\mu}_R} = 190$ GeV and $m_{\tilde{\chi}_1^0} = 151$ GeV. The black solid (dashed) vertical line indicates the cut on m_{T2} from the L100 (L110) signal regions of the ATLAS stop search [116].

For $\Delta m = 50$ and 90 GeV we find the regions where the observed excess can be explained at 1-σ level without $R > 1$ from other searches. This result is consistent with the findings reported in [99]. The authors also discuss in their paper that the presence of light higgsinos allow for a large enough dark matter annihilation cross section to get the correct relic abundance. However the valid regions are already in tension with other searches. In particular the ATLAS stop [116] and ATLAS di-bottom searches [111] that were neglected in previous studies give values of R only slightly smaller than unity in these regions.

In Fig. 2.11 we show $N_{\ell\ell}/130$ and R as functions of $m_{\tilde{b}_1}$ in the left-handed sbottom model where $\tilde{\chi}_2^0$ ($\tilde{\chi}_1^\pm$) is assumed to be wino-like and decays predominantly to an off-shell Z (W) and a bino-like $\tilde{\chi}_1^0$. We again show the results for four different mass gaps and fix $m_{\tilde{\chi}_1^0} = m_{\tilde{\chi}_2^0} - 70$ GeV to fit the central value of the counting experiment. As we have mentioned in section 2.2, we assume the presence of the top squark, $\tilde{t}_1$, with $m_{\tilde{t}_1} = m_{\tilde{b}_1}$. The solid curves in Fig. 2.11 represent the results with both $\tilde{b}_1\tilde{b}_1^*$ and $\tilde{t}_1\tilde{t}_1^*$ production processes. To see the impact of $\tilde{t}_1\tilde{t}_1^*$ production

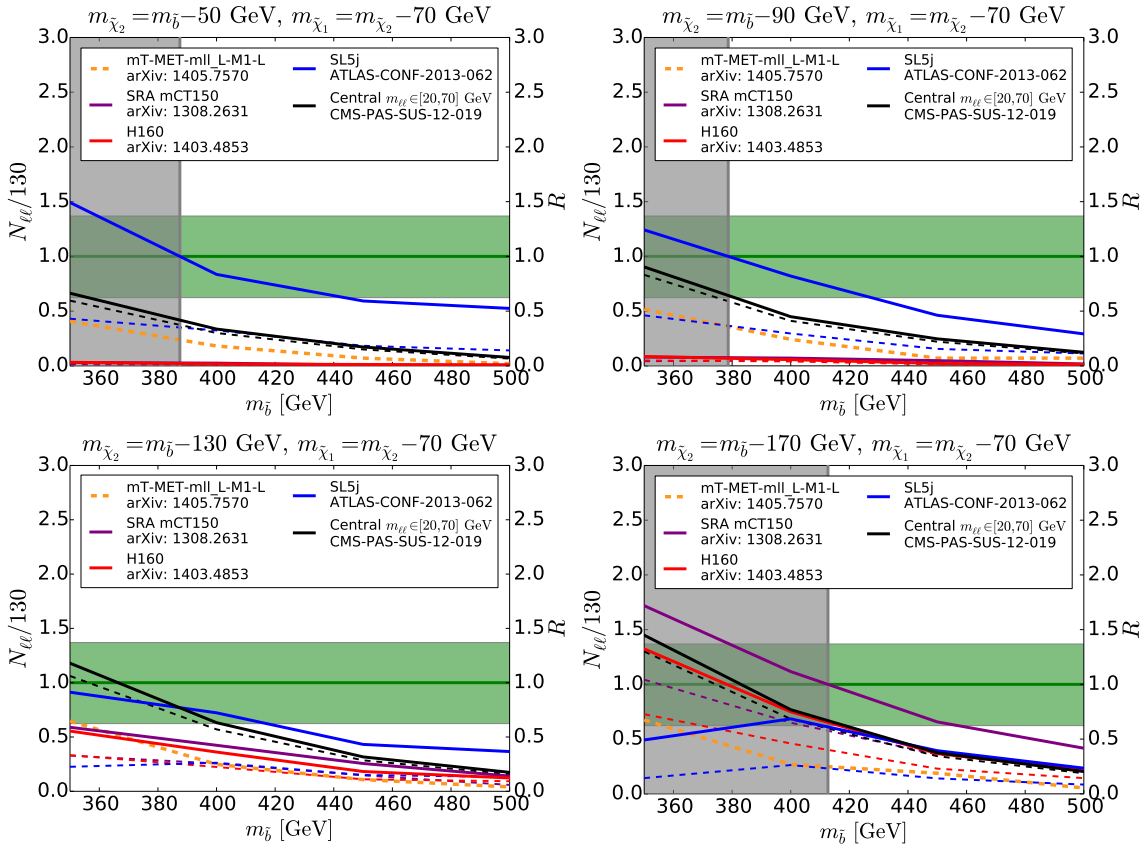

FIGURE 2.11: Signal rate and R-values for the off-shell Z-mediated left-handed sbottom model. Pure sbottom production is indicated by dashed lines and combined sbottom and stop production by solid lines.

on the result, we also plot the contribution to $N_{\ell\ell}/130$ and R solely from $\tilde{b}_1\tilde{b}_1^*$ using dashed curves.

One can see from Fig. 2.11 that for $\Delta m = 50$ and 90 GeV the model is strongly constrained by the SL5j signal region in the ATLAS jets plus 1-2 lepton analysis [113]. This signal region requires a soft single electron (muon) with $p_T \in [10, 25]$ ($[6, 25]$) GeV and veto additional electron (muon) with $p_T > 10$ (6) GeV. It also requires ≥ 5 jets with $p_T > (180, 25, 25, 25, 25)$ GeV. The SL5j signal region is more sensitive to the $\tilde{t}_1\tilde{t}_1^*$ topology where one of the stops decays hadronically $\tilde{t}_1 \to b\tilde{\chi}_1^\pm \to bW^*\tilde{\chi}_1^0 \to bqq'\tilde{\chi}_1^0$ and the other decays leptonically $\tilde{t}_1 \to b\tilde{\chi}_1^\pm \to bW^*\tilde{\chi}_1^0 \to b\ell\nu\tilde{\chi}_1^0$, because the event selection requires a single lepton. We also note that the SL5j signal region becomes less sensitive for larger Δm because the leptons from the stop cascade decay chain are boosted in this case and do not pass the low

p_T requirement (< 25 GeV) efficiently. However, for larger Δm the SRA mCT150 signal region becomes more constraining. In particular the preferred region for the dilepton excess is disfavoured by this signal region at $\Delta m = 170$ GeV.

As a result we find a good fit to the dilepton excess at $\Delta m = 130$ GeV and $m_{\tilde{b}_1} \in [350, 400]$ GeV, although this region is already in tension with the SL5j signal region in the ATLAS jets plus 1-2 lepton analysis. In addition, there is an additional constraint on the $\tilde{\chi}_1^0 - \tilde{t}_1$ mass plane from CMS single-lepton analysis [120], which is not included in our analysis. This analysis does not use the cut-and-count method but instead uses a multivariate Boosted Decision Tree method, which prevents us from implementing this analysis. While recasting this analysis is out of the scope of this work, it is worthwhile to deduce its constraint on our models. Specifically, the exclusion contour on the $\tilde{\chi}_1^0 - \tilde{t}_1$ mass plane with chargino mass fixed at $m_{\tilde{\chi}_1^\pm} = 0.25\ m_{\tilde{t}_1} + 0.75\ m_{\tilde{\chi}_1^0}$ in the CMS analysis is most relevant to the allowed parameter space in our study ($m_{\tilde{\chi}_1^\pm} \simeq 0.3\ m_{\tilde{t}_1} + 0.7\ m_{\tilde{\chi}_1^0}$). At $m_{\tilde{t}_1} \simeq 380$ GeV the CMS analysis excludes $m_{\tilde{\chi}_1^0} \lesssim 200$ GeV, while we find the best fit to the excess at values around $m_{\tilde{\chi}_1^0} = 180$ GeV and $m_{\tilde{t}_1} = 380$ GeV, as can be seen in the bottom left plot ($\Delta m = 130$ GeV) in Fig 2.11.

One might wonder whether electroweak production rules out this possible fit. As we mentioned earlier the mass limit for the LSP is about 160 GeV when the lightest chargino and second lightest neutralino decay via off-shell W or Z bosons. To fit the central value of the excess we would have here $m_{\tilde{\chi}_1^0} \approx 170$ GeV and $m_{\tilde{\chi}_2^0/\tilde{\chi}_1^\pm} \approx 240$ GeV, which is not yet excluded. Note again that electroweak production cannot contribute to the excess because of the presence of bottom quarks.

We will now investigate whether this set of parameters allows the neutralino to set the correct dark matter relic abundance. One way to achieve this for a bino-like LSP is the so-called *A-funnel*, where the CP-odd Higgs, A, serves as a s-channel resonance. For the mass spectrum that gives a good fit to the dilepton excess we have a LSP mass of around 160 GeV, such that A should weigh around 320 GeV. To obtain a good relic abundance we find that a large $\tan\beta$ is needed, which is

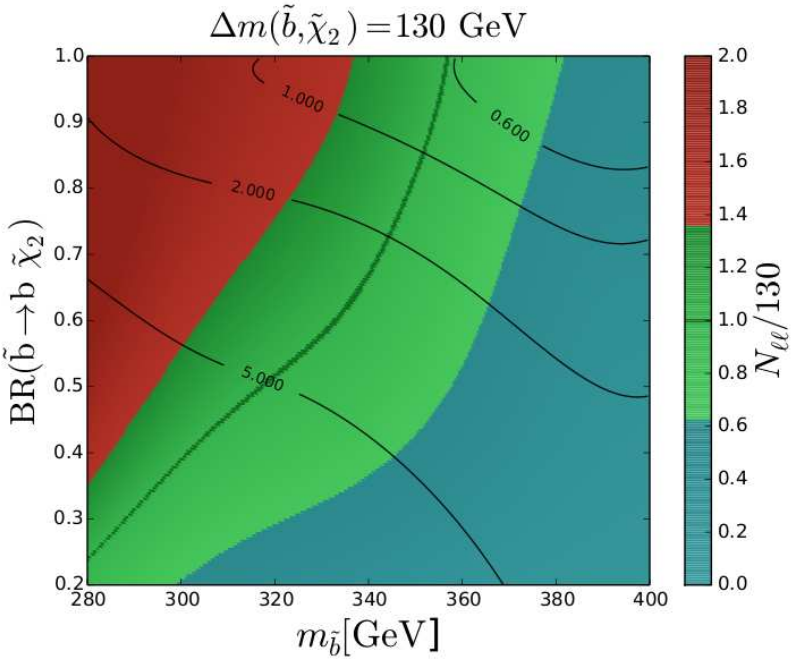

FIGURE 2.12: Variation of $\tilde{b}_1$ branching ratio into $\tilde{\chi}_2^0$ for off-shell Z mediated left-handed sbottom scenario with no stop production. The colour indicates $N_{\ell\ell}/130$ and the black curves are lines of constant $R_{\max}$.

excluded by searches for heavy Higgs bosons, see e.g. [121]. A second option would be to give a sizeable higgsino coupling to the LSP through a small μ parameter. To get a large enough annihilation cross section, we find that the higgsino, $\widetilde{\chi}_3^0$, is introduced into the spectrum and alters the decay channels of stop and sbottom. Hence, our simplified model is not representative and the dilepton excess is not fitted any longer. We conclude that a consistent dark matter relic density is not possible in the spectra that we considered.

It is interesting to see that the difference between the black solid and black dashed curves are small, whereas the difference is large amongst the blue solid and blue dashed curves in the bottom left plot ($\Delta m = 130$ GeV) in Fig 2.11. This means that the $\tilde{b}_1\tilde{b}_1^*$ production gives the main contribution to the dilepton excess, while the model is disfavoured mainly by the additional $\tilde{t}_1\tilde{t}_1^*$ production. Before concluding our study, in figure 2.12 we show the contribution to the dilepton excess and the constraint from other searches in the $m_{\tilde{b}_1}$ versus $BR(\tilde{b}_1 \to b\tilde{\chi}_2^0)$ plane concerning only the $\tilde{b}_1\tilde{b}_1^*$ production. In this study we assume $BR(\tilde{b}_1 \to b\tilde{\chi}_1^0) = 1 - BR(\tilde{b}_1 \to$

$b\tilde{\chi}_2^0$). The region is divided into 3 colours, (red, green and blue) which correspond to an under, good or over fit of the dilepton excess respectively. The R value of the most constraining signal region is shown in the black contours. One can see that a good fit is found for $m_{\tilde{b}_1} \in [340, 380]$ GeV and $BR(\tilde{b} \to b\tilde{\chi}_2^0) \gtrsim 0.8$ without having $R > 1$ from other searches. Within our exploration we did not find models where the sbottom is mostly right-handed and $BR(\tilde{b} \to b\tilde{\chi}_2^0) \gtrsim 0.8$ and it is difficult to achieve such a situation within the MSSM. This indicates that models that have a large cross section of the topology equivalent to $\tilde{b}_1 \to b\tilde{\chi}_2^0 \to bZ^*\tilde{\chi}_1^0$ can in principle explain the CMS dilepton excess avoiding constraints from other ATLAS and CMS direct SUSY searches.

2.5 Conclusions

The search for Supersymmetry is still ongoing and, if realised in nature, a first hint will eventually be observed at the LHC. We have investigated one such possibility here in the example of an observed dilepton excess that forms an edge in the dilepton invariant mass distribution [78, 79]. Such an edge is a characteristic SUSY signal if a particle undergoes a two-stage two-body or a three body decay. As there are b-jets associated with the excessive events we considered the decay of bottom squarks into neutralinos that then either undergo a cascade decay via an intermediate, on-shell slepton or an off-shell Z decay.

Constraints on the MSSM from collider searches at the LHC are model dependent and should ideally be reinterpreted for each given realisation of the parameters. One such an approach using the automated simulation tool `Atom` [103] and recasting existing limits onto our specific models to obtain solid statements about their viability has been chosen here. We selected a comprehensive list of LHC SUSY searches that constrain the relevant topologies.

The considered models are already in strong tension with the experimental data once we demand a good fit to the dilepton excess. In particular, strong limits

arise from an ATLAS stop search [116] with identical final state topology that has been neglected in other attempts to fit this excess. This analysis alone rules out the interpretation of the excess in terms of an intermediate left- or right-handed on-shell slepton, see Fig. 2.7 and Fig. 2.8, respectively. We confirmed the result reported in [99] and showed that the right-handed sbottom model with higgsino-like $\tilde{\chi}_2^0$ and $\tilde{\chi}_3^0$ decaying predominantly into an off-shell Z can explain the dilepton excess at 1σ level, although the model is already in tension with the ATLAS di-bottom search and the ATLAS stop search, as can be seen in Fig. 2.9.

This tension can be ameliorated if the left-handed sbottom model with wino-like $\tilde{\chi}_2^0$ is considered. However, the left-handed stop must be introduced in this model and creates tension with the ATLAS jets plus 1-2 lepton analysis as can be seen in Fig. 2.11. We have also shown that the neutralino cannot generate the correct dark matter relic abundance.

These results indicate that a more complex SUSY scenario should be considered to explain the CMS dilepton excess. It is also of general interest to further develop the automation tools for the recasting of limits.

Chapter 3

Deviations in the Higgs sector

One big problem of particle physics was that mass terms of gauge boson could not be constructed in a gauge invariant way. Hence, there was a problem of explaining boson masses that were highly expected ever since the formulation of Fermi's interaction in 1933 [122]. A possible way out was presented by Nambu [123] and Anderson [124] using the method of spontaneous symmetry breaking to preserve gauge invariance and generate a mass term dynamically for scalar particles. However, these theories always predicted the existence of massless "Nambu-Goldstone" bosons that were not observed in nature.

It was then shown by Brout and Englert [125], Higgs [126], and Guralnik, Hagen and Kibble [127] in 1964 that in a local gauge theory, the degrees of freedoms that formed the massless states disappeared from the theory. They instead form longitudinal modes of the gauge bosons that acquire a mass, a theory now simply known as the "Higgs mechanism". This breakthrough culminated in the formulation of the Standard Model by Weinberg [128] and Salam [129] who applied the concept to the unification of electromagnetic and weak forces as had been suggested by Glashow [130]. After the discovery of the top quark by the CDF and D$\emptyset$ group in 1995 [131, 132] the Higgs was then the last missing piece of the Standard Model.

The construction of the LHC was additionally motivated by the fact that the scattering amplitude of the longitudinal components of W bosons will violate unitarity at high energies if the Higgs is excluded from the SM. This formed the "No-Fail theorem" for the construction of the LHC. New physics had to show up to restore unitarity and the Higgs formed possibly the simplest realisation.

At last, the Higgs particle was found by the ATLAS and CMS experiments in 2012 [1, 2], a discovery that forms a great success for particle physics and finishes a quest that began more than forty years ago. The new resonance not only completed the SM, but at the same time opened up possibilities to look for new, beyond the Standard Model physics. Any deviation of the Higgs properties from expectations would be interpreted as a hint of new physics. Global fits of the Higgs data have shown that the new resonance indeed behaves like the expected SM Higgs boson [133–135]. Nevertheless, at that time the observed decay rate to two photons showed an excess in both experiments, ATLAS and CMS [136, 137]. We will take this as an example to discuss how deviations in the Higgs sector can hint at new physics. In this chapter we will address possible implications of an enhanced diphoton rate for dark matter and baryogenesis. We begin by reviewing Higgs production and decays at the LHC.

3.1 Introduction

3.1.1 Higgs production and decays

In this section we will summarise the main production and decay channels of the Higgs boson at the LHC. As the Higgs coupling to other SM particles is proportional to their masses, these channels mainly include the top and bottom quark and the W and Z bosons. The dominant production channel is gluon-gluon fusion via a virtual top quark loop, followed by vector boson fusion where the Higgs is produced together with two quarks. Associated production of the Higgs with a W or Z

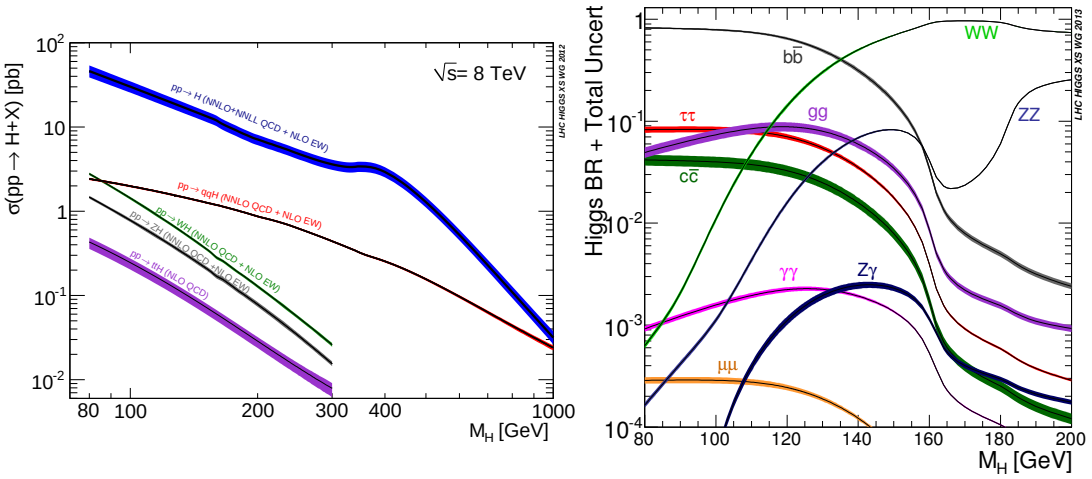

FIGURE 3.1: Dependence of Higgs production cross section and decay branching ratios on its mass as presented by the LHC Cross Section Working Group [138].

boson or a heavy quark pair forms another important production mode. Di-Higgs production is suppressed relative to these processes due to an additional weak coupling appearing in the Feynman graph. In the left panel of figure 3.1 we show the dependence of the different production cross sections on the Higgs mass for a centre of mass energy $\sqrt{s} = 8$ TeV, as presented by the LHC Higgs Cross Section Working Group [138].

Similarly, the Higgs decay into the heaviest, kinematically accessible particle will have the largest branching ratio. Hence, the dominant decay into quarks will produce bottom quarks and the dominant leptonic decay will have a tau pair in the final state. At the measured Higgs mass of 125 GeV the Higgs can only decay into two gauge bosons if one of them is virtual. Nevertheless, the branching ratio into WW^* is only slightly smaller than the branching ratio into $b\bar{b}$.

Decays to massless particles such as gluons or photons are induced via loops. The Higgs to di-gluon decay is the reverse of the gluon-gluon fusion production mode where a heavy quark runs in a loop. Decays into $Z\gamma$ are induced via W bosons running in the loop. The same process also allows for a Higgs to diphoton decay,

which gets an additional contribution from fermion loops. The right panel of figure 3.1 summarises the dependence of branching ratios of possible Higgs decays on the Higgs mass, again taken from the LHC Cross Section Working Group. Since we are interested in the enhanced Higgs to diphoton rate, we will discuss this decay channel in greater detail in the next section.

3.1.2 Diphoton excess

Both CMS and ATLAS experiments measured an enhancement of the Higgs decay into two photons. In terms of the signal strength, $\mu = \sigma/\sigma_{\rm SM}$, the excess in the diphoton channel was measured to be 1.6 ± 0.4 in the CMS and 1.8 ± 0.5 in the ATLAS experiment [1, 2]. Here, σ is the inferred cross section from the data and $\sigma_{\rm SM}$ the cross section expected from the SM for a fixed Higgs boson mass. These were later refined to 1.56 ± 0.43 [137] and 1.65 ± 0.24 [136], respectively. Even though these measurements do not form a statistically significant deviation from the expectations, it was intriguing at that time that both independent experiments measured a slight excess.

New data has moved the signal strengths into regions that are consistent with the SM predictions. The most recent ATLAS and CMS analysis find values of 1.17 ± 0.27 and 1.14 ± 0.21, respectively, [139, 140]. Nevertheless, we will use this as an example to show how deviations in the Higgs sector could point to models beyond the SM. In this chapter we suggest possible relations to dark matter and, simultaneously, to baryogenesis. Let us review the Higgs decay into two photons first.

As discussed in the last section this loop-induced decay mode has two main contributions coming from W bosons and top quarks running inside the loop. The decay rate is given by [141, 142]

$$\Gamma(h \to \gamma\gamma) \propto \left| A_1(\tau_W) + \frac{4}{3} A_{1/2}(\tau_t) \right|^2 , \tag{3.1}$$

where A_1 and $A_{1/2}$ are loop functions for bosons and fermions, respectively, and $\tau_x = \frac{m_h^2}{4m_x^2}$. The factor 4/3 in front of the top contribution originates from $N_c \cdot Q^2$ with $N_c = 3$ as the number of colours and $Q = 2/3$ as the electric charge. The loop functions are

$$A_{1/2}(\tau) = \frac{2\left(\tau + (\tau - 1) f\left(\tau\right)\right)}{\tau^2} \,, \tag{3.2}$$

$$A_1(\tau) = -2 - \frac{3}{\tau} - \frac{3\left(2\tau - 1\right) f\left(\tau\right)}{\tau^2} \,, \tag{3.3}$$

for fermions and bosons, respectively, where the function $f(\tau)$ is given by

$$f\left(\tau\right) = \begin{cases} \arcsin^2 \sqrt{\tau} & \text{for } \tau \leq 1 \,, \\ -\frac{1}{4}\left(-i\pi + \log\left[\frac{1+\sqrt{1-\tau^{-1}}}{1-\sqrt{1-\tau^{-1}}}\right]\right)^2 & \text{for } \tau > 1 \,. \end{cases} \tag{3.4}$$

Being boson and fermion, the amplitudes of W and top quark have opposite signs such that destructive interference occurs. Their single contributions are $A_1(\tau_W) = -8.32$ and $4/3\, A_{1/2}(\tau_t) = 1.84$ showing that the W contribution dominates. In order to enhance the decay rate into two photons, we either have to mimic the bosonic contribution or overcompensate with a larger fermionic contribution. We will chose the first way here and mimic bosons using vector-like leptons. As we shall see such a model will provide a valid dark matter candidate and has interesting consequences for the strength of the electroweak phase transition. In the next section we present the Lagrangian.

3.2 Vector-like leptons

Vector-like leptons are leptons whose left and right handed components transform in the same way under the standard model gauge groups. Past works have demonstrated that not only can vector-like fermions enhance the diphoton rate [143–149], but also that there are possible connections to other phenomena such as dark matter [150–153] or baryogenesis [154]. We take this as a motivation to examine these connections in greater detail - in particular we aim to explore the compatibility of

Field	$\ell'_{\rm L}, \ell''_{\rm R}$	$e'_{\rm R}, e''_{\rm L}$	$\nu'_{\rm R}, \nu''_{\rm L}$
$\mathrm{SU(3)} \times \mathrm{SU(2)} \times \mathrm{U(1)}$	(1,2,-1/2)	(1,1,-1)	(1,1,0)

TABLE 3.1: $\mathrm{SU(3)} \times \mathrm{SU(2)} \times \mathrm{U(1)}$ quantum numbers of the new fermion fields.

an explanation of both dark matter and baryogenesis within one single setup of vector-like fermions and see what its implications for the Higgs diphoton rate are.

In this chapter we investigate the model proposed in reference [150]. We will use the exact same notation here in order to avoid unnecessary confusion and present the Lagrangian and resulting mass matrices. Note that such a model may arise by gauging lepton number, as explained in references [153, 155, 156].

The model consists of a SU(2) doublet ℓ'_L with standard model type couplings as well as corresponding singlets e'_R and ν'_R plus, to make it vector-like, mirrored fields with opposite chirality. See also table 3.1 for clarification of the different fields and their quantum numbers. The Lagrangian is given by,

$$\begin{aligned} \mathcal{L} \;=\; & \mathcal{L}_{\rm SM} - m_\ell \bar{\ell}'_{\rm L} \ell''_{\rm R} - m_e \bar{e}''_{\rm L} e'_{\rm R} - m_\nu \bar{\nu}''_{\rm L} \nu'_{\rm R} - \frac{1}{2} m' \overline{\nu'^{\,c}_{\rm R}} \nu'_{\rm R} - \frac{1}{2} m'' \overline{\nu''^{\,c}_{\rm L}} \nu''_{\rm L} \\ & - Y'_c (\bar{\ell}'_{\rm L} H) e'_{\rm R} - Y'_n (\bar{\ell}'_{\rm L} \tau H^\dagger) \nu'_{\rm R} - Y''_c (\bar{\ell}''_{\rm R} H) e''_{\rm L} - Y''_n (\bar{\ell}''_{\rm R} \tau H^\dagger) \nu''_{\rm L} + \text{h.c.}\,. \end{aligned} \tag{3.5}$$

Here, the symbol τ represents the antisymmetric 2×2 matrix in SU(2) space with non zero components $\tau_{12} = 1$ and $\tau_{21} = -1$. There are therefore nine free parameters of the model - five masses and four Yukawa couplings. With $v = 246$ GeV one obtains the following mass matrices for the charged sector

$$\left(\overline{e'_{\rm L}}\ \overline{e''_{\rm L}}\right) \mathcal{M}_c \begin{pmatrix} e'_{\rm R} \\ e''_{\rm R} \end{pmatrix} + \text{h.c.} \qquad \text{with} \qquad \mathcal{M}_c = \begin{pmatrix} \frac{Y'_c v}{\sqrt{2}} & m_\ell \\ m_e & \frac{Y''_c v}{\sqrt{2}} \end{pmatrix}, \tag{3.6}$$

and for the neutral sector,

$$\frac{1}{2}\left(\overline{\nu'_{\mathrm{L}}}\ \overline{\nu'^{\,c}_{\mathrm{R}}}\ \overline{\nu''^{\,c}_{\mathrm{R}}}\ \overline{\nu''_{\mathrm{L}}}\right)\mathcal{M}_n\begin{pmatrix}\nu'^{\,c}_{\mathrm{L}}\\ \nu'_{\mathrm{R}}\\ \nu''_{\mathrm{R}}\\ \nu''^{c}_{\mathrm{L}}\end{pmatrix}+\mathrm{h.c.}\quad\text{with}\quad\mathcal{M}_{\mathrm{n}}=\begin{pmatrix}0 & \frac{Y'_n v}{\sqrt{2}} & m_\ell & 0\\ \frac{Y'_n v}{\sqrt{2}} & m' & 0 & m_\nu\\ m_\ell & 0 & 0 & \frac{Y''_n v}{\sqrt{2}}\\ 0 & m_\nu & \frac{Y''_n v}{\sqrt{2}} & m''\end{pmatrix}. \tag{3.7}$$

These matrices are diagonalised such that we obtain the masses and mixing elements of the physical states. This is done with a Singular Value Decomposition in the charged fermion sector that requires two independent unitary matrices U_L and U_R, whereas one unitary matrix V is sufficient for the Takagi decomposition that is applied in the neutral sector, where Majorana states are present [157]. In the following we will use the symbols $N_{1,2,3,4}$ and $E_{1,2}$ for the mass eigenstates of the neutral and charged fermions, respectively. Their masses will be written as $M_{N_{1,2,3,4}}$ and $M_{E_{1,2}}$ and their couplings to the Higgs boson as, e.g., $C^{N_1 N_1 h}$ or $C^{E_1 E_1 h}$. Note that there is no mixing between the new vector-like and the SM fermions, such that the lightest, neutral new state will be stable and forms a dark matter candidate.

In the following analysis we will examine whether this dark matter candidate can give rise to the correct relic abundance while avoiding constraints arising from direct detection searches. It will be of further interest to us how the Higgs diphoton rate is altered and if the strength of the EWPT can be increased such that the third Sakharov condition is fulfilled. Electroweak precision measurements and collider constraints have to be respected. We will explain our scanning procedure of the nine dimensional parameter space in the next section.

3.3 Methodology

After presenting the model in the last section, we will now present how we examine the complete accessible nine dimensional parameter space. We restrict the parameter ranges are as follows:

$$\begin{aligned} m' &\in [0, 4000] \text{ GeV}, & m'' &\in [0, 4000] \text{ GeV}, & m_\ell &\in [0, 4000] \text{ GeV}, \\ m_\nu &\in [0, 4000] \text{ GeV}, & m_e &\in [0, 4000] \text{ GeV}, & Y_c' &\in [0, 3.6]\,, \\ Y_c'' &\in [0, 3.6]\,, & Y_n' &\in [0, 3.6]\,, & Y_n'' &\in [0, 3.6]\,. \end{aligned}$$

The upper limits on the mass parameters are set to 4 TeV because we would enter the decoupling regime for larger masses. We implement perturbativity by setting an upper limit on the Yukawa couplings of $\sqrt{4\pi} \approx 3.6$.

For the mass matrix diagonalisations we rely on the routines from the SLHAplus package [158]. As we expect the expressions for the masses and mixing elements to be too complicated to be illuminating, we perform the complete analysis without considering analytic expressions. We demonstrate the impact of these new fermions on the Higgs to diphoton decay in the next section.

3.3.1 Diphoton rate

In the last section we have introduced our model of vector-like fermions and pointed out that a dark matter candidate exists. We will now outline how the charged fermions alter the Higgs diphoton rate. Since our vector-like fermions are colour singlets they do not change the production cross sections of the Higgs boson. Hence, the excess in the Higgs diphoton channel is characterised by the ratio of the decay rates only:

$$R_{\gamma\gamma} = \frac{\sigma(pp \to h)}{\sigma_{\text{SM}}(pp \to h)} \frac{\Gamma(h \to \gamma\gamma)}{\Gamma(h \to \gamma\gamma)_{\text{SM}}} = \frac{\Gamma(h \to \gamma\gamma)}{\Gamma(h \to \gamma\gamma)_{\text{SM}}}. \tag{3.8}$$

The extended version of the diphoton decay rate that we presented earlier is [143, 144, 150]

$$\Gamma(h \to \gamma\gamma) \propto \left| A_{\rm SM} + \frac{C^{E_1 E_1 h} v}{\sqrt{2} M_{E_1}} A_{1/2}(\tau_{E_1}) + \frac{C^{E_2 E_2 h} v}{\sqrt{2} M_{E_2}} A_{1/2}(\tau_{E_2}) \right|^2 . \tag{3.9}$$

This form of the adapted diphoton rate suggests that the new fermions behave just like the SM top quark. However, the couplings $C^{E_i E_i h}$ behave differently if the masses of the vector-like fermions *decrease* during electroweak symmetry breaking [143, 144]. This can be understood more clearly when we look at a different formulation of the Higgs-γ-γ coupling. Using an effective QED Lagrangian in the presence of heavy fermions the coupling may be written as [143],

$$\begin{aligned} C_{h\gamma\gamma} &= \frac{\alpha\, b_{1/2}}{16\pi} \frac{\partial}{\partial v} \log\left(\det \mathcal{M}_f^\dagger \mathcal{M}_f\right) \\ &= \frac{\alpha\, b_{1/2}}{16\pi} \frac{\left(m_{11}^2 \frac{\partial}{\partial v} m_{22}^2 + m_{22}^2 \frac{\partial}{\partial v} m_{11}^2 - \frac{\partial}{\partial v} |m_{12}^2|^2\right)}{\left(m_{11}^2 m_{22}^2 - |m_{12}^2|^2\right)} , \end{aligned} \tag{3.10}$$

where α is the QED coupling constant, $b_{1/2} = 4/3$ for a colour singlet fermion with unit charge and a fermion mass matrix, $\mathcal{M}_f^\dagger \mathcal{M}_f$, as

$$\mathcal{M}_f^\dagger \mathcal{M}_f = \begin{pmatrix} m_{11}^2 & m_{12}^2 \\ m_{12}^{*2} & m_{22}^2 \end{pmatrix} . \tag{3.11}$$

If there is no mixing between the new fermions ($|m_{12}^2| = 0$) the coupling will be positive and the top-quark contribution will be copied. If the mixing is non-zero and independent of the vev the coupling will again be positive, because the determinant of $\mathcal{M}_f^\dagger \mathcal{M}_f$ appearing in the denominator of equation 3.10 has to be positive definite. If, on the other hand, the mixing has a dependence on the vev the Higgs-γ-γ coupling may be negative. This is the case for our model of vector-like fermions. This behaviour is incorporated in equation 3.9 because the couplings $C^{E_i E_i h}$ depend on the mixing elements.

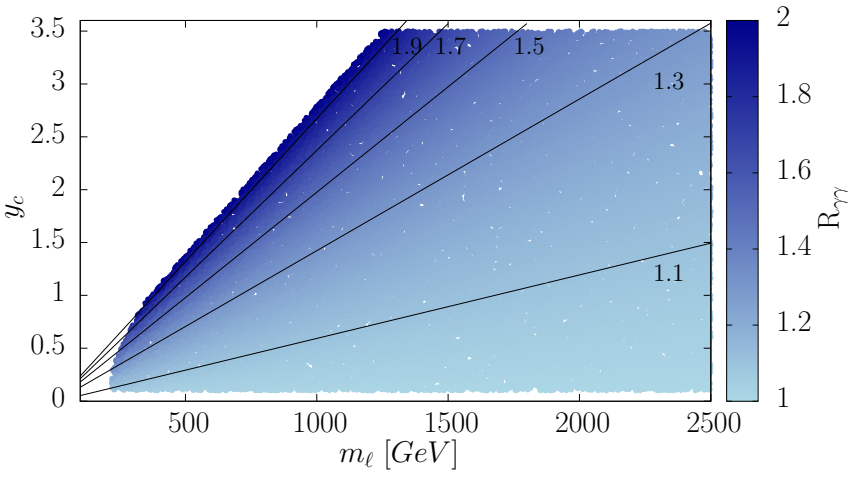

FIGURE 3.2: Diphoton rate and its dependence on the doublet mass parameter m_ℓ and the Yukawa coupling y'_c. m_e and y''_c are fixed to 482 GeV and 2.82, respectively. The lines indicate an enhanced branching ratio from 1.1 to 1.9.

To show the general dependence of the diphoton rate on the parameters, we show for completeness in figure 3.2 how $R_{\gamma\gamma}$ behaves under a variation of m_ℓ and y'_c. For a fixed m_ℓ the diphoton rate becomes stronger with an increasing Yukawa coupling, and for a fixed Yukawa coupling $R_{\gamma\gamma}$ decreases while m_ℓ increases. These are the expected general trends which have been discussed in the literature, see e.g. [143–150, 159, 160]. In everything that follows all accepted scenarios have an enhanced Higgs diphoton branching ratio between 1 and 2.

Not only can the new fermions change the Higgs decays, they may also affect the self-energies of the weak gauge bosons that are strongly constrained by electroweak precision test. We will discuss these *oblique* parameters in the next section.

3.3.2 Oblique parameters

New particles that are too heavy to be produced at a particle collider might leave traces if their quantum corrections show large effects on well studied phenomena. Heavy new fermions, as we are considering here, couple to the weak gauge bosons

and contribute to their self-energies via loop effects. These oblique corrections, often described in terms of the Peskin-Takeuchi parameters S, T, and U, are strongly constrained by electroweak precision measurements.

Contributions to U are generally suppressed by a factor $(m_Z/\Lambda)^2$ compared to S or T, where Λ is the scale of new physics. We therefore neglect U in our analysis. S and T are defined as [161]:

$$S = 16\pi \frac{d}{dq} \left[\Pi_{33}(q^2) - \Pi_{3Q}(q^2)\right] |_{q^2=0} \,, \tag{3.12}$$

$$T = \frac{4\pi}{c_W^2 s_W^2 M_Z^2} \left[\Pi_{11}(0) - \Pi_{33}(0)\right] \,, \tag{3.13}$$

where Π_{33}, Π_{3Q} and Π_{11} denote gauge boson self energies. The expressions for the S and T parameters for our model have been derived in [150], see also [162, 163]. The allowed ranges for a Higgs mass of 125 GeV are $S = 0.04 \pm 0.09$ and $T = 0.07 \pm 0.08$ where the errors are correlated with a coefficient of 0.88 [164], forming a diagonally oriented error ellipse in the S-T plane.

To get a qualitative understanding of these parameters, let us review some limiting cases. For vanishing Yukawa couplings the new fermions do not affect S or T. The same is true when transitioning into the decoupling regime by increasing the explicit mass terms. Because T is sensitive to isospin violation, it receives corrections proportional to the square of the mass difference between partners in a doublet [161]. The larger the explicit mass terms are, the larger the mass splitting may be. The parameter S may, for small mass splittings, be interpreted as a measure of the size of the new sector. As shown in [161], a single fermion doublet gives a contribution of $1/(6\pi)$ to S up to logarithmic corrections arising from mass differences. For a set of two degenerate fermion doublets a contribution to S of approximately 0.106 is expected, which we can confirm with our numerical implementation.

In our analysis we evaluate S and T for each model point and veto if it falls out of the 95% confidence region. We show the distribution of our models in figure 3.3.

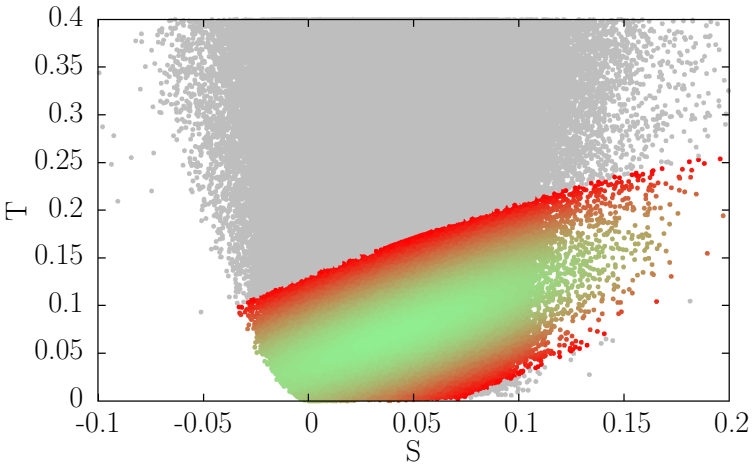

FIGURE 3.3: 95% confidence region of the S and T parameters. Grey models which lie outside this region are rejected before any subsequent analysis.

The coloured region is part of the ellipse which represents the error on S and T and the correlation between those errors.

Besides creating oblique corrections the new fermions could be produced directly at particle accelerators. In the next section we will summarise current collider constraints.

3.3.3 Collider constraints

After the presentation of corrections to oblique parameters in the last section, we will now discuss constraints from collider physics. Since we do not assume any mixing of the new fermions with the SM fermions, constraints from flavour physics do not apply to our model. However, electroweak production at colliders could give signals. At the LHC the production would proceed vis s-channel Z, W or γ exchange with subsequent decays as follows:

$$E_1 \rightarrow N_1 + W \tag{3.14}$$

$$N_2 \rightarrow N_1 + Z \tag{3.15}$$

These decays are similar to wino-like chargino/neutralino decays (like the left-handed sbottom model with off-shell Z decay in chapter 2) and their mass limits can give indications. Note, however, that the mass limits that are given in figure 2.1 assume mass degenerate $\tilde{\chi}_2^0$ and $\tilde{\chi}_1^\pm$ which would translate into degenerate N_2 and E_1 here, which is not the case. Hence, simply applying the chargino/neutralino mass limits would be too constraining. We decide to apply the LEP limit of 103.5 GeV for any chargino [51] to the new charged fermions here as a first estimate.

A detailed collider study that applies to our model is missing in the literature. One could think of recasting existing limits on charginos and neutralinos to apply them to this model, similarly to our investigations in chapter 2, but such an approach is beyond the scope of this analysis. Similar assumptions on mass limits were taken in [144, 150].

In the next section we will present additional constraints on our model that arise when we demand the lightest neutral state to be a valid dark matter candidate.

3.3.4 Dark matter

Having outlined general collider constraints in the last section, we will now review the constraints that apply specifically to the dark matter candidate.

Results from LEP constrain the mass of an additional Majorana neutrino to be above 39 GeV [51, 165]. Whereas this limit might in some cases be avoided due to the mixing of the DM candidate with singlet fields, which results in a suppressed coupling to the Z-boson, it still serves as a good first estimate. This is because in the low dark matter mass region a sizeable DM-Z coupling must be present for consistent relic abundance. Hence, we show this limit as a dotted, vertical black line at 39 GeV in following plots.

Constraints arising from the dark matter sector include the relic abundance, direct searches and the invisible branching ratio of the Higgs $\mathrm{BR}_{\mathrm{inv}}$. The Lagrangian is expressed in the language of LanHEP [166] such that we can use micrOMEGAs [167]

to calculate the relic abundance, Ωh^2, and the spin-independent WIMP-Nucleon cross section σ^{SI}. We demand the relic density to lie in the range $[0.1134, 0.1258]$ as has been measured by the Planck collaboration [22] and apply the strong limits on σ^{SI} by the XENON100 collaboration [168]. These were the strongest constraints on the model when this analysis was first conducted. Recently, Planck has made their measurement on the relic density more precise using the full data set [23] and more stringent limits on σ^{SI} come from the LUX collaboration [44]. However, these updated limits do not change our qualitative conclusions and we do not apply them here.

If the Higgs boson is kinematically allowed to decay into two dark matter particles, a significant contribution to $\mathrm{BR}_{\mathrm{inv}}$ may arise, which is constrained by the Higgs data. We will apply a rather strong limit in this analysis by demanding $\mathrm{BR}_{\mathrm{inv}} < 0.2$, following the global fits performed in references [133–135]. The invisible branching ratio was calculated using CalcHEP [169].

As we have remarked before we will not only investigate the dark matter candidate of the model, but also the possibility of altering the strength of the electroweak phase transition with the new fermions. We will describe this in more detail in the next section.

3.3.5 Baryogenesis

To find out whether the model can achieve a strong first order phase transition, we evaluate the full free energy density $\mathcal{F}$ up to first loop order numerically. It can be decomposed as

$$\mathcal{F}(\phi, T) = V_{\mathrm{SM}}(\phi) \pm \sum_i g_i V(m_i^2(\phi)) + T^4 \sum_i g_i I_{\mp}\left[m_i(\phi)/T\right]/2\pi^2, \qquad (3.16)$$

where the first term $V_{\mathrm{SM}}(\phi) = -\frac{1}{2}\mu^2\phi^2 + \frac{1}{4}\lambda\phi^4$ is the tree level Higgs potential, the second term contains one-loop contributions with a plus for bosons and a minus sign for fermions, and the last term represents the thermal corrections with the

integrals $I_{\mp}$ defined below. T is the temperature, g_i the degrees of freedom and $m(\phi)$ the field dependent masses. Both sums run over all Standard Model particles and the new vector-like fermions. We neglect SM leptons and quarks other than the top, because they have negligible effects due to their small couplings to the Higgs.

The one-loop contributions can be expressed as [170–172]

$$V(m^2(\phi)) = \frac{1}{64\pi^2}\, m^4(\phi) \log m^2(\phi) + P(\phi), \tag{3.17}$$

with the polynomial $P(\phi)$ that depends on the renormalisation conditions.

$$P(\phi) = \frac{1}{2}\alpha\, \phi^2 + \frac{1}{4}\beta\, \phi^4. \tag{3.18}$$

Here we chose renormalisation conditions that do not change the tree level vacuum expectation value and the Higgs mass (which we fix to 125 GeV) such that the parameters in the polynomial are fixed to [173]

$$\begin{aligned} \alpha &= \frac{1}{64\pi^2}\left\{\left(-3\,\frac{\omega\omega'}{v} + \omega'^2 + \omega\omega''\right)\log\omega - \frac{3}{2}\frac{\omega\omega'}{v} + \frac{3}{2}\omega'^2 + \frac{1}{2}\omega\omega''\right\}, \\ \beta &= \frac{1}{128\pi^2 v^2}\left\{2\left(\frac{\omega\omega'}{v} - \omega'^2 - \omega\omega''\right)\log\omega + \frac{\omega\omega'}{v} - 3\omega'^2 - \omega\omega''\right\}, \end{aligned} \tag{3.19}$$

with

$$\begin{aligned} \omega &= m^2(v)\ , \\ \omega' &= \left.\frac{dm^2(\phi)}{d\phi}\right|_{\phi=v}, \\ \omega'' &= \left.\frac{d^2m^2(\phi)}{d\phi^2}\right|_{\phi=v}. \end{aligned} \tag{3.20}$$

For the vector-like fermions, we evaluate these derivatives numerically by fitting a polynomial to $m^2(\phi)$ paying attention to possible points where the function may not be differentiable.

The last part of equation (3.16), the thermal corrections, include the integrals [174]

$$I_{\mp}(x) = \pm \int_0^\infty dy\, y^2 \log\left(1 \mp e^{-\sqrt{y^2+x^2}}\right), \tag{3.21}$$

where I_- is the contribution from bosons and I_+ from fermions.

The goal is that the new fermions induce a barrier in the Higgs potential at finite temperatures such that a second minimum arises. The EWPT is then first order and the third Sakharov condition can be fulfilled if the order parameter, the ratio of the vev of the second minima at the critical temperature to the critical temperature, v_c/T_c, is greater than unity. The critical temperature is defined as the temperature when both minima are degenerate. In this case sphaleron processes are sufficiently suppressed in the broken phase and a baryon asymmetry can be generated.

The effect that strengthens the phase transition in this model is described in [154]. Temperature corrections can drive the effective quartic coupling λ_{eff} negative while μ_{eff} becomes positive, resulting in a barrier at finite temperature. A positive ϕ^6 term stabilises the potential up to some energy scale. In [154] the effect was discussed in a model with a doublet and a singlet fermion. When the heavier state is integrated out and the high temperature expansion of the full potential is considered, logarithmic terms in the effective quartic coupling and T^2 terms in μ_{eff} create the desired temperature dependence.

Large Yukawa couplings necessary for the barrier intuitively stand in conflict with the oblique parameters and the dark matter sector, because large Yukawa couplings may quickly lead to an underproduction of dark matter and to a WIMP-Nucleon cross section above current exclusion limits. A detailed discussion of the model is thus necessary and we investigate in the following the compatibility of those constraints all together.

Let us mention another way to obtain a first order phase transition with fermions. The mechanism in [173] relies on decoupling of heavy fermions from the plasma when they enter the broken phase resulting in a delay of the phase transition

towards cooler temperatures and enhancing its strength in this way. Since we want to enhance the diphoton rate, some of our particles become lighter when they enter the broken phase. Hence, this effect is not the driving force behind our barrier.

We used existing works in the literature and Mathematica to cross-check our numerical results for the mass diagonalisations, Higgs diphoton rate, electroweak precision tests and the Higgs potential and conclude our presentation of the methodology. In the next section we present our numerical results. First we examine the viability of the dark matter candidate on its own and then investigate the compatibility of successful baryogenesis and dark matter simultaneously. We will relate both phenomena to the diphoton rate.

3.4 Results

Here we will present the results of the applied procedures outlined in the previous section and show how the different criteria affect the parameter space of our model.

To explore the parameter space we initially used a naive Monte Carlo scanning technique but we then moved on to a basic version of a Metropolis Hastings Monte Carlo Markov chain (MCMC) to search for good parameters more efficiently, especially to find regions with a strong first order phase transition.

There are some plots which are the result of naive parameter scans where we vary the parameters randomly. Such plots (e.g. figure 3.5) will have, for example, very few points which are not excluded by the XENON-100 bound on the WIMP-nucleon cross section. This told us that we had to scan the parameter space more intelligently such that we implemented the MCMC technique. Including the XENON-100 bound as a fitness criteria, the Markov chain hence concentrated on acceptable regions and the shape of the plots changed significantly (see, e.g. figure 3.9).

We do not claim to have made a completely comprehensive scan of the parameter space, but we have gone to some effort within the ranges described above to look

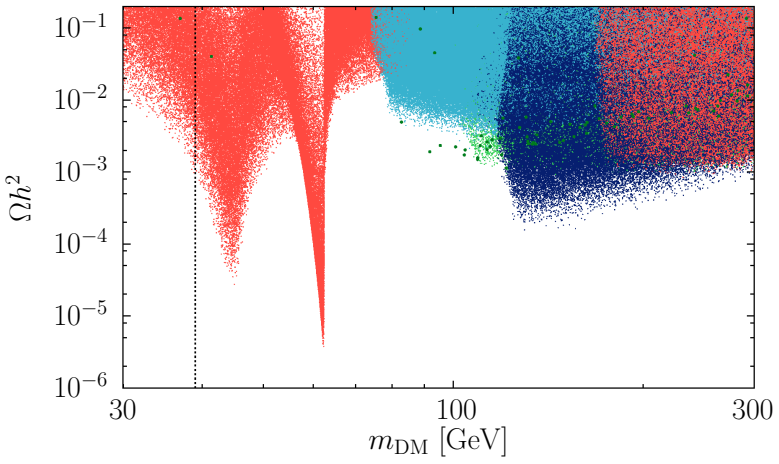

FIGURE 3.4: Relic density and the dominant annihilation channel responsible for relic abundance. Red points represent annihilation into quark pairs, light blue points into gauge boson final states and dark blue points into a pair of Higgs bosons while light and dark green points denote co-annihilation with the lightest charged or next-to-lightest neutral fermion, respectively. In this and all following plots, the dotted vertical line shows the LEP exclusion for an additional Majorana neutrino.

for parameter combinations which satisfy all of our requirements (dark matter, baryogenesis, not too large S and T parameters) which also have Yukawa couplings as small as possible, in order to retain perturbativity.

One relic of our slightly incomplete scanning procedure is that the careful reader may be able to spot some lines on the scatter plots which are not due to any physical mechanism, but rather due to the behaviour of one of the MCMC chains as it explores the parameter range. We have tried to identify which features are physical and which are random and hopefully made this distinction clear through drawing attention to real features using colour coding and careful wording in the figure captions. We start with the presentation of the results related to the dark matter candidate.

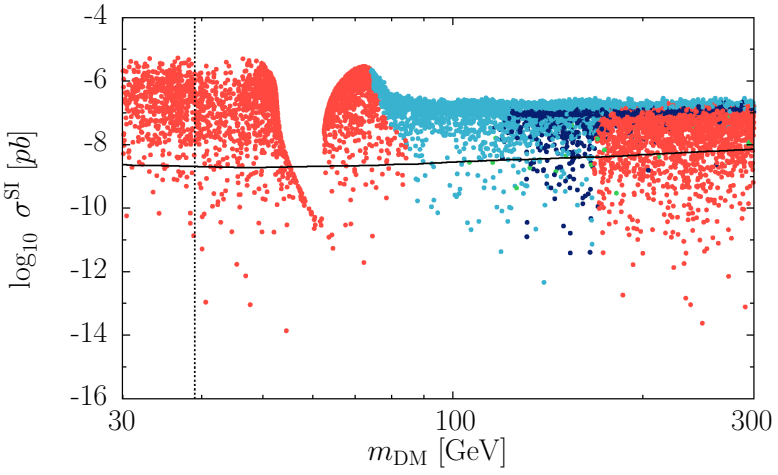

FIGURE 3.5: WIMP-Nucleon cross section σ^{SI} and the dark matter mass. All points give the correct dark matter relic abundance and are colour coded by the dominant annihilation channel responsible for relic abundance. Colour coding as in figure 3.4. In this and all following plots the solid black line shows the XENON100 (2012) exclusion limit.

3.4.1 Dark matter

We extend existing discussions about dark matter in this model [150] by presenting results from an investigation of the complete parameter space performing a simple Monte Carlo scanning. In figure 3.4 we show the relic abundance and the different annihilation mechanisms that dominate during the freeze-out process. The shape is characterised by different resonances and thresholds.

At a dark matter mass of about 45 GeV and at approximately 65 GeV the Z- and h-resonances appear with a dominant decay into quark/antiquark pairs (mainly $b\bar{b}$), represented by the red points. The red scenarios at masses above 170 GeV denote $t\bar{t}$ final states. Above $m_{\mathrm{DM}} \approx 80$ GeV the possible annihilation into two W-bosons (and later also Z-bosons) comes along with another decrease in the relic abundance (light blue points). A similar feature is observed at the Higgs threshold at 125 GeV (dark blue points). Coannihilations with the lightest charged vector-like fermion E_1 (light green) set in at approximately 100 GeV while coannihilations with the second lightest neutral state N_2 (dark green) can be present at any mass range. In

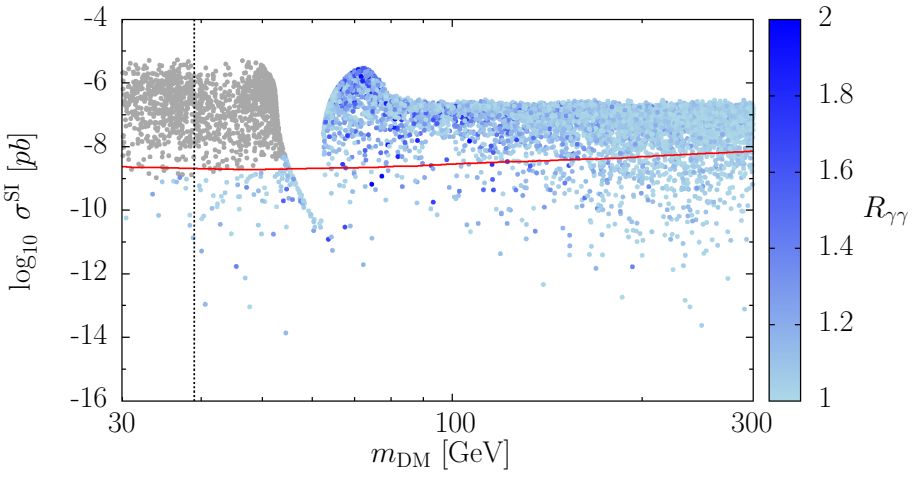

FIGURE 3.6: WIMP-Nucleon cross section σ^{SI} and the dark matter mass of a general scan. The blue colour indicates an enhanced Higgs to diphoton branching fraction. Grey points are excluded due to invisible Higgs decays.

this and all following plots the dotted, vertical black line indicates the mass limit from LEP for an additional Majorana neutrino of 39 GeV.

We note here, that this picture can and will change when we concentrate on certain regions of the parameter space, as we will do when we discuss baryogenesis. Coannihilations, which seem to under-produce dark matter here, will become important as the dominant mechanism to set the relic abundance.

In figure 3.5 we present the mapping of those scenarios that fulfil the relic density condition (i.e. $\Omega h^2 \in [0.1134, 0.1258]$) into the direct detection plane. We have again colour coded the diagram so that it is easy to see the different sections of the diagram where different mechanisms dominate the relic abundance calculation. It is visible that direct detection limits can be avoided in the complete mass range. Since the scattering process for the WIMP-nucleon cross section is mediated by the Higgs, σ^{SI} indicates the coupling of our dark matter particle to the Higgs. This is best seen at the h-resonance itself: To obtain the correct relic abundance, the resonantly enhanced annihilation rate asks for a a suppressed dark matter Higgs coupling, which translates into a suppressed σ^{SI}.

The dark matter discussion is to some extent independent of an enhanced diphoton rate, since the latter one is solely fixed by the charged sector. However, we note that the vector mass parameter for the doublet fields, m_ℓ, relates both sectors and can give rise to some correlations.

In figure 3.6 we show the diphoton rate in the direct detection plane with a blue colour coding and can observe a general trend of a decreasing excess in the diphoton channel towards larger dark matter masses. This is because the charged states must become heavier and their contribution to the diphoton rate gets suppressed as the dark matter mass increases.

In this plot we also apply the constraint from the invisible branching ratio of the Higgs boson. Every scenario with $\mathrm{BR}_{\mathrm{inv}} > 0.2$ is coloured grey and therefore excluded. As expected, these scenarios populate light dark matter masses with a large WIMP-Nucleon cross section. If the LHC achieves a higher sensitivity for the invisible branching ratio, we can expect this constraint to become more important for light dark matter masses and eventually be stronger than direct searches.

Additionally, we cross-checked the predictions of the spin-dependent WIMP-Nucleon cross section σ^{SD} with the current limits from the XENON100 collaboration [175], but found them to be not constraining yet. Hence, we see that we find consistent realisations of the model at every accessible dark matter mass.

A complimentary approach to detect dark matter are indirect searches that look for annihilation products in dark matter dominated regions. The light end of the dark matter spectrum here annihilates preferably into $b\bar{b}$ final states that are strongly constrained by measurements of the gamma ray flux of dwarf spheroidal galaxies by FERMI-LAT [30]. Annihilation cross-sections below the one of a canonical WIMP are currently tested for dark matter masses below around 100 GeV. For Majorana dark matter it is known that the velocity independent part of the annihilation process suffers a helicity suppression. For annihilations away from resonances one can approximate $\langle \sigma v \rangle \approx a + bv^2$ and for Majorana dark matter $b \gg a$. Note in this context that today's dark matter velocity is around $v \approx 10^{-3}$ whereas at freeze out

it is around $v \approx \sqrt{x_f} \approx 0.3$. Hence, even though the correct annihilation cross section existed in the early Universe to create the correct relic abundance, by now it might have dropped by several orders of magnitude, such that the experiments do not probe the annihilation yet. We found that for the light candidates in this model today's annihilation cross section is around $10^{-29}\text{cm}^3\text{s}^{-1}$, calculated by micrOMEGAs [25], which is far below the probed region of parameter space. Note that the velocity independent part suppression may be enhanced via gauge boson and Higgs Bremsstrahlung [176, 177].

In this section we have proved that the lightest neutral state is a valid dark matter candidate over a wide mass range and calculated its direct detection cross section. In the next section we will demonstrate that the EWPT can be enhanced such that sufficient deviation from thermal equilibrium is given for successful baryogenesis.

3.4.2 Baryogenesis

We have seen in the last section that this model has a viable dark matter candidate. In this section we will test whether the model can create large deviations from thermal equilibrium for baryogenesis. In order to work out if a given set of parameters leads to a strong first order phase transition, we look at the free energy equation (3.16) and iteratively vary the temperature until we get a phase transition. We then look for first order phase transitions and quantify the order parameter, v_c/T_c, to see if sphaleron processes are suppressed at and below the temperature of the phase transition, preventing washout of any baryon asymmetry. We have analysed all the points we have found with good relic abundances in order to see which parameter sets give rise to a strong first order phase transition. In figure 3.7 we colour code models with a smooth cross-over or a weak phase transition light-grey, and those with $v_c/T_c > 1$ dark-grey or in a red colour scale. Dark-grey points are excluded by the invisible branching ratio of the Higgs boson, whereas the red points fulfil all constraints considered in this analysis.

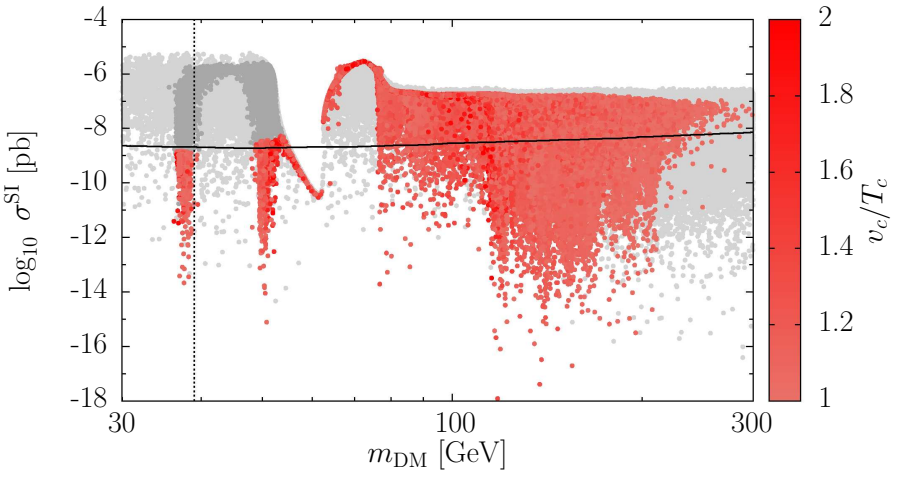

FIGURE 3.7: WIMP-nucleon cross section $\sigma^{\rm SI}$ and the dark matter mass of models that respect dark matter and electroweak constraints. Light-grey coloured scenarios only have a cross-over or a weak first order phase transition, while red and dark-grey scenarios give a strong first order phase transition. Dark-grey points are, however, ruled out due to the invisible Higgs decay width.

We can observe interesting behaviour at low dark matter masses. There are two dips surrounding the Z-resonance and a thin band along the h-resonance. This pattern is closely related to the constraints on the mixing of the dark matter candidate arising from demanding that we can get a strong first order phase transition. In figure 3.8 we show how strongly constrained the mixing becomes once we apply the baryogenesis condition $v_c/T_c > 1$. We show as an example the second mixing element V_{21} and note that similar plots exist for the other three elements. Again, grey points satisfy electroweak and dark matter constraints and the red points additionally the baryogenesis condition.

At the Z- resonance and at a mass around 70 GeV, one can observe that $|V_{21}|^2$ is always non-zero if we want to get a first order phase transition. As this holds for all the other mixing elements as well[1], we can understand why no suppression of $\sigma^{\rm SI}$ occurs. Since the direct detection process proceeds via Higgs exchange, $\sigma^{\rm SI}$ will be proportional to the Higgs coupling of the dark matter candidate, C^{N_1hh}, which

[1]Of course unitarity requests some of them to be small, but around the Z-resonance they are still significantly further away from zero than in other regions.

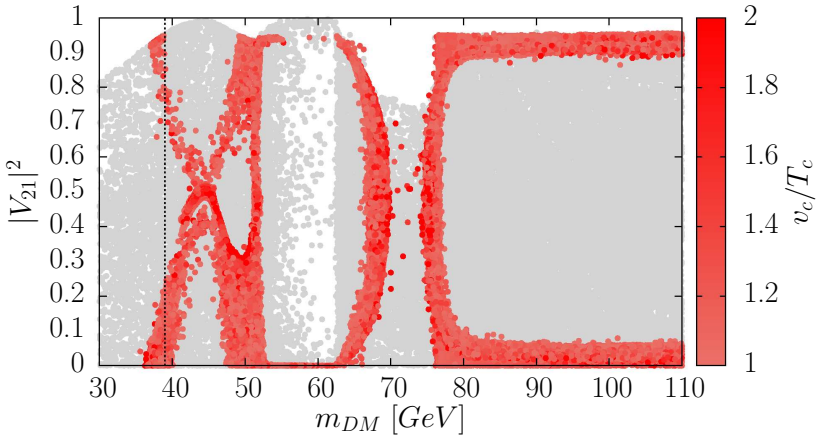

FIGURE 3.8: Second mixing element of the dark matter candidate and the dark matter mass. Grey points fulfil electroweak and dark matter constraints, while red points additionally give a strong first order phase transition.

is given by:

$$\begin{aligned} C^{N_1hh} &= \frac{y'_n}{\sqrt{2}} \left(V_{11}^* V_{21}^* + V_{11} V_{21}\right) + \frac{y''_n}{\sqrt{2}} \left(V_{31}^* V_{41}^* + V_{31} V_{41}\right) \\ &= \sqrt{2}\, y'_n\, \mathrm{Re}(V_{11} V_{21}) + \sqrt{2}\, y''_n\, \mathrm{Re}(V_{31} V_{41})\,. \end{aligned} \tag{3.22}$$

For a suppressed direct detection rate, we generally need one of the mixing elements in each product to be suppressed which cannot be achieved around the Z-resonance if we demand that the vector-like fermions are important for baryogenesis.

A second thing to note in figure 3.7 is the tendency of smaller order parameters towards larger dark matter masses. This is again explained through approaching the decoupling limit. As all masses increase, the behaviour of the free energy becomes more and more Standard Model like and the first order phase transition gets weaker and weaker. This puts an upper limit on the dark matter candidate of around 300 GeV.

In figure 3.9 we look at the same data as in figure 3.7 but this time we colour code the annihilation channels. With this plot we can now understand the sharp edge

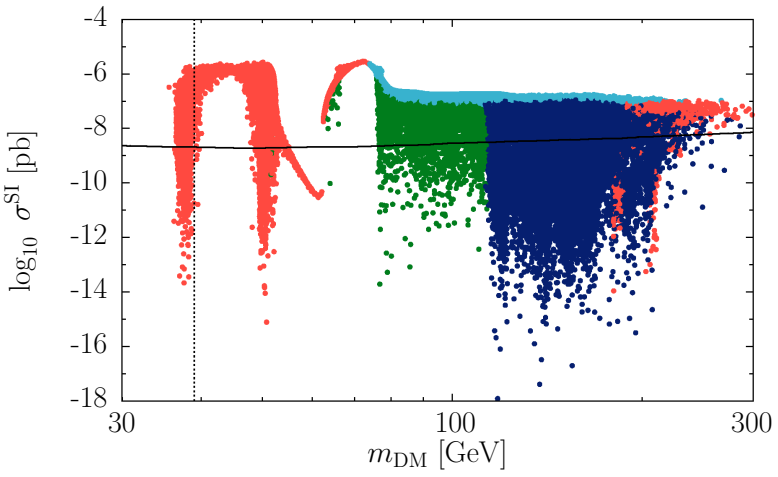

FIGURE 3.9: WIMP-Nucleon cross section $\sigma^{\rm SI}$ and the dark matter mass. All scenarios produce the correct dark matter relic abundance and give a strong first order phase transition. They are colour coded by the dominant annihilation channel responsible for relic abundance. Colour coding as in figure 3.4.

setting in slightly below 80 GeV in figure 3.7. There, coannihilations of the dark matter particle with the second lightest neutral state into two W-bosons set in. The following dip at 125 GeV can now be understood with the possible annihilations processes into two Higgs bosons. We note here again, that we do expect paradoxes with figure 3.4 and 3.5 where coannihilations seemed to be unimportant for the relic abundance, because we changed our scanning procedure in such a way that we find interesting regions where baryogenesis is possible.

It is clear that we can obtain strong first order phase transitions and good dark matter abundance whilst avoiding the XENON100 bound. There are regions at particular masses below 125 GeV and for a range of masses above 125 GeV. We would like to learn more about the characteristics of the parameters which satisfy these criteria, but with nine free parameters there are many combinations which can lead to good results. There is however one feature of the parameter sets which gives rise to strong first order phase transitions, and that is that they usually require large Yukawa couplings between the Higgs and the additional fermions. In order to show this behaviour we look at a first benchmark point (BM1), which

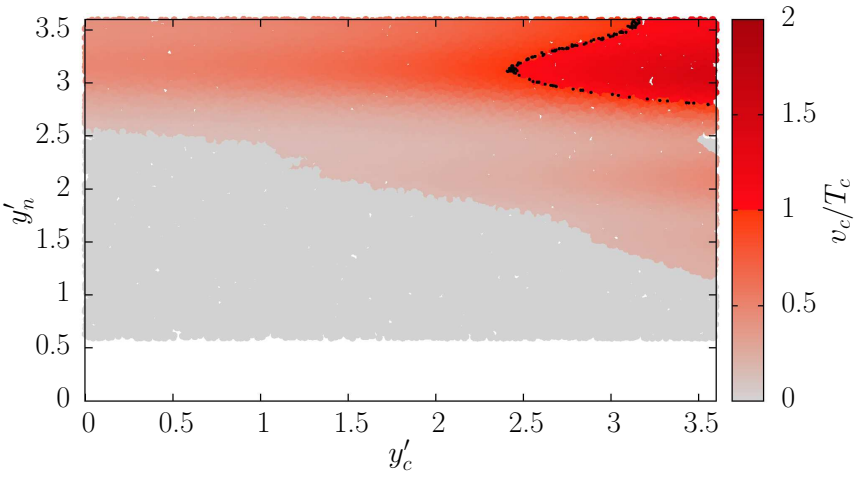

FIGURE 3.10: The order parameter and its dependence on the primed charged and neutral Yukawa couplings. The black points have an order parameter of one and indicate the switchover from a weak to a strong first order phase transition. All other parameter of our benchmark point BM1 have been fixed. Note that as we vary the Yukawa couplings from the benchmark point, the other constraints (S and T parameters, dark matter relic abundance, XENON100 limit and diphoton bound) may be violated.

has been chosen because it satisfies all the requirements we have in terms of dark matter and baryogenesis with relatively small Yukawa couplings (relative to other parameter sets that give us baryogenesis). See table 3.2 for the numerical values of the parameters. We then vary the Yukawa couplings to see the effect upon the strength of the phase transition.

Figure 3.10 shows the order of the phase transition as a function of the primed charged and neutral Yukawa couplings. While both Yukawa couplings increase the order of the phase transition, it seems that for the benchmark point the neutral Yukawa takes the lead role in realising baryogenesis. It becomes clear that a large ratio v_c/T_c only appears for large Yukawa couplings.

Related to this need for large Yukawa couplings, we point out that an enhanced diphoton rate is unavoidable if the fermions should cause the phase transition to be strongly first order. All simulated scenarios with $v_c/T_c > 1$ have a minimal enhancement of $R_{\gamma\gamma}$ of 1.1. As we mentioned in section 3.1, both experiments now

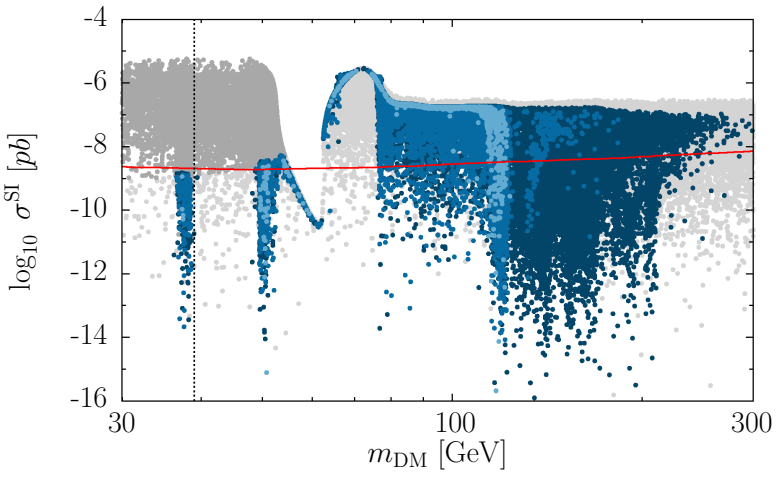

FIGURE 3.11: WIMP-Nucleon cross section $\sigma^{\rm SI}$ and the dark matter mass. The solid red line is the XENON100 (2012) limit. All scenarios give the correct relic abundance and respect electroweak precision tests. Dark grey points are, however, excluded by the invisible branching ratio of the Higgs. Blue models additionally give a strong first order phase transition. The three blue tones indicate different upper limits on the diphoton excess $R_{\gamma\gamma}$. From dark to light, the corresponding upper limits on $\mathrm{R}_{\gamma\gamma}$ are 1.5, 1.3 and 1.2.

measure a diphoton decay rate that is consistent with the SM and it is doubtful whether vector-like fermions are responsible for baryogenesis. At the current state, however, the diphoton signal strengths are also compatible with a slight enhancement such that this model is still valid at this level of precision. Future runs of the LHC and a detailed collider study would help to clarify the situation.

New data coming from the current LHC run will clarify the Higgs to diphoton rate which will place tight constraints upon this set of models. It will be interesting to discover which regions of the parameter space will still be available if the constraints on this rate are increased.

To explore this further, we show in figure 3.11 regions of models that explain both dark matter and baryogenesis, colour coded according to the value of the excess in the diphoton channel. As in the rest of the chapter, we show a background of light-grey points that give a dark matter candidate fulfilling the relic density condition and electroweak constraints with an excess in the diphoton channel between 1 and

2. Dark grey points are, however, ruled out by the upper limit on the invisible branching ratio of the Higgs. All blue points additionally give a strong first order electroweak phase transition and form the scenarios consistent with all our applied constraints. The different shades of blue indicate different upper limits on $R_{\gamma\gamma}$ ranking from 1.5 (darkest blue) via 1.3 (middle tone) to 1.2 (lightest blue). We can see that if in the future the excess in the diphoton channel consistently decreases in both experiments, scenarios at high dark matter masses will be ruled out. In those regions, all new vector-like fermions are relatively heavy and for successful baryogenesis the charged Yukawa couplings need to be close to their largest possible value still consistent with perturbativity, which comes along with a relatively large enhancement in the diphoton decay channel. Related to this we note again that all scenarios with a strong first order phase transition show an enhancement of $R_{\gamma\gamma}$ of at least 10%. This demonstrates how a better limit from the LHC in that channel can rule out electroweak baryogenesis within this model.

3.4.3 Vacuum stability

It is known that adding fermions to the SM may create a problem of vacuum (in)stability. If the SM alone is extrapolated to higher energies, it seems as if we live in a metastable Universe, i.e. a Universe that will eventually tunnel into the lower energetic, second minimum, but with a lifetime in the current state of more than its age [178–180]. This occurs due to the negative contribution of the top quark. Adding new fermions will shift the second minimum (which may be unbounded from below) to smaller energies and make the problem more severe. We estimate in this section at which energy scale this instability appears.

We define the instability scale Λ as the scale for which the potential takes a value smaller than the current minimum. For clarity, we set $V(v) = 0$. We plot in figure 3.12 potentials of our two benchmark points and indicate the largest fermion mass with a vertical red line. The second benchmark point is chosen with Yukawa couplings close to the perturbativity limit because one would expect the instability

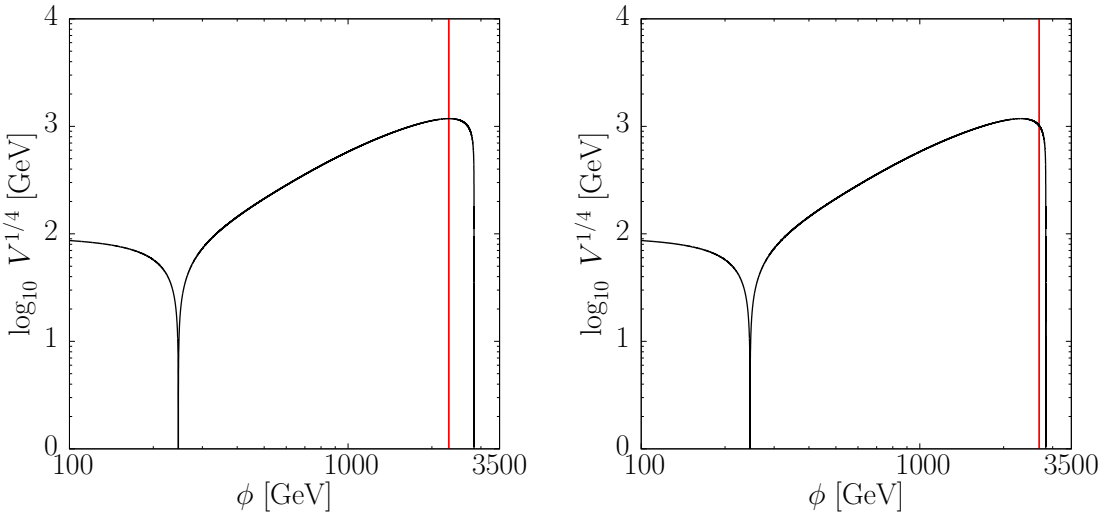

FIGURE 3.12: Zero temperature Higgs potential for benchmark point 1 (left panel) and 2 (right panel). The scale of instability occurs above the largest fermion mass eigenvalue (red vertical line).

problem to be worse for larger couplings. For consistency the instability scale has to be larger than the heaviest fermion. In figure 3.12 we see that this is the case for both benchmark points. In table 3.2 we give their specific parameters and in table 3.3 the mass eigenvalues as well as the instability scale. We checked that all our model points fulfil this consistency condition.

Even though our approach is consistent, the problem of vacuum instability is severe and shows that the model needs extra particle states to stabilise the vacuum. We did not investigate this in more detail in this analysis, however, let us briefly discuss a possible solution. In contrast to fermions, new bosonic states contribute positively to the running of λ_{eff}. Hence, we could think of introducing, e.g., an additional scalar. Of course, if this scalar has a mass comparable to the light fermions in our

	m'	m''	m_ℓ	m_ν	m_e	y'_c	y''_c	y'_n	y''_n
BM1	97.70	90.90	2172.0	124.50	482.80	2.73	2.82	2.98	2.99
BM2	869.53	236.57	2514.70	215.13	445.66	3.59	3.48	3.06	2.88

TABLE 3.2: Parameters of two benchmark points considered in the model. Mass parameters are given in GeV.

	m_{N_1}	m_{N_2}	m_{N_3}	m_{N_4}	m_{E_1}	m_{E_2}	Λ
BM1	85.96	92.42	2291.24	2301.45	354.62	2300.23	2833.23
BM2	210.11	841.35	2605.85	2660.49	276.74	2683.68	2857.79

TABLE 3.3: Masses and instability scale in GeV for both benchmark points.

model, it would influence electroweak physics as well and strongly influence our results. Hence, for our approach to be valid we must demand these new states to be below the instability scale, but around the mass of the heaviest fermion. Also, a solution would be supersymmetric versions of vector-like fermions, as investigated in for example [149, 181, 182].

3.5 Conclusions

The measurement of the Higgs boson has given us a new tool to look for physics beyond the Standard Model. In this chapter we have shown one such example using the excessive Higgs to diphoton decay rate as had formerly been measured by ATLAS and CMS. We introduced vector-like fermions to mimic the bosonic contribution for enhancement of the diphoton decay rate. These new fermions not only include a viable dark matter candidate, but also have the possibility to alter the Higgs potential such that the electroweak phase transition becomes strongly first order.

In section 3.4.1 we saw that this WIMP can give rise to the correct DM relic abundance in the Universe in the complete mass range that we investigated. We showed in figure 3.4 which mechanisms are the most important ones for effective annihilation in the early Universe and looked at their mapping into the direct detection plane in figure 3.5. We saw that the invisible branching ratio of the Higgs can cut into the parameter space, but is not yet sensitive enough to be more important than direct detection limits on the WIMP-Nucleon cross section σ^{SI}.

We have investigated the effect upon electroweak baryogenesis of these extensions to the Standard Model detailed in section 3.4.2 and showed that one can obtain a strong first order electroweak phase transition if the diphoton channel is enhanced by at least 10%. Therefore this type of model enables the kind of out-of-equilibrium physics required to fulfil the third Sakharov condition. We have noted that in order to obtain successful baryogenesis, one requires relatively large Yukawa couplings between the new states and the Higgs, compare to figure 3.10. These Yukawa couplings can potentially serve as a possible new source of CP-violation.

If we demand that this extra sector provides both our dark matter and a strong first order electroweak phase transition simultaneously, there are quite large ranges of possible dark matter masses between 39 GeV and 300 GeV with notable absences of models where the dark matter mass is around 45 GeV or 70 GeV, as can be seen in figure 3.7 and 3.11. We hence find that both these problems of modern particle physics can be addressed within this single setup of vector-like fermions.

The best fitting values of the top quark mass and the Higgs mass suggest that our current electroweak vacuum is metastable [178–180]. The addition of fermions will generically worsen this situation, such that the quartic coupling becomes negative at lower energies (as pointed out by the authors of [144]). In section 3.4.3 we argued that if the scenario set out in this chapter turned out to be true, it would be a strong indication of additional particles at higher energies. These would cure this vacuum stability issue by adding positive contributions to the beta function for the quartic coupling.

It would be interesting to investigate the impact that these heavier states can have on the electroweak phase transition. Additionally, a detailed collider study on this kind of vector-like fermions is of high interest.

Chapter 4

Direct searches and the neutrino background

Within the WIMP paradigm there is dark matter scattering off baryonic matter. Great effort is undertaken to directly detect dark matter via these scattering processes in Earth-based, low-background direct search experiments.

The need for an almost background-free search environment originates from the extremely small dark matter event rates. Whereas experiments have managed with great success to keep reducible backgrounds to a minimum, non-reducible backgrounds coming from neutrino-nucleus scattering will create a problem for future searches. It has been shown that neutrinos from the Sun, from supernovae and from cosmic ray collisions with atoms in the atmosphere will lead to a saturation regime of direct searches, meaning that the experiment's sensitivity will no longer increase with exposure [42]. This is, of course, a problem because it would limit the reach of direct searches in terms of the dark matter-nucleus cross section.

In this chapter we will suggest a solution to this problem using technologies that not only measure the recoil energy and event time, but also the direction of the recoiling nucleus. Necessary exposures of such directional dark matter detectors in order to bypass the neutrino barrier will be estimated.

4.1 Introduction

4.1.1 Dark matter event rate

In this section we will introduce the ingredients to calculate the dark matter event rate in a direct detection experiment. We will especially address the dark matter velocity distribution that governs the annual modulation of the event rate.

The differential event rate can be expressed as [183],

$$\frac{dR_{\rm DM}}{dE_r} = M_{\rm det}\ \frac{\rho_0\sigma_0}{2m_{\rm DM}\mu_T^2}F^2(q)\int_{t_0}^{t_1}\int_{v_{\rm min}}^{\infty}\frac{f(\vec{v},t)}{v}d^3v\ dt\,, \tag{4.1}$$

where $M_{\rm det}$ is the detector mass, ρ_0 the local dark matter energ density, σ_0 the WIMP-nucleus cross section at zero momentum transfer, $\mu_T = m_{\rm DM}m_T/(m_{\rm DM} + m_T)$ the dark matter-target nucleus reduced mass, $F(q)$ the form factor, $v_{\rm min}$ the minimal velocity needed for a scattering event of recoil energy E_r and $f(\vec{v},t)$ the dark matter velocity distribution. We have $v_{\rm min} = \sqrt{2E_{\rm min}/m_{\rm DM}}$ with $E_{\rm min} = E_{\rm r}(m_{\rm DM} + m_T)^2/(4m_{\rm DM}m_T)$ as the minimal energy to obtain a recoil with energy $E_{\rm r}$. An integration over the exposure time has to be performed. We will now discuss some of these parameters and our assumptions in more detail.

For ρ_0 we assume the standard value of 0.3 GeV cm^{-3} which is in agreement with current N-body simulations [184], whereas a Bayesian analysis of astrophysical data seems to suggest a slightly larger value of around 0.39 GeV cm^{-3} [185]. Changing ρ_0 will simply scale any derived limits.

We assume that WIMPs have a Maxwellian distribution $f(\vec{v})$ with a cut-off at the halo escape velocity $v_{\rm esc} = 544$ km/s, as quoted by the Radial Velocity Project (RAVE) [186] and used as standard value throughout the literature. A new data release [187] shifted the best fit value to $v_{\rm esc} = 533^{+54}_{-41}$ km/s, such that the value used here is well within the 1-sigma range. If $|\vec{v}| < v_{\rm esc}$, the distribution in the halo

rest frame is

$$f(\vec{v})_{halo} = \frac{1}{N_{\rm esc}} \left(\frac{3}{2\pi\sigma_v^2}\right)^{3/2} \exp\left[-\frac{3\,(\vec{v})^2}{2\sigma_v^2}\right] \ , \tag{4.2}$$

with $N_{esc} = \mathrm{erf(z)} - 2\mathrm{z}\ \exp(-\mathrm{z}^2)/\sqrt{\pi}$ accounting for the truncation. We have $z = v_{\rm esc}/\bar{v}$ and $\bar{v} = 220$ km/s as the most probable WIMP velocity, which is related to the width of the distribution via $\sigma_v = \sqrt{3/2}\,\bar{v}$. For $|\vec{v}| \geq v_{\rm esc}$ we assume that $f(\vec{v})$ vanishes. It is well known that limits on the dark matter-nucleon cross section for light dark matter strongly depend on astrophysical uncertainties, see e.g. [188–191] for a non-comprehensive list, but it is beyond the scope of this analysis to include these.

The most general dark matter-nucleus cross section at zero-momentum transfer is parametrised as [192, 193]

$$\sigma_0 = \frac{4\mu_T^2}{\pi}\left(Z f_p + (A-Z) f_n\right)^2 \ , \tag{4.3}$$

where f_p and f_n are the couplings of the dark matter particle to the proton and neutron, respectively, μ_T is the dark matter-nucleus reduced mass, A the atomic number and Z the number of protons in the target nucleus. Under the assumption of an isospin conserving interaction f_p and f_n are equal such that $\sigma_0 \propto f_p^2$ holds.[1] Then, we can cast σ_0 into the dark matter-proton cross-section σ_p via $\sigma_0 = \sigma_p \left(\mu_T/\mu_p\right)^2 A^2$ and direct searches can use the event rate to constrain σ_p. This is a model independent way to constrain the interaction strength, because the model dependent quantity f_p is absorbed in σ_p. The differential event rate will then be proportional to A^2.

When the momentum transfer, q, becomes sizeable and the finite size of the nucleus and its substructure play a role, a form factor, $F(q)$, has to be introduced that describes the distribution of electroweak hypercharge within the nucleus. In our

[1] This assumption is broken in isospin-violating dark matter models that are not considered here [194].

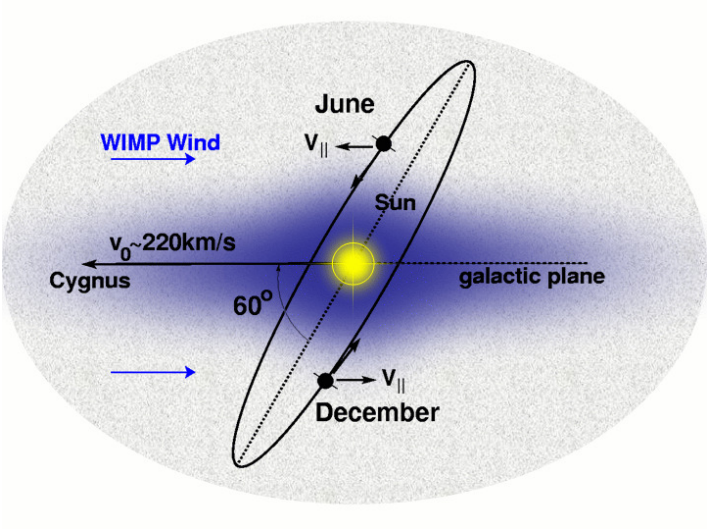

FIGURE 4.1: WIMP wind and its annual modulation due to the Earth's movement around the Sun. [196]

analysis we use the standard Helm form factors, see e.g. [183] or [195]:

$$F(qr_n) = 3[\sin(qr_n) - qr_n \cos(qr_n)]/(qr_n)^3 \cdot e^{(qs)^2/2} \ , \tag{4.4}$$

$$r_n^2 = c^2 + \frac{7}{3}\pi^2 a^2 - 5s^2 \ . \tag{4.5}$$

For the parameters we adapt the standard choices $c = 1.23A^{1/3} - 0.6\,\text{fm}$, $a = 0.52\,\text{fm}$ and $s = 0.9\,\text{fm}$ [183].

The calculation of the event rate has to be performed in the laboratory frame. Hence, we need to take into account the Earth's overall velocity vector to perform a correct transformation of frames. The Earth's velocity vector has contributions from the Sun's movement around the Galactic centre, the peculiar movement of the Sun relative to the local standard of rest and the Earth's velocity vector relative to the Sun. The dark matter velocity distribution viewed from Earth therefore has a complicated time dependence. Reference [197] describes in detail the Earth's overall velocity vector and we use it in this work.

Since the Sun moves around the Galactic centre, the isotropy of the WIMP velocity

distribution is broken in the laboratory frame. Dark matter particles moving anti-parallel to the Sun's velocity vector have, on average, a larger velocity when viewed from Earth than dark matter particles that try to "overtake" the Sun. This so-called "WIMP wind" is illustrated in figure 4.1.

On top of this, the Earth's velocity vector relative to the Sun changes throughout the year. In December it has a large component parallel to the Sun's velocity vector, in June a large anti-parallel component. Hence, the WIMP wind as seen from Earth undergoes an annual modulation with the largest WIMP velocities appearing in December.

The WIMP wind directly impacts the differential event rate because there will be more dark matter particles with a velocity larger than $v_{\min}$ in December than in June, increasing the differential event rate. This annual modulation of dark matter is a typical characteristic that any direct detection signal should ultimately possess. We now understand why we need a time integration in equation 4.1.

The total number of dark matter events is calculated by integrating the differential event rate over the recoil energy window $[E_{\text{thr}}, E_{\text{up}}]$ of the detector weighted by an energy-dependent detection efficiency $\epsilon(E_{\text{r}})$:

$$s = \int_{E_{\text{thr}}}^{E_{\text{up}}} \epsilon(E_{\text{r}}) \frac{dR_{\text{DM}}}{dE_{\text{r}}} dE_{\text{r}} \ . \tag{4.6}$$

Specification of the target material and detector exposure, the dark matter mass and cross-section translates via 4.6 into an expected event rate.

In figure 4.2 we present expected event rates s of a 100 GeV WIMP with a DM-nucleus cross section of $10^{-46}\,\text{cm}^2$ for a range of target materials depending on the chosen threshold energy. For small thresholds, heavy targets will observe more events, because the event rate scales with A^2. However, as heavier targets will in general give smaller recoil energies, the event rate drops faster when the threshold is increased. We assumed here a perfect energy efficiency and an upper threshold of 100 keV. For the rest of the analysis we will consider more realistic setups.

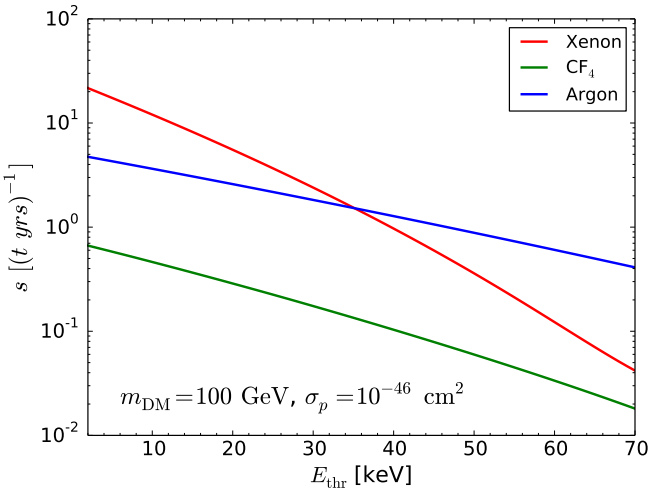

FIGURE 4.2: Dark matter event rate per ton per year for different target materials and energy thresholds but fixed dark matter mass and cross section.

We will now present the technology that is currently capable of testing the smallest DM-nucleus cross sections, two-phase noble element detectors.

4.1.2 Two phase noble element detectors

Noble elements carry many properties that are useful for dark matter direct searches. Their scintillation with fast de-excitation (order of nano seconds) after being struck by a passing particle allows for a quick detector response. Electrons that are extracted in a collision may travel freely over large distances in the dense medium as noble gases carry no electronegativity. In two phase noble element detectors, these electrons may then additionally ionise atoms in a gas phase, which is helpful to infer the position of the collision within the detector. Several experiments have been running or are proposed. A not comprehensive list is XENON100 [168], XENON1T [198] or LZ [199] as two-phase detectors and DEAP-3600 [200] as a single phase detector using liquid Argon as target material.

Currently most experiments are using Xenon as target material. The reason is the scaling behaviour of the event rate as A^2, such that smaller cross sections may be

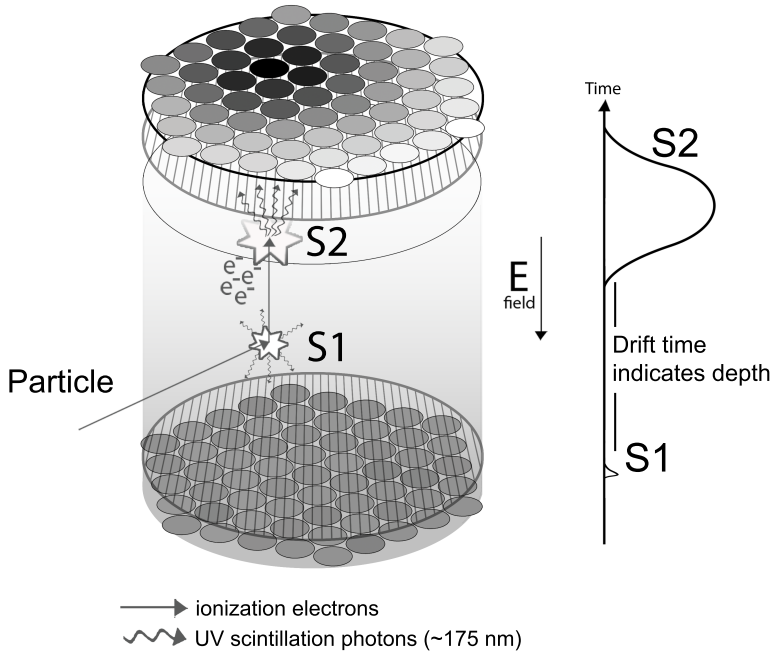

FIGURE 4.3: The LUX liquid noble gas detector, as shown in [201].

tested. For this reason, we will explain the method of a two phase noble element detector following the setup of the LUX experiment.

In figure 4.3 we show a schematic construction of the detector. The inner part is filled with the liquid noble element and, in the upper part, with its gaseous phase. The top and bottom end of the container are covered with photomultiplier tubes (PMT). If a passing particle interacts with a target atom, primary scintillation light, S_1, is released and ionisation of the atom leads to free electrons. An applied electric field accelerates these free electrons towards the gas phase, where they further ionise target atoms and more scintillation light, S_2 is produced. Both signals are recorded by the PMTs and the difference in arrival time is an indicator of the depth of the event. The position in the horizontal plane can be inferred by the distribution of signals on the PMTs. In this way, the event can be located within the detector.

This localization plays an important role in background subtraction. The detector components, even though purified and screened before construction, will always carry a trace of long-lived radioactive elements, like Uranium or Thorium. These

will undergo α and/or β decays that can contribute to nuclear recoil backgrounds. The mean free path of α particles is generally very short such that recoils from α particles will take place close to the detector surfaces. Dark matter nuclear recoils, on the other hand, will happen homogeneously within the detector volume. An efficient background rejection of α particles is therefore detector volume fiducialisation, meaning that only the innermost part is an acceptable region to look for dark matter events.

Electronic recoil events (of electrons or neutrinos) can be distinguished from nuclear recoils due to the different interaction type. In general an electronic recoil event will create less scintillation light and more free electrons, such that their $S2/S1$ ratio is larger than for nuclear recoils. Another tool to reject electronic recoils is pulse shape discrimination. This relies on the fact that the time when delayed fluorescence appears after a collision depends on the type of interacting particle. For Xenon, e.g., the effective decay constants are approximately 32 ns and 18 ns for electronic or nuclear recoil, respectively [202]. Both techniques are applied in modern detectors reaching a background rejection rate of electronic recoils of about 99.6 % [44], but it has been shown that detectors can achieve better discrimination [203].

Other technologies that are currently under development are detectors that not only measure the recoil energy and event time, but additionally the direction of the recoiling nucleus. In this chapter we will compare how these two technologies, non-directional and directional detectors, perform in the presence of the irreducible neutrino background. Before talking more about the origin and characteristic of this background, we will present the working procedure of such directional experiments in the next section.

4.1.3 Directional dark matter detectors

Directional dark matter detectors have the capability to measure additionally to recoil energy and event time the recoil direction of a target nucleus that can be used to infer the arrival direction of the incoming particle. Dark matter has an expected

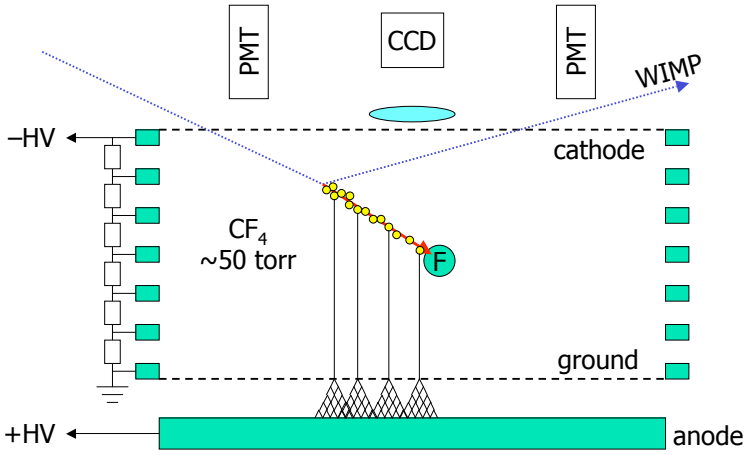

FIGURE 4.4: The dark matter time projection chamber (DMTPC) as an example for a directional dark matter experiment, as shown in [209].

daily modulation of its arrival direction due to the Earth's rotation around an axis that spans a 48° angle with the dark matter wind. This modulation forms a distinct characteristic of dark matter and an observation would strongly contribute to identify a signal as dark matter. As identifying a direction in one day is very difficult because of the count rates, it is more feasible to translate the recoil direction into galactic coordinates and measure the expected dipole feature pointing back towards Cygnus A [204, 205]. Further applications of directional experiments are to discover ring features [206], to infer parameters of the velocity distribution [207], or to distinguish different kind of interactions between DM and the SM [208].

In figure 4.4 we show as an example for a characteristic setup of a directional dark matter search the DMTPC (dark matter time projection chamber) experiment [209]. Generally, these types of experiments use a gas as target material and operate at low-pressure (around 50 Torr) such that the mean free path of a recoiling nucleus extends to a few millimetres. The DMTPC collaboration uses Tetrafluoromethane, CF_4, as target to be specifically sensitive to spin-dependent dark matter-proton interactions, but also because of its good scintillation properties that allow for easy optical readout. Electrons from ionising collisions are accelerated by an electric field towards the anode. There, an amplification region leads to an electron avalanche that is read out. The produced photons of this avalanche are

recorded by a CCD camera situated above the cathode operated at long exposure (order of seconds) such that a 2 dimensional image of the nuclear recoil is obtained. PMT's help to measure the depth of the event for background rejection and the recoil length perpendicular to that plane by recording time measurements. Finally, the recoil direction is inferred from the change in energy loss along the path of the recoiling nucleus.

The combination of track length and recoil energy serves as a background rejection tool. Dark matter particles are expected to give smaller track lengths for a given recoil energy compared to electronic recoils [210]. The typical track length is about 1 mm for a 50 keV nuclear recoil [210, 211]. Other technologies that can be used to conduct directional dark matter experiments are, e.g., arrays of carbon nanotubes [212], nuclear emulsion plates [213] or anisotropic crystals [214].

Having presented both non-directional and directional technologies, we will now take a more detailed look on the neutrino background that will penetrate any direct dark matter search and lead to scattering events.

4.1.4 Neutrino background

Ambient neutrinos are produced in the Sun, by cosmic ray collisions in the atmosphere, in supernovae, in beta decays of natural occurring elements in the Earth (geoneutrinos) and man-made neutrinos in, e.g., nuclear power stations (reactor neutrinos). All of these can potentially form a background to dark matter searches [42, 215, 216]. We will discuss each type individually.

The flux of reactor neutrinos can be kept small by ensuring that the dark matter experiment is far away from any such source and we therefore neglect this neutrino type. Geoneutrinos have energies smaller than about 4.5 MeV (most energetic neutrino from ^{238}U decay) and give events with small recoil energies that will lie below the energy thresholds of the detectors that we will consider in this analysis, compare to [215]. We are then left with three possible neutrino backgrounds: solar,

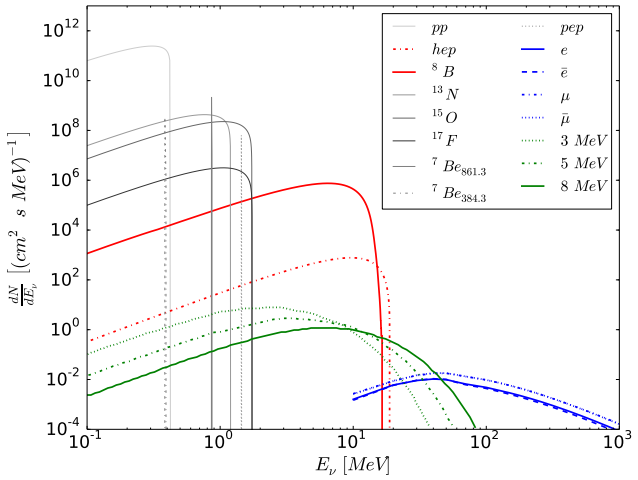

FIGURE 4.5: Neutrino fluxes considered in this work. Grey coloured fluxes will not give events above thresholds considered in this analysis. Fluxes that will act as background originate from solar neutrinos (red), atmospheric neutrinos (blue) and diffuse supernovae neutrinos (green).

atmospheric and supernovae neutrinos. In figure 4.5 we show the energy dependence of their fluxes.

Neutrinos from the Sun with energies large enough to give recoil events above thresholds are coloured in red. The largest solar neutrino flux comes from a ^{8}B beta-decay: $^{8}\mathrm{B} \rightarrow ^{8}\mathrm{Be} + e^{+} + \nu_e$. The second most important solar neutrino contribution is due to ^{3}He-proton interactions in the reaction $^{3}\mathrm{He} + \mathrm{p}^{+} \rightarrow ^{4}\mathrm{He} + \mathrm{e}^{+} + \nu_e$, the so-called *hep* neutrinos. Whereas the flux is smaller by a factor of around 10^{-4}, the neutrinos can be more energetic. As we argued for the geoneutrinos, neutrino energies below approximately 10 MeV will not give any large recoil in the detector and can thus be neglected as a background. Solar models by Bahcall et al [217] have made precise predictions on the solar neutrino fluxes that are in agreement with recent measurements of the neutrino flux at the Homestake mine [218] or by the SNO collaboration [219]. The theoretical uncertainties are around 16% on the ^{8}B and hep fluxes.

The largest neutrino energies originate from cosmic ray collision with the atmosphere, shown as blue lines in figure 4.5. Decay products of these collisions contain electron and muon (anti-)neutrinos with energies up to 1 GeV. Their flux is the smallest of all contributions. We will use results of theoretical calculations, see e.g. [220]. The atmospheric neutrino flux has recently been measured by Super-Kamiokande [221], the MINOS collaboration [222] and the IceCube collaboration [223].

The background of diffuse supernovae neutrinos is the integrated flux from all supernovae that occurred in the Universe and shown as green solid, dashed and dotted lines in figure 4.5. The neutrino energy spectrum of a single supernovae is assumed to be similar to a Fermi-Dirac spectrum with temperatures of 3 MeV for electron neutrinos, 5 MeV for electron antineutrino and 8 MeV for the other four flavors. For more details on diffuse supernovae neutrinos see for example [224].

Neutrinos may interact in two distinct ways with the target atoms in the detectors. The first possibility is neutral current elastic scattering between neutrinos and electrons. These events can have a recoil energy of a few hundred keV with a cross sections of about 10^{-44} cm^2. It has been suggested to use this process to detect solar neutrinos [225]. The second way is neutral current coherent elastic scattering of a neutrino interacting with the target nucleus. As the nuclear recoil energies are rather small (a few tens of keV) this process has not yet been observed, although their cross section is of order 10^{-39} cm^2 [226, 227]. The latter process could be used to conduct precision weak interaction measurements at the SNS [228], to search for supernova neutrinos [229] or to measure solar neutrinos [230]. Coherent neutrino-nucleus elastic scattering was already anticipated as a background before direct dark matter searches existed [231].

As we have argued earlier, electronic recoil events can be vetoed with about 99.6% accuracy. Even though their rate is much larger than nuclear recoils we will neglect them here, because future experiments are expected to increase the veto-accuracy

even more by applying stronger electric fields. In this analysis we therefore focus exclusively on coherent ν-A scattering.

We will now calculate the background rates caused by ν-A coherent scattering in target materials relevant to current dark matter searches, following approaches taken in [42, 215, 216].

The maximum recoil kinetic energy in ν-A coherent scattering is

$$E_{\mathrm{r,max}} \;=\; \frac{2E_\nu^2}{m_T + 2E_\nu} \;, \tag{4.7}$$

where E_ν is the incident neutrino energy, and m_T is the mass of the target nucleus. Because the recoil energies of these processes are quite small, the neutrino scatters off the weak charge of the entire nucleus coherently. The weak charge is given by,

$$Q_W \;=\; N - (1 - 4\sin^2\theta_W)Z \;, \tag{4.8}$$

where N and Z are the number of target neutrons and protons respectively, and θ_W is the weak mixing angle. Through the dependence on Q_W the scattering cross section scales approximately as N^2.

The differential ν-A coherent scattering cross section is given by [226, 227, 232]

$$\frac{d\sigma}{d(\cos\theta)} \;=\; \frac{G_F^2}{8\pi}\, Q_W^2\, E_\nu^2\, (1+\cos\theta)\, F^2(q) \;, \tag{4.9}$$

where G_F is the Fermi coupling constant, Q_W is the weak charge of the target nucleus, E_ν is the incoming neutrino energy, $\cos\theta$ is the scattering angle in the lab frame of the outgoing neutrino direction with respect to the incoming neutrino direction, and $F(q)$ is the nuclear form factor. Via the momentum transfer, $2m_T E_r = q^2 = 2E_\nu^2(1-\cos\theta)$, the scattering angle $\cos\theta$ is related to incoming neutrino energy and recoil energy through

$$\cos\theta = \frac{E_\nu^2 - m_T E_r}{E_\nu^2} \;. \tag{4.10}$$

We can then express the differential cross section as

$$\frac{d\sigma}{dE_{\rm r}} \;=\; \frac{G_F^2}{4\pi}\; Q_W^2\; m_T^2\; (1 - \frac{m_T E_{\rm r}}{2E_\nu^2})\; F^2(q). \tag{4.11}$$

The theoretical uncertainty on the coherent ν-A scattering cross section comes from uncertainty in the form factor; for neutrino energies of 10 MeV the uncertainty is expected to be less than 10% [229].

The differential rate of coherent neutrino-nucleus elastic scattering is

$$\frac{dR_\nu}{dE_r} = n_T \int_{t_0}^{t_1} \int_{E_\nu^{\rm min}}^{\infty} \frac{dN(t)}{dE_\nu}\; \frac{d\sigma(E_\nu, E_{\rm r})}{dE_{\rm r}}\; dE_\nu\; dt\;, \tag{4.12}$$

with n_T the number of target nuclei in the detector, the flux $\frac{dN(t)}{dE_\nu}$ and the differential cross section $\frac{d\sigma(E_\nu,E_r)}{dE_r}$. The dependence on time, t, in the flux is due to the change of distance between the Sun and the Earth over the year. We hence integrate over the exposure time of a given experiment to calculate rates. Note that the only thing that changes with time is the normalization in the solar neutrino flux, not the shape of the spectrum. As a first approximation, we take the flux of atmospheric and supernovae neutrinos to be time independent, although there is a time variation in the atmospheric flux due to temperature changes in the Earth's atmosphere [233]. This change in the event rate is, however, smaller than the annual modulation of the dark matter rate or the modulation of the solar neutrino rate. As we found that both of these are not contributing significantly to the sensitivity of the simulated directional detectors we neglect the variation of the atmospheric neutrino flux here.

In equation 4.12 the integral over the neutrino energy starts at the minimal neutrino energy E_ν necessary to get a recoil event over threshold and is given by $E_\nu^{\rm min} = \sqrt{m_T E_{\rm r}/2}$. The total neutrino event rate is then, similarly to the dark matter event rate, given by an integral over the differential recoil rate and the energy efficiency,

$$b = \int_{E_{\rm thr}}^{E_{\rm up}} \epsilon(E_{\rm r}) \frac{dR_\nu}{dE_{\rm r}} dE_{\rm r}\;. \tag{4.13}$$

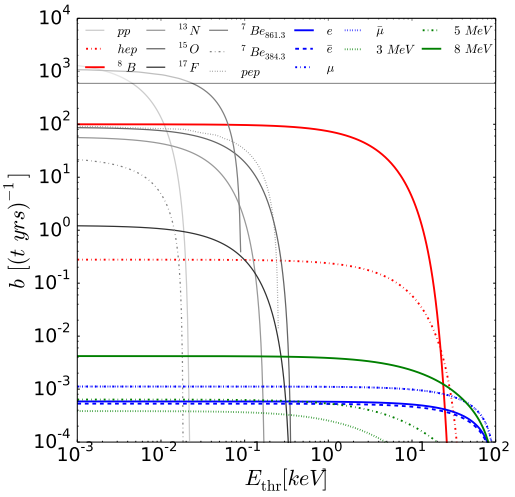

FIGURE 4.6: Neutrino event rate in a CF_4 detector. Here, a perfect energy efficiency and an upper threshold of 100 keV were assumed. For the rest of the analysis we take a more realistic energy efficiency.

In figure 4.6 we show the event rate for a CF_4 detector. For the threshold that we will consider in this work (5 keV), only ^8B and hep neutrinos from the Sun as well as all atmospheric and supernovae neutrinos are important.

4.1.5 Systematic uncertainties

The neutrino background consists of three different populations - solar, diffuse supernovae and atmospheric neutrinos. Their flux normalisations carry uncertainties and we will try here to estimate roughly by how much these uncertainties will decrease in the future.

In the energy range important for our analysis, the dominant contributions to the solar neutrino flux are ^{8}B and hep neutrinos. Both these fluxes strongly dependent on the iron abundance in the Sun which changes the opacity inside the core [234]. Currently there is a mismatch between solar compositions derived from surface observations [235] and helioseismology [236], such that the iron abundance is not well understood. The solar flux uncertainties, however, can potentially be reduced

by the SNO+ experiment, which will perform detailed measurements on the Boron-8 and Beryllium-7 neutrinos that are both sensitive to the iron abundance. This will additionally put an indirect constraint on the hep flux [237]. If Hyper-Kamiokande will be approved, it might detect hundreds of ^{8}B neutrinos per day and look for time variations in the flux [238]. With such high statistics a significant drop of the uncertainties seems possible. Data from future dark matter searches could also help to test solar models [239].

Understanding the diffuse supernova background is even more challenging, because the neutrino spectrum of a single supernovae is not well known. Using dissolved gadolinium, the sensitivity of Super-Kamiokande to detect DSNB neutrinos may be improved and a direct measurement could become possible. Then, the flux normalisation between 10 and 20 MeV could be constrained [240]. Hyper-Kamiokande has a much better perspective to measure the DSNB and could reduce uncertainties even more.

The atmospheric neutrino flux is affected by the cosmic ray flux, the geomagnetic field, nuclear propagation models as well as the solar wind. Measurements of the muon flux with balloon experiments and observing interactions of protons hitting thin targets (O_2 and N_2) at the HARP experiment can reduce theoretical errors in shower development and increase the accuracy of neutrino flux predictions by models like DPMJET-III and JAM [241]. Measuring the atmospheric neutrino flux with an upgraded Super-Kamiokande or Hyper-Kamiokande could help greatly in reducing the uncertainties.

For our analysis we make a semi-optimistic estimation that the flux uncertainties will reduce by a factor of two until the detectors that we simulate here will be built. We assume an uncertainty of 8% for the solar neutrino fluxes (note that only ^{8}B and hep neutrinos can give events above threshold in this work), and 10% for the atmospheric and supernovae neutrino fluxes.

4.2 Methodology

We have seen that both dark matter and neutrinos will give signals in dark matter direct detection experiments and calculated their event rates per ton per year. Our final goal is to estimate sensitivities of future dark matter detectors in the presence of the neutrino background. In this chapter we will present our methodology to achieve this goal and present our detector assumptions, explain the simulation of dark matter and neutrino events and describe the statistical test.

As we discussed in the previous chapter directional techniques already exist with CF_4 [211, 242] as target material which we will choose as one of the targets that we consider. Also we have mentioned that the most stringent limits currently come from Xenon based experiments, for which, on the other hand, no directional techniques have been developed or demonstrated to work. However, for comparison purposes we will nevertheless choose Xenon as the second target material, also to see the influence of directionality on heavy targets.

We will continue with discussing our detector assumptions for our simulations.

4.2.1 Detector performance assumptions

In the event rate calculation we introduced the energy efficiency, ϵ, of the detector. A reasonable parametrisation for a CF_4 detector is

$$\epsilon(E_{\rm rec}) = c_1 \left(1 + \mathrm{erf}\left[\frac{(E_{\rm rec} - c_2)}{c_3}\right]\right) \ . \tag{4.14}$$

We choose $c_1 = 0.5$, c_2 as the energy threshold $E_{\rm thr} = 5$ keV and $c_3 = 15$ keV. The 5 keV energy threshold we assume is optimistic relative to current searches, but regarding that a number of directional detectors use 5.9 keV ^{55}Fe sources for calibration and that track images with directionality at this energy have been measured in small prototypes [243], we believe it to be achievable in the future, compare to [205].

Large direct dark matter searches based on Xenon have been carried out in the past already [44, 168], so we use the efficiency curve published by the LUX experiment and shift it to a smaller energy threshold of 2 keV, because of possible technological advances. For the Xenon detectors we assume an upper energy cutoff of 40 keV, for the CF_4 detectors we take 100 keV.

No detector will be able to measure the recoil energy or the direction of the recoiling nucleus perfectly. Hence, we model the energy resolution as

$$\sigma_E = 0.1 \sqrt{E/\text{keV}} \,, \tag{4.15}$$

and the angular resolution as

$$\sigma_\theta = \frac{30^\circ}{\sqrt{E/\text{keV}}} \,. \tag{4.16}$$

There is also an efficiency connected to angular detection, which is, however, driven by energy response. Hence, as a first approximation we take the angular efficiency to be included in the energy efficiency. These values are improvements to current directional searches [244], but again we take the optimistic approach and believe them to be achievable in the future. With the fixed detector setup we are now in a position to make predictions on how dark matter and neutrino events should be observed within the directional detector based on our assumptions on the dark matter mass and its velocity distribution.

4.2.2 Dark matter signal distribution

Here we will present the expected dark matter signal distribution in terms of recoil energy and recoil direction in the detector. Our ultimate goal is to best distinguish dark matter events from the neutrino backgrounds making use of the recoil direction. We are, therefore, left with the problem to define the event direction in a useful way.

In the Introduction, we have mentioned that the dark matter arrival direction is expected to have a daily modulation due to Earth's rotation. The same, however, is true for the solar neutrino background and in the end the opening angle between solar neutrino and dark matter arrival direction will determine how well both can be distinguished. Therefore, we introduce the event angle as the angle between the direction of the recoiling nucleus and the Earth-Sun direction. In this way, solar neutrino events will have the largest possible event angles and we remove any daily modulation. We are now ready to create the expected signal distribution based on our model assumptions.

When a dark matter particle with kinetic energy E_{DM} scatters off a target nucleus with scattering angle θ with respect to its incoming direction, the resulting recoil energy is

$$E_{\mathrm{r}} = E_{\mathrm{DM}} r (1 - \cos\theta)/2 \ , \tag{4.17}$$

with $r = 4 m_{\mathrm{DM}} m_T / (m_{\mathrm{DM}} + m_T)^2$. In this work we assume isotropic scattering in $\cos\theta$, which ultimately depends on the interaction type. The scattering angle θ' of the recoiling nucleus with respect to the incoming dark matter velocity is then given by momentum conservation to be

$$\tan\theta' = \frac{p' \sin\theta}{\sqrt{2 m_{\mathrm{DM}} E_{\mathrm{DM}}} - p' \cos\theta} \ , \tag{4.18}$$

with $p' = \sqrt{2 m_{\mathrm{DM}} E_{\mathrm{DM}} - 2 m_T E_{\mathrm{r}}}$ as the dark matter momentum after the scattering event.

To simulate dark matter events we use the rest frame of the static, spherically symmetric dark matter halo and draw a random velocity magnitude v from the velocity distribution according to equation 4.2 and, to fix the dark matter direction, additionally two angles (θ,φ) in a spherically symmetric way. We then transform the dark matter velocity vector, $\vec{v}$, into galactic coordinates. We draw a random event time t from a uniform distribution between t_0 and t_1 and obtain the Earth's overall velocity vector in galactic coordinates from reference [197]. After a coordinate transformation into the rest frame of the Earth, we have the incoming WIMP

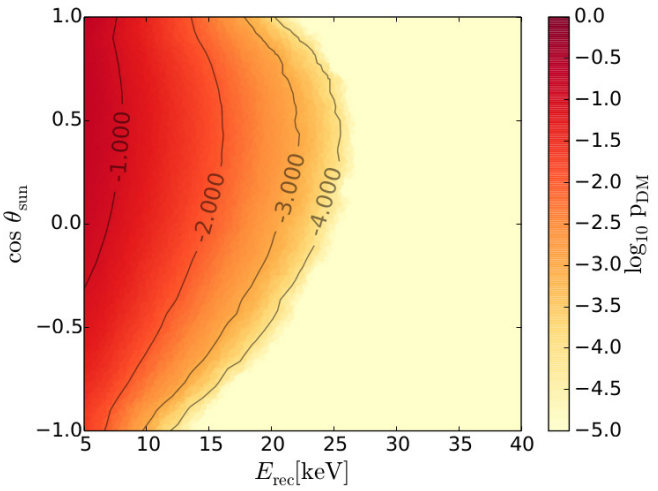

FIGURE 4.7: Two dimensional dark matter probability distribution ρ of recoil energy and event angle for a 9 GeV dark matter particle in a CF_4 detector with 5 keV energy threshold in September.

velocity vector. As we assume isotropic scattering, we draw a uniform scattering angle θ and calculate the recoil energy $E_{\rm r}$ of the event from equation 4.17. The annual modulation is thus included as those event times t for which the dark matter velocity in the laboratory frame is largest are more likely to give events above threshold and in this way more likely to contribute to the distribution.

The nucleus will recoil in a direction with angle θ' according to equation 4.18 relative to the dark matter velocity. Rotational symmetry around the incoming dark matter direction leads us to choose a random angle $\phi' \in [0, 2\pi)$ to completely fix the recoil track. We calculate the event angle $\theta_{\rm sun}$ by projecting this track of the recoiling nucleus onto the Earth-Sun direction, which at any given time is fixed, and perform the energy and angular Gaussian smearing. To take the energy efficiency into account, we only accept the corresponding fraction of events at each recoil energy and apply the energy thresholds as hard cutoffs. In this way we create ten dark matter probability distributions distributed evenly throughout the year for each dark matter mass. We simulate $6 \cdot 10^6$ events and bin the data into 60 energy and 30 angular bins.

Figure 4.7 presents the obtained two dimensional probability distribution of event

angle and recoil energy in a CF_4 detector with 5 keV energy threshold for a 9 GeV dark matter particle in September. Two distinct features should be noted. First, the event angles of dark matter scattering events preferably lie at large cos θ_{sun} (small event angles) because of the inclination of the ecliptic with the galactic disk. Second, the probability distribution drops to zero above the largest possible recoil energy for the given dark matter mass and escape velocity.

A third feature that is not directly visible in figure 4.7, but is important nonetheless, is a variation of the peak of the dark matter probability distribution in time. The direction of the Earth's overall velocity vector will point approximately towards the radio galaxy Cygnus A[2], such that the incoming dark matter particles in the lab frame will have a preferred direction coming from Cygnus A. The angle between the Earth-Sun and Earth-Cygnus A direction changes over the year, such that the peak in the dark matter probability distribution will follow a similar pattern. We will discuss this in some more detail now in the example of light dark matter.

The annual modulation in the event rate of light dark matter has a maximum in June because at this time the velocity vector of the Earth and the Sun are parallel to each other [246]. Both vectors approximately point into the direction of Cygnus A. In December, these two vectors are antiparallel resulting in a minimum of the event rate. The angle between the Earth-Sun direction and the Earth-Cygnus A direction, $\theta_{\mathrm{sun-CygnA}}$, is expected to be the same in June and December, because the Earth has simply moved to the other side of the Sun. However, in September the Earth is between the Sun and Cygnus A, such that $\theta_{\mathrm{sun-CygnA}}$ is at its largest value. The two objects appear on opposite directions in the sky. Analogously, in March when the Earth is behind the Sun relative to Cygnus, $\theta_{\mathrm{sun-CygnA}}$ is at its smallest value. These situations were studied to test the coordinate system of our simulations.

The time evolution of the peak in the two dimensional dark matter probability distribution arises because of this modulation in the relative angle between the

[2]As the direction of Cygnus A we take a right ascension of $19^{\mathrm{h}}59^{\mathrm{min}}28.4^{\mathrm{s}}$ and a declination of $40°44'1.0''$ [245]

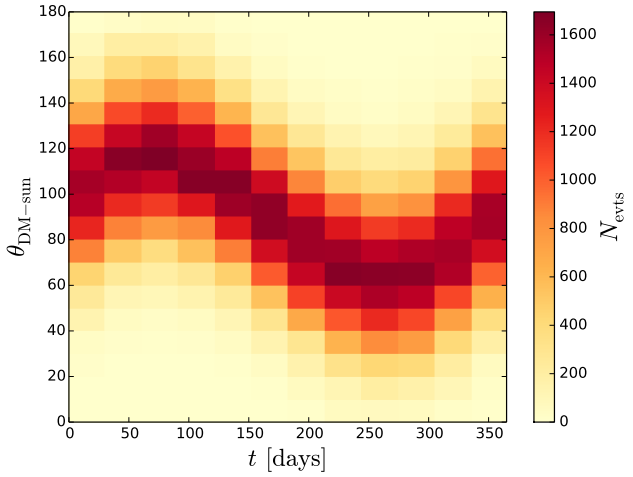

FIGURE 4.8: Distribution of the angle between the incoming dark matter velocity and the Earth-Sun direction over the year for events above a 5 keV threshold in a CF_4 detector. For each month 1×10^4 dark matter events have been simulated. The maximum of the distribution follows the expected annual pattern. Day zero corresponds to the first of January.

incoming dark matter velocity vector and the Earth-Sun direction, $\theta_{\mathrm{DM-sun}}$. Since in September the Sun and Cygnus A appear in different directions on the sky, the velocities of the incoming WIMPs that can produce an event above a detector's fixed energy threshold therefore preferentially point along the Earth-Sun direction. In March, however, the incoming dark matter velocities will point away from the Sun, resulting in a large $\theta_{\mathrm{DM-sun}}$. When simulating light dark matter events for each month of the year and producing a histogram for $\theta_{\mathrm{DM-sun}}$, we expect the peaks of these histograms to show a modulation that follows exactly this pattern. In figure 4.8 we color code the number of events in each angular bin. It is visible that the distribution in $\theta_{\mathrm{DM-sun}}$ follows the expected pattern with a maximum in March and a minimum in September.

Having presented the dark matter event rate as a function of energy, time and direction, we now turn to the neutrinos.

4.2.3 Neutrino signal distribution

The scattering angle of the nucleus with respect to the incoming neutrino direction can be found from scattering kinematics to be

$$\cos\theta' = \frac{E_\nu + m_T}{E_\nu}\sqrt{\frac{E_\mathrm{r}}{2m_T}}\,. \tag{4.19}$$

To create the two dimensional probability distribution function for neutrinos, we perform the event rate calculation, equation 4.13, for each neutrino type separately to know the exact ratio of events of each type for a given detector configuration. This is important because every neutrino type has different energies and may therefore give different recoil energies.

To simulate neutrino events, we draw a random neutrino energy according to the energy dependent flux. We use the differential cross section, equation 4.11, to create a probability distribution for each given neutrino energy E_ν to give an event of recoil energy E_r,

$$p_{\nu,E_r} = \frac{\int_{E_{thr}}^{E_r}(d\sigma/dE'_r)dE'_r}{\int_{E_{thr}}^{E_{up}}(d\sigma/dE'_r)dE'_r}\,. \tag{4.20}$$

From this we draw a random E_r and obtain the recoil angle of the nucleus via equation 4.19. For a solar neutrino the direction is known. When simulating the atmospheric and supernovae neutrinos we assume an isotropic incoming neutrino direction. Again, the outgoing nucleus has an angle θ' with respect to the incoming neutrino direction and a spherically symmetric distribution around that direction in $\phi' \in [0, 2\pi)$. We thus obtained the complete outgoing direction which we project onto the Earth-Sun direction.

These real event values are smeared according to the detector resolutions as explained in section 4.2.1 and the energy efficiency and thresholds are applied. The event time is drawn uniformly for the atmospheric and supernovae neutrinos, but from a non uniform distribution for the solar neutrinos that follows the annual

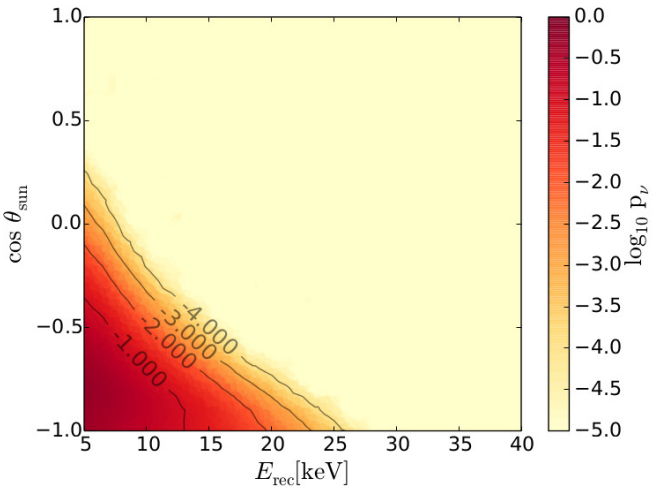

FIGURE 4.9: Two dimensional probability distribution ρ of recoil energy and event angle of neutrino events in a CF_4 detector with 5 keV threshold.

modulation of the event rate. For the neutrino probability distribution we simulate 4.5×10^6 neutrino events and bin them into 60 energy and 30 angular bins.

Figure 4.9 shows the two dimensional probability distribution of recoil energy and event angle for neutrinos in a CF_4 detector with a 5 keV energy threshold. The significant difference to the dark matter probability distribution is the clear peak at $\cos\theta_{\rm sun} = -1$ and small recoil energies due to the solar neutrino events. Atmospheric and supernovae neutrinos contribute as a smooth, isotropic background. For a 5 keV CF_4 detector we can see in figure 4.6 that the non-solar neutrinos have only a small contribution such that in this example the probability distribution function falls off steeply away from the solar peak. The ratio of the solar peak to the smooth background of non-solar neutrinos depends on the target material and the energy threshold.

The power of directionality can now be seen when the neutrino and dark matter distributions are compared. For dark matter masses that create an energy spectrum very similar to the neutrino background, both collisions can easily be distinguished when the event angle is taken into account, as dark matter and neutrinos have very

different event angles. For light dark matter a strong gain in sensitivity compared to non-directional detectors is therefore expected.

In different detector configurations the dominance of the solar peak over the non-solar background is not necessarily this significant.

4.2.4 Statistical test

Having obtained detailed spectra for dark matter and neutrino events as a function of energy, direction and time, we need a statistic to quantify how well these signal and background distributions can be distinguished in a given experiment.

The presence of backgrounds in direct searches of any kind implies that a given set of observed events is either pure background or contains background plus a hidden signal. One way to distinguish between these two cases statistically is to perform a hypothesis test. Such a test can be carried out by looking at the ratio between the probability densities of the measured data $\vec{X}$ being either signal plus background or background only, $\widetilde{Q} = \frac{\mathcal{L}(\vec{X},S+B)}{\mathcal{L}(\vec{X},B)}$ [247]. We take this as the definition of our test statistic:

$$\widetilde{Q} = \frac{p_{b+s}(n)}{p_b(n)} \frac{\prod_{j=1}^{n} \frac{sS_t(t_j)+bB_t(t_j)}{s+b} \; \frac{sS^{(t)}_{\theta,E}(\theta_j,E_j)+bB_{\theta,E}(\theta_j,E_j)}{s+b}}{\prod_{j=1}^{n} B_t(t_j) \; B_{\theta,E}(\theta_j,E_j)} \; . \tag{4.21}$$

Here s is the number of expected dark matter events given by equation 4.6, b the number of expected neutrino events given by equation 4.13 and n the total number of observed events in an experiment. $p_\lambda(n)$ is the Poisson distribution centred at λ, where λ is either b or $b+s$. The functions with capital letters B or S denote different normalised probability distribution functions for the neutrino and dark matter events, respectively. The variables t_j, E_j, θ_j denote the time, recoil energy and event angle of the j-th event. B_t and S_t describes the annual modulation of the neutrino and dark matter event rate, respectively.

$S^{(t)}_{\theta,E}$ is the two dimensional probability distribution of the recoil energy and the event angle for dark matter events and $B_{\theta,E}$ the corresponding one for neutrino

events. Visualized examples of these distributions are the figures 4.7 and 4.9, respectively. The dark matter distribution carries an additional index for time because of the variation of its peak over the year as described in section 4.2.2. To include this time variation, we choose ten equally distributed days over one year and create one probability distribution function for each of these days. A given event will then interpolate linearly between the two probability distribution functions closest to the signal event time.

We can further simplify equation 4.21 to:

$$\widetilde{Q} = e^{-s} \left(\frac{b}{s+b} \right)^n \prod_{j=1}^{n} \left(1 + \frac{sS_t(t_j)}{bB_t(t_j)} \right) \left(1 + \frac{sS^{(t)}_{\theta,E}(\theta_j, E_j)}{bB_{\theta,E}(\theta_j, E_j)} \right) \ . \tag{4.22}$$

In the following we will discuss the log-ratio $Q = -2 \log \widetilde{Q}$.

For every dark matter mass and cross section we want to find out whether a fixed detector setup (target material, energy threshold, exposure, energy and angular resolution) is capable of distinguishing whether the observed events are pure background or contain a dark matter signal. To do so, Q has to be evaluated twice: First we simulate pseudo-experiments with only neutrino events and obtain a distribution $p_B(Q_B)$ for the background only hypothesis using equation 4.22. As, in this case, the pseudo-data is more consistent with the background expectations, $p_B(Q_B)$ will peak at positive Q values. We then repeat the exercise and simulate pseudo-experiments with dark matter and neutrino events to get a distribution $p_{SB}(Q_{SB})$, again with equation 4.22. This distribution will, in contrast, peak at negative Q values. Note that for both evaluations the dark matter mass and cross section is fixed, such that s is the same for both cases, even if the background only hypothesis is simulated.

To account for the flux uncertainties we vary the expectation of each pseudo experiment, that is b in equation 4.22. Hence, for each pseudo experiment we draw a

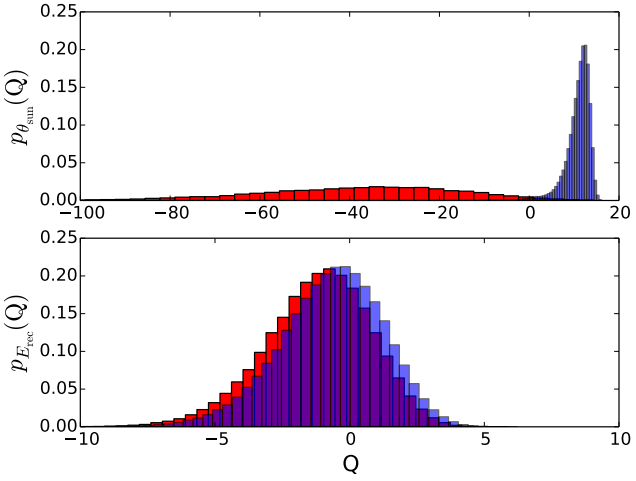

FIGURE 4.10: Normalised background only distribution $p_B(Q_B)$ (blue) and signal plus background distribution $p_{SB}(Q_{SB})$ (red) including angular information (top) and excluding angular information (bottom) for s=10 and b=500 for a 6 GeV dark matter particle in a CF_4 detector. The gain in sensitivity when using directionality is clearly visible in the separation of the two distribution in the upper plot.

random flux value for each neutrino flux type from a Gaussian with 1σ corresponding to the uncertainties. This results in a different expected background rate b for each pseudo-experiment and widens the Q distributions.

The number of observed events n in a pseudo experiment is drawn from a Poisson distribution centred at a value λ which is either equal to b_0 for the background only or $b_0 + s$ for the signal plus background simulation. Here b_0 is the background rate assuming the incoming fluxes have their nominal measured value such that we obtain a central value result. We can then repeat the procedure shifting b_0 up and down by one sigma to obtain a 1 sigma band for estimated exclusion limits. For each pseudo experiment we simulate these n events as discussed in section 4.2. To decide how many of the n events are dark matter or neutrino events, we draw for each event a random number r. If r is greater than $s/(s+b)$ this event will be simulated as a neutrino, otherwise as dark matter.

This procedure allows us to decide whether the detector setup is sensitive to that

chosen m_{DM} and σ_{p}, if we look at the separation between the two obtained distributions Q_B and Q_{SB}. The clearer this separation, the easier it is for the chosen detector configuration to distinguish between the two hypotheses and the more sensitive the detector. The lower the signal rate and the more similar the signal expectations are to the background expectations, the closer the distributions will be until they start to overlap. If the overlap becomes too large, the experiment will lose its sensitivity completely. See figure 4.10 for a visualization.

To quantify the sensitivity of a given dark matter experiment for a specific dark matter mass and cross section we calculate the overlap of these two distributions as follows. We integrate both,

$$\beta_{SB} = \int_{-\infty}^{q} p_{SB}(Q_{SB})\ dQ_{SB}\ , \tag{4.23}$$

$$\beta_{B} = \int_{-\infty}^{q} p_{B}(Q_{B})\ dQ_{B}\ , \tag{4.24}$$

up to a q value for which

$$1 - \beta_{SB} = \beta_B \equiv \alpha\ . \tag{4.25}$$

We take the confidence level at which the signal plus background hypothesis can be distinguished from the background-only hypothesis to be $(1-\alpha)$. In this work we are interested in separations of both hypotheses at 90% confidence level, corresponding to α equal to 0.1, and in 3σ separations ($\alpha = 0.00135$).

An advantage of this procedure is that experimental uncertainties can easily be incorporated by smearing the probability distributions. Dark matter searches have imperfect energy and angular resolution leading to a smearing of $B_{\theta,E}$ and $S^{(t)}_{\theta,E}$. The background of non-solar neutrinos ensures a non-zero value for $B_{\theta,E}$ for all values of θ and E such that Q is well behaved.

The statistical approach has uncertainties due to a finite sample size of pseudo-experiments, a finite number of events to create the two-dimensional probability distributions, as well as a finite bin width when creating the histograms of the test

statistics. We estimate this numerical error to be 5% in the overlap and add it to the error due to the systematic uncertainties.

This completes the discussion of the methodology. We are now in a position to first show the arising of the neutrino bound in non-directional searches, then compare exclusion limits for a given detector setup and at last investigate the scaling behaviour of these exclusion limits with detector exposure.

4.3 Results

After presenting our methodology, we will now show the results of our analysis. We begin by explaining how a saturation regime arises in non-directional searches. Then we compare exclusion limits obtained with and without directional information for an otherwise fixed detector setup and, at the end, investigate their scaling behaviour with detector exposure. In the following discussion we will focus on the CF_4 detector as an example and make a comparison to a heavier target material when we discuss the scaling behaviour. We will comment on the dependence on angular and energy resolution as well as the impact of the annual modulation.

4.3.1 The bound in non-directional searches

To show how the neutrino bound appears, we chose a non-directional CF_4 detector according to our assumptions in section 4.2.1 and scale up the exposure such that background rates from 5 to $5{\cdot}10^3$ are expected. For each dark matter mass we then find the cross section that separates signal plus background hypothesis from the background only hypothesis at 90% confidence level. The results of the scan are presented in figure 4.11.

One can observe that the experiment's reach at low dark matter masses scales much worse than at masses above around 20 GeV. The reason for this is that the energy spectra of a 9 GeV dark matter particle and the ^{8}B neutrinos are identical in CF_4.

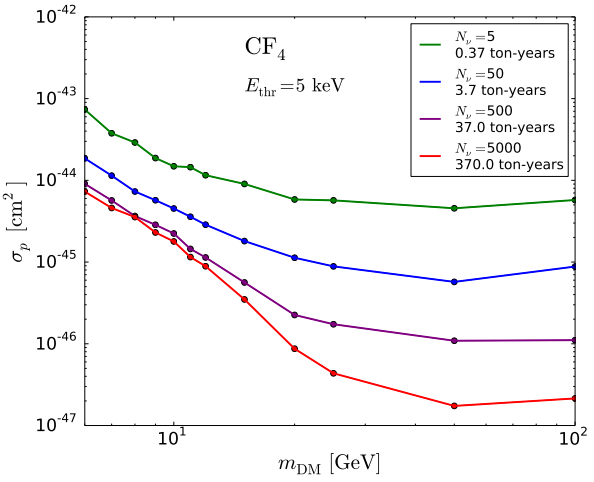

FIGURE 4.11: Estimated exclusion limits of a CF_4 non-directional detector for different number of neutrino events. A saturation regime at low dark matter masses appears.

Hence, around this mass region there is no information to be gained from measuring the energies of the collisions and the only possibility to distinguish dark matter from neutrinos is the counting of events. In a pure Poisson dominated regime, the discovery limit would evolve proportional to $\sqrt{N}/N$ according to the statistical uncertainties. Here, we need to add the systematics which are proportional to the background rate, we call the proportionality factor α. In total we then have:

$$\sigma \propto \frac{\sqrt{N + \alpha^2 N^2}}{N} = \sqrt{\frac{1 + \alpha^2 N}{N}}\,. \tag{4.26}$$

For $\alpha^2 N \gg 1$, we have $\sigma \propto \alpha$ and the discovery limit becomes constant at a value set by the systematics. This is the discovery limit of non-directional direct searches, which was presented in this form in [42]. Note that specific assumptions on the dark matter velocity distribution were made which is not known either. Including the uncertainty on the dark matter velocity distribution will widen the neutrino floor, as discussed in reference [248].

We discussed here the origin of the solar neutrino discovery limit. Heavy dark matter particles have an energy spectrum sufficiently different to solar neutrinos

such that their occurrence only has a small influence on the scaling behaviour for heavy WIMPs. In fact, one could imagine a situation in which the energy threshold of the detector is so large that all solar neutrinos are cut, such that the experiment is effectively background-free. For large exposures, however, the non-solar neutrinos will be observed and a similar argument can be given. Again, there will be a saturation regime which limits future searches, however at much smaller cross sections. Because the exposures needed to reach this limit are so large (about 10^3 ton-years [42, 249]) we will focus on the solar neutrino background in this analysis.

Note here that the discovery limit is slightly target material dependent. For a Xenon detector, e.g., the energy spectra of ^{8}B neutrinos is identical with a 6 GeV WIMP instead and the discovery limit would shift to the left. Also, the discovery limit only strictly exists for a perfect match of the energy spectra of dark matter and neutrino. If the dark matter particles can give a slightly larger recoil energy than the neutrinos, a few of these higher energetic events could clearly tell apart signal from background. The probability for such an event to occur is, however, quite small such that in the mass region close to the strict discovery limit the scaling behaviour is still strongly affected by the background contamination. Also the energy resolution of a detector will make such a distinction difficult.

A more recent analysis with a finer energy grid than the one used here showed that differences in the tail of neutrino and dark matter energy spectrum may be used to overcome the saturation regime, but very large background rates of $\approx 10^4$ need to be present for this effect to be measurable [249]. Because these large exposures are very difficult to achieve, other ways to go beyond the bound should be examined. In the next section, we will prove that one such possibility is the use of directional information.

4.3.2 Estimation of detector sensitivities

We have seen that the neutrino background limits the reach of non-directional searches. Here we will fix the detector set-up and then compare directly the sensitivities of searches with and without directional information. We will look at sensitivity limits at the 90% confidence level and 3σ level. The detector exposure is scaled such that each simulated experiment will observe 500 neutrino events, i.e. the background contribution is sizeable. Again we use CF_4 as target material and choose the detector setup as discussed in section 4.2.1.

Figure 4.12 shows the obtained sensitivity bands for a 36.6 ton-year CF_4 experiment with a 5 keV energy threshold. The 500 neutrino events consist of 499.8 expected solar and 0.2 expected non-solar neutrinos. The red (green) band represents limits that can be obtained with a non-directional (directional) detector at a 3σ level. The fainter colours show corresponding limits at 90% C.L, the grey curve is the discovery limit derived in reference [42]. The separation of the green band from the red band represents the impact of directional information.

The non-directional detector cannot test the parameter space beyond the neutrino background at 90% confidence level. However, we see that cross sections below the solar neutrino bound can be probed at the 3σ level when directional information is taken into account.

Directional information is more useful the smaller the dark matter mass as can be seen by the increasing separation of the lines when moving from heavy to light dark matter. This can be understood by the significant separation of the neutrino and dark matter peak in the combined two dimensional probability distribution function. For a light dark matter event to be above threshold, the track of the recoiling nucleus has to lie closer along the incoming dark matter direction in order to produce a large enough recoil energy. Hence, the dark matter signal also has a strong directional character. As the event angle for neutrinos has a distribution pointing back to the Sun, directional information impacts the sensitivity significantly.

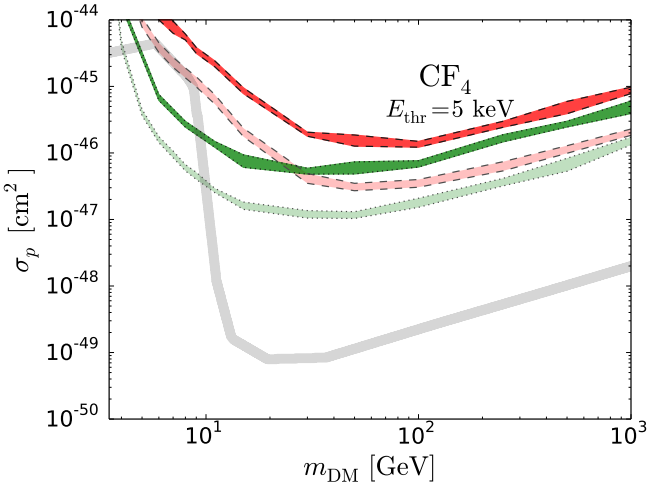

FIGURE 4.12: Estimated sensitivity limits at 3σ level for a non-directional (red band) and directional (green band) CF_4 detector with 36 t-yrs exposure and 5 keV energy threshold resulting in 500 expected neutrino events. The fainter bands indicate corresponding sensitivity limits at 90% CL, the grey curve is the neutrino bound.

Towards heavier dark matter masses, we see that the sensitivity curves approach each other and directionality plays a subdominant role. For heavy dark matter, the distinction of signal and solar neutrino background is already easy when the energy spectrum is considered on its own, because the recoil energies of solar neutrinos are much smaller compared to heavy dark matter. Besides, the dark matter events lose their clear directional character. The kinetic energy of heavy dark matter particles is, in contrast to light dark matter, also large for smaller dark matter velocities. Hence, the incoming dark matter direction becomes less constrained and more isotropic the heavier the WIMP. Directionality still adds to the sensitivity, because heavy dark matter particles may give recoil events with energies that fall into the solar neutrino region. In that case, only the direction can tell the two apart. Hence, also for heavy dark matter, an increase in sensitivity is found. Note that track resolution improves for larger recoil energies and thus for heavier dark matter the recoil track is less smeared and has a better defined direction.

In this section we have presented results from detector simulations for which we fixed the number of expected neutrino events to 500 in order to estimate possible

sensitivity limits in the presence of neutrino backgrounds. It was shown that cross sections beyond the discovery limit can be probed when directional information is taken into account. Directional detectors have significantly larger sensitivities for light dark matter masses and adds to the sensitivity for heavy dark matter. We will now move on and discuss how these limits behave as a function of exposure.

4.3.3 Projected sensitivities

In the previous section we have seen that directionality can increase the sensitivity of direct searches significantly. Now we will investigate the scaling behaviour of this sensitivity to find out which exposure is necessary to cross the neutrino discovery limit. For dark matter masses we choose 9 GeV to see how directionality helps when the energy spectrum of solar ^8B neutrinos and dark matter are identical, 1000 GeV as a heavy dark matter mass and 30 GeV as an intermediate. For each dark matter mass and cross section we simulate $15 \cdot 10^3$ pseudo-experiments.

Again, we look at a CF_4 detector and present the results in figure 4.13. The projected sensitivity limits for directional detectors are presented as solid, for non-directional detectors as dashed-dotted lines in dependence on the dark matter mass. We colour code the three different masses in blue (9 GeV), red (30 GeV) and black (1000 GeV). The discovery limits for each dark matter mass of [42] are indicated as horizontal dashed lines, which were derived for Xenon as target material. To compensate for the dependence on target material that we discussed in section 4.3.1, we show the limit of a 6 GeV WIMP derived for Xenon here for the 9 GeV WIMP in CF_4. This should be a reasonable choice because the energy spectra are the important factors for the discovery limit. We expect the projected non-directional sensitivity limits to flatten out below the limits from reference [42] by a factor of 2 because we assume half their neutrino flux uncertainties.

We will first discuss the scaling behaviour for a 9 GeV WIMP. Looking at the non-directional limit, we observe that it flattens out just below the discovery limit as we expect because of the different assumptions on the neutrino flux uncertainties. The

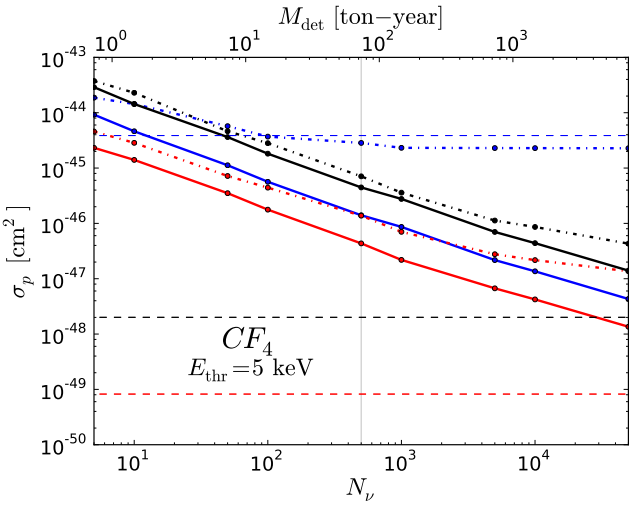

FIGURE 4.13: Estimated sensitivity limits for a directional CF_4 detector with a 5 keV energy threshold for a 9 GeV (blue), 30 GeV (red) and 1000 GeV (black) dark matter particle. The solid lines show directional detectors, the dash-dotted lines show non-directional detectors. The horizontal dashed lines indicate the discovery limit of [42] for each dark matter mass. The vertical grey line indicates a background rate of 500 events.

directional detector will test cross sections beyond the discovery limits even with imperfect flux knowledge and we estimate the necessary exposure to be around 2 ton-years. The slope of the directional sensitivity line is constant, such that no discovery limit exists once directional information is used. Also for the heavier dark matter masses we see that directionality contributes significantly and can help more than an order of magnitude in the cross section for the intermediate mass. The heavier the dark matter mass, the less significant is the impact of the direction, as we explained in the previous section. However, we can also see that the discovery limits for the heavier WIMP masses may only be reached for an unreasonably large exposure (more than 10^4 ton-years). We note again that directional detectors operate with low-pressure gas such that very large exposures quickly lead to very large detector volumes.

At the moment, the strongest constraints on the WIMP-nucleon cross section are set by experiments that use Xenon as a target material. It is not clear how a Xenon detector might be made directional, however, it is still interesting to ask which cross

section experiments with heavy target materials would be able to probe if they used directional information. There has been recent interest in developing a direction-sensitive Xenon detector technology based on recombination dependence on the recoil angle relative to the detector $\vec{E}$ field [250]. This may perhaps be a possibility for the future.

An additional motivation to pursue directionality is that ultimately very large Xenon detectors would be limited by the background of solar neutrino-electron elastic scattering events. It is important to note that we do not take this background source into account in our simulations, although it is expected to become significant at the 10^{-48} cm^2 level [251]. Additionally, the electron discrimination in Xenon detectors is less efficient than in other detectors, for example liquid argon. Directionality could aid in that discrimination considerably, because these events have a direction that points back to the Sun, allowing deeper cross sections to be probed. Hence, directional detectors could also be used to detect neutrino-electron recoil events, and one could ask whether CNO neutrinos could be measured. However, the electronic recoil spectrum in the energy window of these detectors (below 100 keV) is dominated by solar pp-neutrinos with an event rate that is about 100 times larger than the CNO neutrino event rate, see e.g. [252]. Keeping in mind that their recoil spectra at these recoil energies are very similar, namely rather flat, [42, 225], detecting CNO neutrinos is very challenging. Of course it is important to note that such large detectors would cost a great deal of money since Xenon is ∼\$1000 per kg at today's prices and only 25 tons are obtained from the air annually. It would be interesting to investigate in more detail how directionality could help to further reduce this background.

We look at a hypothetical directional Xenon detector in figure 4.14. As expected, for $m_{\rm DM} = 6$ GeV the sensitivity of non-directional Xenon detector flattens out just below the discovery limit. Again it is important to observe the strong increase in sensitivity for light dark matter once directional information is used. This is shown by the large gap between the dotted and solid blue lines. The necessary exposure to go beyond the neutrino bound is about 10 ton-years. For larger dark matter masses

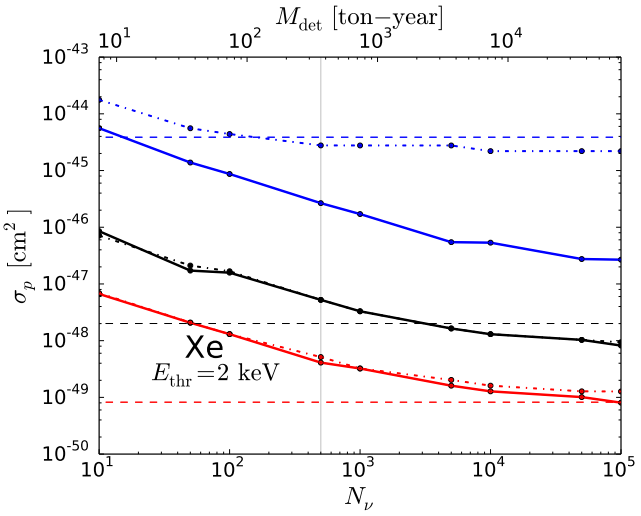

FIGURE 4.14: Estimated sensitivity limits for a directional Xenon detector with a 2 keV energy threshold for a 6 GeV (blue), 30 GeV (red) and 1000 GeV (black) dark matter particle. The solid lines show directional detectors, the dash-dotted lines show non-directional detectors. The horizontal dashed lines indicate the discovery limit of [42] for each dark matter mass. The vertical grey line indicates a background rate of 500 events.

one can observe that directional and non-directional limits are close to identical for the heavier target. For Xenon the possible recoil energies of solar neutrinos are, taking our chosen threshold energy into account, between 2 and 5 keV. This is only a small range compared to the total considered energy window of the detector (2 to 40 keV). Hence, the region where only the direction can tell apart a neutrino from a dark matter particle is rather small and for large dark matter masses recoil energy alone is sufficient. The projected sensitivities reach a boundary close to the discovery limit. The boundary of the 1000 GeV WIMP candidate is slightly below the discovery limit as expected from the reduced flux uncertainties. We note that the discovery limits in [42] were obtained with a 4 keV energy threshold, compared to a 2 keV threshold here. This explains why the 30 GeV sensitivity line stays just above the neutrino bound. The number and type of neutrinos present in the detector show a strong dependence on the chosen energy threshold in this dark matter mass region.

We find that the sensitivities for directional and non-directional detectors are close

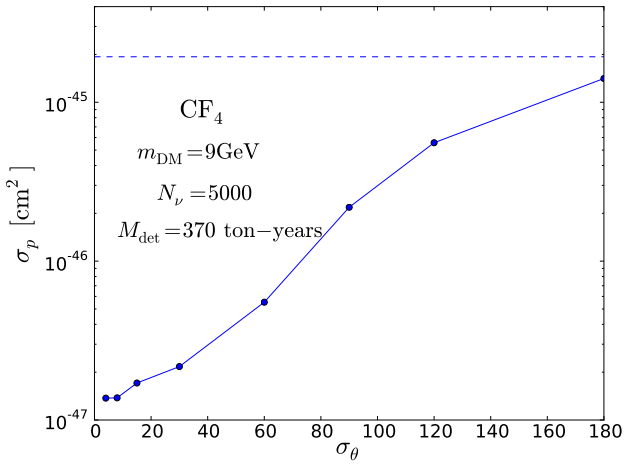

FIGURE 4.15: Dependence of sensitivity on angular resolution for fixed exposure and dark matter mass. The blue dashed line indicates the discovery limit.

to identical for heavy dark matter and a distinction between atmospheric neutrino and dark matter recoils is not possible for our chosen exposure, energy threshold as well as energy and angular resolution. In [253] it was shown that with a lower energy threshold and better energy and angular resolutions the atmospheric neutrino bound can be surpassed, but only for exposures of around 10^4 ton-years.

In figures 4.14 and 4.13 the improvement in sensitivity is visible when directional information is included additionally to event time and recoil energy. In our analysis we find that time information adds only little to the sensitivity of a pure spectral analysis. For a 9 GeV dark matter particle in a CF_4 detector, e.g., we can find an improving effect of 10% on the sensitivity when measuring annual modulation only if there are about 10^3 background events. We see that annual modulation becomes important for large background rates and that the impact of directional information is much larger.

Reference [248] presents the different modulation phases of neutrino and dark matter signals and then estimates detector exposures necessary to go beyond the neutrino floor if only annual modulation is considered on top of event counting and recoil energies. It is shown that it is possible to circumvent the neutrino floor, however, with the same conclusion that large event rates are crucial. To show the

effect a 10 ton Xenon detector with 0.1 keV threshold was chosen, which will give about 10^4 events per year. A clear increase in sensitivity is observed for exposures above 96 days which corresponds to about 10^3 events and is in agreement with our results.

The estimated sensitivities of directional detectors also depend on the chosen angular and energy resolutions. We find the angular resolution to be the more important one. In figure 4.15 we show the maximal testable cross section of a CF_4 detector for a 9 GeV dark matter candidate and an exposure of 5000 background events. It is visible that the sensitivity varies over two orders of magnitude and approaches the discovery limit if the angular resolution vanishes.

In this section we have proved that, in principle, there is no solar discovery limit for directional direct dark matter searches. Going beyond the discovery limit for a 9 GeV dark matter particle is possible for an exposure of approximately 2 ton-years for a directional CF_4 and around 10 ton-years for a directional Xenon detector. For this dark matter mass, a directional experiment can reach the discovery limit with an exposure which is smaller by about an order of magnitude compared to the non-directional case. Directionality has more impact the lighter the dark matter particle is. For events to be above the energy threshold, the incoming light dark matter particles need a large velocity and, hence, have a clear arrival direction from Cygnus A, clearly distinct from the arrival direction of neutrinos. For a light target material directional information also adds to the sensitivity of heavy dark matter candidates.

4.4 Conclusions

Coherent neutrino-nucleus elastic scattering will become an irreducible background for future generations of direct dark matter experiments. The scaling of sensitivity with exposure will greatly suffer and a neutrino bound arises. We investigated how directional information can help additionally to time and recoil information to

distinguish dark matter signal from neutrino background. To do so, we performed a hypotheses test and demanded separations of the two hypotheses at 90% confidence or three sigma level.

For the simulated detectors we assumed moderately optimistic energy thresholds and energy efficiencies as well as smearing due to imperfect energy and angular resolution. In order to see how the target mass influences the searches, we looked at Tetrafluoromethane, CF_4, as a light and Xenon as a heavy target material. For CF_4 there are detector technologies that measure the recoil track of the nucleus, whereas they have not yet been developed for Xenon.

In section 4.2 we calculated two dimensional probability distributions in recoil energy and event angle, θ_{sun}, of neutrino and dark matter events. In figure 4.7 we showed the distribution of light dark matter and pointed out that it peaks at large values of $\cos\theta_{\text{sun}}$. We presented how the position of this peak evolves over the year due to the motion of the Earth around the Sun in figure 4.8. We remarked that the lightest dark matter particles that a detector is sensitive to, need to have a large incoming velocity such that their arrival direction points back to Cygnus A.

In the same section we presented in figure 4.9 the corresponding distribution of the neutrino events. The way we defined the event angle removes any time dependence of this distribution. Compared to dark matter, we noted that the solar neutrinos peak at small recoil energies and at $\cos\theta_{\text{sun}} \approx -1$. The non-solar neutrinos were assumed to have an isotropic distribution in the detector frame and act as a smooth background for the distribution.

In section 4.3.2 we simulated a CF_4 detector and fixed the exposure such that there are 500 expected neutrino events. We found that with directional information cross sections beyond the neutrino discovery limit may be probed. The directional detectors can test more than an order of magnitude smaller cross sections compared to non-directional detectors for light dark matter masses.

We projected possible sensitivities as a function of exposure in section 4.3.3. We saw that directional information removes the solar neutrino discovery limits and is especially useful for light dark matter. For a 9 GeV dark matter particle an exposure of approximately 2 ton-years for a directional CF_4 and around 10 ton-years for a directional Xenon detector is needed to go beyond the discovery limit of non-directional detectors. The limit is reached with an exposure that is about an order of magnitude smaller compared to the non-directional case.

Chapter 5

Conclusions

The evidence for dark matter is overwhelming. We have outlined in the introduction that the dynamics of galaxies and clusters of galaxies suggest that there must be more gravitating mass than simply the visible matter. Measurements from Big Bang nucleosynthesis and from the Cosmic Microwave Background have confirmed that a great part of the matter in the Universe is not only dark, but also non-baryonic.

One popular framework for this new kind of matter is the weakly interacting massive particle (WIMP) that can provide the correct relic abundance via a freeze-out process in the early Universe. Its weak interactions have initiated a series of experiments that try to identify the exact particle properties. A dark matter particle may be produced at particle accelerators, may collide with ordinary atoms in terrestrial experiments or it may annihilate in dark matter rich regions such that the annihilation products can be detected.

Up to this point no conclusive signal has been observed by any experiment. Whereas one typical collider signal of dark matter would be a mono-jet event with large missing energy, it may be that the first hint of dark matter is of a more indirect kind. Excesses in other searches could lead the way to pin down the dark matter properties.

As an example, we discussed in Chapter 2 how a deviation in a dilepton search by CMS can be interpreted within the Minimal Supersymmetric Standard Model (MSSM) that contains a popular dark matter candidate, the lightest neutralino. We suggested simplified supersymmetric models in which the second lightest neutralino, $\tilde{\chi}_2^0$, either decays via an on-shell slepton or an off-shell Z to a final state with two leptons. Strong production of sbottoms that subsequently decay into $\tilde{\chi}_2^0$ boosts the production of dilepton pairs. To test the validity of these models, we recast a comprehensive list of complementary searches using the automation tool `Atom`.

We found that on-shell slepton scenarios are disfavoured by an ATLAS stop search such that the only possible way to explain the excess within the MSSM are the off-shell Z scenarios. A fit within the 1σ uncertainty around the best fit value can be achieved in a scenario with right-handed sbottoms and higgsino-like $\tilde{\chi}_2^0$ that weigh around 280(330) GeV and 230(240) GeV, respectively. For left-handed sbottoms a fit to the central value can be obtained for 370 GeV sbottoms and 240 GeV, wino-like $\tilde{\chi}_2^0$, but the correct dark matter relic abundance cannot be accounted for. Tensions between these two explanations and other searches already exist, such that the next run of the LHC will clarify the situation in this channel, especially given that a similar ATLAS search did not show any deviation.

The recasting of existing limits that we performed in Chapter 2 is essential for obtaining solid statements about the validity of a given SUSY model, because production cross sections and decay modes in the MSSM are highly model dependent. Developing such an automated machinery further is an important goal to interpret future SUSY searches.

A tremendous success of the LHC was the measurement of the Higgs mass at 125 GeV. It not only completed the Standard Model, but also created opportunities to look for new physics, e.g. through deviations in its production or decay rates. Interestingly, an enhancement in the Higgs to diphoton decay rate was initially observed by both independent experiments, ATLAS and CMS. Although this excess

has now vanished, we investigated in Chapter 3 what could be learned from such an anomaly using the example of vector-like leptons.

We explained how the Higgs to diphoton decay is altered by the new fermions and that a dark matter candidate is present in the model. Even though strong constraints from dark matter and collider searches as well as electroweak precision tests were taken into account, we have shown that the correct dark matter relic abundance can be provided. We further proposed and examined a possible relation to the formation of the baryon asymmetry of the Universe, which cannot be generated within the Standard Model with the Higgs mass at 125 GeV. The new fermions can alter the strength of the electroweak phase transition sufficiently to ensure strong enough deviations from thermal equilibrium for successful electroweak baryogenesis. Simultaneously, the dark matter candidate stays valid and the diphoton rate stays slightly enhanced offering the possibility to test this scenario at future colliders. We also argued that the new fermions intensify the problem of vacuum (in)stability and indicated that a solution would be to add additional bosonic degrees of freedom to the theory.

While the search for signals at the LHC goes into the next round, the wait for a dark matter signal at direct detection experiments continues. These searches constrain the WIMP-nucleon scattering cross section by looking for dark matter collisions in low background, terrestrial experiments.

From the dark matter model building perspective, however, it is not uncommon that this cross section is suppressed. Mixing in the dark sector or destructive interference between multiple contributions may decrease the cross section far below currently tested values.

There will then be the need to scale up these detectors and an irreducible background from coherent neutrino-nucleus elastic scattering will begin to introduce contaminations. Ultimately, this results in a saturation regime, the so-called "neutrino bound". Ways to overcome this limit must be developed and we proposed one idea in Chapter 4.

To surpass the neutrino bound, we suggested using the direction of the recoiling nucleus as additional information, which can be measured in directional dark matter experiments. As most of the background neutrinos will arrive from the Sun, neutrino and dark matter collisions will in general lead to different recoil directions of the atomic nucleus. We derived two dimensional probability distributions of recoil energy and event angle for neutrino and dark matter scattering events and proved that they are a powerful tool to distinguish signal from background. A hypothesis test was performed to quantify the sensitivity of a given experiment.

We analysed the scaling behaviour of directional and non-directional searches in the presence of the neutrino background and showed that the saturation regime can be overcome with directional information. With Tetrafluoromethane as target material the necessary exposure is 2 ton-years at a WIMP mass of 9 GeV. For a hypothetical directional Xenon detector we find a necessary exposure of around 10 ton-years for a 6 GeV WIMP.

In this thesis we investigated how excesses at colliders can be interpreted in dark matter models and suggested relations to other problems of the Standard Model, such as baryogenesis. One solution to the future challenge to direct searches of neutrino backgrounds has been proposed using directional information of recoil events. We hope that this thesis contributes to the quest for dark matter that continues on many fronts and will face challenges in the future.

Appendix A

Validation tables

Here we show the validation results of our implementation of the CMS dilepton search [78, 79] and the ATLAS stop search with two lepton final state [116].

$(m_{\tilde{b}}, m_{\tilde{\chi}_2^0}) = (400, 150)$ GeV	Central	`Atom`/Exp	Forward	`Atom`/Exp
$N_{\text{jets}} \geq 2$(no $\not{E}_T$ cond.)	242.7 ± 2.8	1.04	34.2 ± 1.1	0.77
$N_{\text{jets}} \geq 3$(no $\not{E}_T$ cond.)	186.2 ± 2.5	1.09	25.6 ± 0.9	0.76
$\not{E}_T > 100$ GeV(no N_{jets} cond.)	152.5 ± 2.1	1.03	19.8 ± 0.8	0.98
$\not{E}_T > 150$ GeV(no N_{jets} cond.)	85.0 ± 1.5	0.93	10.4 ± 0.5	0.87
Signal region	132.4 ± 2.0	1.031	17.0 ± 0.7	0.937

TABLE A.1: Validation table for our implementation of the CMS dilepton analysis [78, 79] in `Atom`.

The benchmark point considered in the CMS analysis has a sbottom of mass 400 GeV decaying via $\tilde{b} \to \tilde{\chi}_2^0 b$ with 100%. The second lightest neutralino then undergoes an off-shell Z decay with SM branching ratios. We show the good agreement between the CMS results and our implemented analysis in `Atom` in table A.1. There, we give the event numbers in the central and forward signal regions as quoted by the CMS collaboration and their ratio to our results obtained with `Atom`.

$(m_{\tilde{t}}, m_{\tilde{\chi}_1^\pm}, m_{\tilde{\chi}_1^0}) = (400, 390, 195)$ GeV	SF	`Atom`/Exp	DF	`Atom`/Exp
$\Delta\phi > 1$	1834.9	1.09	2390.1	1.06
$\Delta\phi_b$	1402.8	1.07	1800.5	1.07
$m_{T2} > 90$ GeV	396.5	1.02	500.0	1.09
$m_{T2} > 120$ GeV	211.8	1.01	284.4	1.1
$m_{T2} > 100$ GeV, $p_{T,\text{jet}} > 100$ GeV	21.7	1.4	35.0	0.99
$m_{T2} > 110$ GeV, $p_{T,\text{jet}} > 20$ GeV	86.0	0.95	116.1	0.89

TABLE A.2: Validation table for our implementation of the ATLAS stop search with two leptons [116] in `Atom`.

Additionally, we provide validation results for the stop search because of the strong constraints that we derive from this analysis. The ATLAS benchmark scenario consists of a stop decaying to $\tilde{\chi}_1^\pm + b$ with 100% probability followed by a decay of $\tilde{\chi}_1^\pm$ via a W into $\tilde{\chi}_1^0$ and Standard Model particles. We show our validation in table A.2. In this table we present event numbers for the same-flavour (SF) and different-flavour (DF) case as given by ATLAS and their ratio to our results in the column `Atom`/Exp.

Appendix B

Parameter values for pMSSM scan

In table B.1 we give additional pMSSM input parameters as well as the sum of the branching ratio of $\tilde{b}_1$ to $\tilde{\chi}_2^0$, $\tilde{\chi}_3^0$. These points were used to scan the right-handed sbottom-higgsino model. Calculation of the physical SUSY masses and branching ratios was performed using SPheno [101, 102].

	$\Delta m(\tilde{b}, \tilde{\chi}_2^0)$ =50	$\Delta m(\tilde{b}, \tilde{\chi}_2^0)$ =90	$\Delta m(\tilde{b}, \tilde{\chi}_2^0)$ =130	$\Delta m(\tilde{b}, \tilde{\chi}_2^0)$ =170
$m_{\tilde{b}}$ =280	(229,157,0.48)	(183,157,0.63)	(140,157,0.69)	(96,157,0.63)
$m_{\tilde{b}}$ =320	(270,215,0.48)	(228,215,0.63)	(183,215,0.69)	(140,215,0.67)
$m_{\tilde{b}}$ =360	(307,263,0.46)	(269,263,0.63)	(228,263,0.69)	(183,263,0.7)
$m_{\tilde{b}}$ =400	(345,310,0.46)	(307,310,0.63)	(269,310,0.7)	(228,310,0.71)

TABLE B.1: Additional information about the right-handed sbottom-higgsino model. We give values for (μ, $m_{\tilde{b}_R}$,$\sum_{i=2,3} BR(\tilde{b} \to b\, N_i)$) for each model point. All masses and mass differences are given in GeV.

Bibliography

[1] S. Chatrchyan *et al.*, "Observation of a new boson at a mass of 125 GeV with the CMS experiment at the LHC," *Phys.Lett.*, vol. B716, pp. 30–61, 2012.

[2] G. Aad *et al.*, "Observation of a new particle in the search for the Standard Model Higgs boson with the ATLAS detector at the LHC," *Phys.Lett.*, vol. B716, pp. 1–29, 2012.

[3] V. C. Rubin, N. Thonnard, and W. K. Ford, Jr., "Rotational properties of 21 SC galaxies with a large range of luminosities and radii, from NGC 4605 /R = 4kpc/ to UGC 2885 /R = 122 kpc/," *Astrophys. J.*, vol. 238, p. 471, 1980.

[4] K. G. Begeman, A. H. Broeils, and R. H. Sanders, "Extended rotation curves of spiral galaxies: Dark haloes and modified dynamics," *Mon. Not. Roy. Astron. Soc.*, vol. 249, p. 523, 1991.

[5] J. F. Navarro, C. S. Frenk, and S. D. M. White, "The Structure of cold dark matter halos," *Astrophys. J.*, vol. 462, pp. 563–575, 1996.

[6] B. Moore, "Evidence against dissipationless dark matter from observations of galaxy haloes," *Nature*, vol. 370, p. 629, 1994.

[7] G. Gentile, P. Salucci, U. Klein, D. Vergani, and P. Kalberla, "The Cored distribution of dark matter in spiral galaxies," *Mon. Not. Roy. Astron. Soc.*, vol. 351, p. 903, 2004.

[8] A. Del Popolo, J. A. S. Lima, J. C. Fabris, and D. C. Rodrigues, "A unified solution to the small scale problems of the ΛCDM model," *JCAP*, vol. 1404, p. 021, 2014.

[9] A. Friedman, "On the Curvature of space," *Z. Phys.*, vol. 10, pp. 377–386, 1922. [Gen. Rel. Grav.31,1991(1999)].

[10] F. Zwicky, "Die Rotverschiebung von extragalaktischen Nebeln," *Helv. Phys. Acta*, vol. 6, pp. 110–127, 1933.

[11] R. G. Carlberg, H. K. C. Yee, and E. Ellingson, "The Average mass and light profiles of galaxy clusters," *Astrophys. J.*, vol. 478, p. 462, 1997.

[12] L. P. David, C. Jones, and W. Forman, "Cosmological implications of ROSAT observations of groups and clusters of galaxies," *Astrophys. J.*, vol. 445, pp. 578–590, 1995.

[13] J. A. Tyson, R. A. Wenk, and F. Valdes, "Detection of systematic gravitational lens galaxy image alignments - Mapping dark matter in galaxy clusters," *Astrophys. J.*, vol. 349, pp. L1–L4, 1990.

[14] N. A. Bahcall and X.-h. Fan, "The Most massive distant clusters: Determining omega and sigma_8," *Astrophys. J.*, vol. 504, p. 1, 1998.

[15] D. Clowe, M. Bradac, A. H. Gonzalez, M. Markevitch, S. W. Randall, C. Jones, and D. Zaritsky, "A direct empirical proof of the existence of dark matter," *Astrophys. J.*, vol. 648, pp. L109–L113, 2006.

[16] D. Harvey, R. Massey, T. Kitching, A. Taylor, and E. Tittley, "The non-gravitational interactions of dark matter in colliding galaxy clusters," *Science*, vol. 347, pp. 1462–1465, 2015.

[17] R. Massey *et al.*, "The behaviour of dark matter associated with four bright cluster galaxies in the 10 kpc core of Abell 3827," *Mon. Not. Roy. Astron. Soc.*, vol. 449, no. 4, pp. 3393–3406, 2015.

[18] S. Perlmutter *et al.*, "Measurements of Omega and Lambda from 42 high redshift supernovae," *Astrophys. J.*, vol. 517, pp. 565–586, 1999.

[19] A. G. Riess *et al.*, "Observational evidence from supernovae for an accelerating universe and a cosmological constant," *Astron. J.*, vol. 116, pp. 1009–1038, 1998.

[20] P. de Bernardis *et al.*, "A Flat universe from high resolution maps of the cosmic microwave background radiation," *Nature*, vol. 404, pp. 955–959, 2000.

[21] T. P. Walker, G. Steigman, D. N. Schramm, K. A. Olive, and H.-S. Kang, "Primordial nucleosynthesis redux," *Astrophys. J.*, vol. 376, pp. 51–69, 1991.

[22] P. Ade *et al.*, "Planck 2013 results. XVI. Cosmological parameters," *Astron.Astrophys.*, vol. 571, p. A16, 2014.

[23] P. Ade *et al.*, "Planck 2015 results. XIII. Cosmological parameters," 2015.

[24] E. W. Kolb and M. S. Turner in *The Early Universe* (D. Pines, ed.), Westview Press, 1990.

[25] G. Belanger, F. Boudjema, A. Pukhov, and A. Semenov, "micrOMEGAs3: A program for calculating dark matter observables," *Comput.Phys.Commun.*, vol. 185, pp. 960–985, 2014.

[26] G. Bertone, D. Hooper, and J. Silk, "Particle dark matter: Evidence, candidates and constraints," *Phys. Rept.*, vol. 405, pp. 279–390, 2005.

[27] D. Hooper, "Particle Dark Matter," in *Proceedings of Theoretical Advanced Study Institute in Elementary Particle Physics on The dawn of the LHC era (TASI 2008)*, pp. 709–764, 2010.

[28] L. J. Hall, K. Jedamzik, J. March-Russell, and S. M. West, "Freeze-In Production of FIMP Dark Matter," *JHEP*, vol. 03, p. 080, 2010.

[29] D. E. Kaplan, M. A. Luty, and K. M. Zurek, "Asymmetric Dark Matter," *Phys. Rev.*, vol. D79, p. 115016, 2009.

[30] M. Ackermann *et al.*, "Searching for Dark Matter Annihilation from Milky Way Dwarf Spheroidal Galaxies with Six Years of Fermi-LAT Data," 2015.

[31] L. Goodenough and D. Hooper, "Possible Evidence For Dark Matter Annihilation In The Inner Milky Way From The Fermi Gamma Ray Space Telescope," 2009.

[32] D. Hooper and L. Goodenough, "Dark Matter Annihilation in The Galactic Center As Seen by the Fermi Gamma Ray Space Telescope," *Phys. Lett.*, vol. B697, pp. 412–428, 2011.

[33] N. Okada and O. Seto, "Gamma ray emission in Fermi bubbles and Higgs portal dark matter," *Phys. Rev.*, vol. D89, no. 4, p. 043525, 2014.

[34] C. Boehm, M. J. Dolan, C. McCabe, M. Spannowsky, and C. J. Wallace, "Extended gamma-ray emission from Coy Dark Matter," *JCAP*, vol. 1405, p. 009, 2014.

[35] C. Boehm, M. J. Dolan, and C. McCabe, "A weighty interpretation of the Galactic Centre excess," *Phys. Rev.*, vol. D90, no. 2, p. 023531, 2014.

[36] T. Bringmann, M. Vollmann, and C. Weniger, "Updated cosmic-ray and radio constraints on light dark matter: Implications for the GeV gamma-ray excess at the Galactic center," *Phys. Rev.*, vol. D90, no. 12, p. 123001, 2014.

[37] M. Aguilar *et al.*, "First Result from the Alpha Magnetic Spectrometer on the International Space Station: Precision Measurement of the Positron Fraction in Primary Cosmic Rays of 0.5–350 GeV," *Phys.Rev.Lett.*, vol. 110, p. 141102, 2013.

[38] L. Bergstrom, T. Bringmann, I. Cholis, D. Hooper, and C. Weniger, "New limits on dark matter annihilation from AMS cosmic ray positron data," *Phys.Rev.Lett.*, vol. 111, p. 171101, 2013.

[39] A. Ibarra, A. S. Lamperstorfer, and J. Silk, "Dark matter annihilations and decays after the AMS-02 positron measurements," *Phys. Rev.*, vol. D89, no. 6, p. 063539, 2014.

[40] O. Adriani *et al.*, "A statistical procedure for the identification of positrons in the PAMELA experiment," *Astropart. Phys.*, vol. 34, pp. 1–11, 2010.

[41] N. Arkani-Hamed, K. Blum, R. T. D'Agnolo, and J. Fan, "2:1 for Naturalness at the LHC?," *JHEP*, vol. 01, p. 149, 2013.

[42] J. Billard, L. Strigari, and E. Figueroa-Feliciano, "Implication of neutrino backgrounds on the reach of next generation dark matter direct detection experiments," *Phys.Rev.*, vol. D89, no. 2, p. 023524, 2014.

[43] P. Cushman, C. Galbiati, D. McKinsey, H. Robertson, T. Tait, *et al.*, "Working Group Report: WIMP Dark Matter Direct Detection," 2013.

[44] D. Akerib *et al.*, "First results from the LUX dark matter experiment at the Sanford Underground Research Facility," *Phys.Rev.Lett.*, vol. 112, p. 091303, 2014.

[45] R. Bernabei, P. Belli, F. Cappella, V. Caracciolo, S. Castellano, *et al.*, "Final model independent results of DAMA/LIBRA-phase1 and perspectives of phase2," *Phys.Part.Nucl.*, vol. 46, no. 2, pp. 138–146, 2015.

[46] C. E. Aalseth, P. S. Barbeau, N. S. Bowden, B. Cabrera-Palmer, J. Colaresi, J. I. Collar, S. Dazeley, P. de Lurgio, J. E. Fast, N. Fields, C. H. Greenberg, T. W. Hossbach, M. E. Keillor, J. D. Kephart, M. G. Marino, H. S. Miley, M. L. Miller, J. L. Orrell, D. C. Radford, D. Reyna, O. Tench, T. D. Van Wechel, J. F. Wilkerson, and K. M. Yocum, "Results from a search for light-mass dark matter with a p-type point contact germanium detector," *Phys. Rev. Lett.*, vol. 106, p. 131301, Mar 2011.

[47] J. H. Davis, C. McCabe, and C. Boehm, "Quantifying the evidence for Dark Matter in CoGeNT data," *JCAP*, vol. 1408, p. 014, 2014.

[48] O. Buchmueller, M. J. Dolan, S. A. Malik, and C. McCabe, "Characterising dark matter searches at colliders and direct detection experiments: Vector mediators," *JHEP*, vol. 01, p. 037, 2015.

[49] S. Malik *et al.*, "Interplay and Characterization of Dark Matter Searches at Colliders and in Direct Detection Experiments," 2014.

[50] A. D. Sakharov, "Violation of CP Invariance, c Asymmetry, and Baryon Asymmetry of the Universe," *Pisma Zh. Eksp. Teor. Fiz.*, vol. 5, pp. 32–35, 1967. [Usp. Fiz. Nauk161,61(1991)].

[51] K. Olive *et al.*, "Review of Particle Physics," *Chin.Phys.*, vol. C38, p. 090001, 2014.

[52] B. D. Fields, "The primordial lithium problem," *Ann. Rev. Nucl. Part. Sci.*, vol. 61, pp. 47–68, 2011.

[53] G. 't Hooft, "Symmetry Breaking Through Bell-Jackiw Anomalies," *Phys. Rev. Lett.*, vol. 37, pp. 8–11, 1976.

[54] J. M. Cline, "Baryogenesis," in *Les Houches Summer School - Session 86: Particle Physics and Cosmology: The Fabric of Spacetime Les Houches, France, July 31-August 25, 2006*, 2006.

[55] S. L. Adler, "Axial vector vertex in spinor electrodynamics," *Phys. Rev.*, vol. 177, pp. 2426–2438, 1969.

[56] J. S. Bell and R. Jackiw, "A PCAC puzzle: pi0 –¿ gamma gamma in the sigma model," *Nuovo Cim.*, vol. A60, pp. 47–61, 1969.

[57] V. A. Kuzmin, V. A. Rubakov, and M. E. Shaposhnikov, "On the Anomalous Electroweak Baryon Number Nonconservation in the Early Universe," *Phys. Lett.*, vol. B155, p. 36, 1985.

[58] M. E. Shaposhnikov, "Possible Appearance of the Baryon Asymmetry of the Universe in an Electroweak Theory," *JETP Lett.*, vol. 44, pp. 465–468, 1986. [Pisma Zh. Eksp. Teor. Fiz.44,364(1986)].

[59] A. I. Bochkarev and M. E. Shaposhnikov, "Electroweak Production of Baryon Asymmetry and Upper Bounds on the Higgs and Top Masses," *Mod. Phys. Lett.*, vol. A2, p. 417, 1987.

[60] M. Fukugita and T. Yanagida, "Baryogenesis Without Grand Unification," *Phys. Lett.*, vol. B174, p. 45, 1986.

[61] P. Minkowski, "$\mu \to e\gamma$ at a Rate of One Out of 10^9 Muon Decays?," *Phys. Lett.*, vol. B67, pp. 421–428, 1977.

[62] P. Ramond, "The Family Group in Grand Unified Theories," in *International Symposium on Fundamentals of Quantum Theory and Quantum Field Theory Palm Coast, Florida, February 25-March 2, 1979*, pp. 265–280, 1979.

[63] T. Yanagida, "Horizontal Symmetry and masses of neutrinos," *Conf. Proc.*, vol. C7902131, pp. 95–99, 1979. [Conf. Proc.C7902131,95(1979)].

[64] M. Gell-Mann, P. Ramond, and R. Slansky, "Complex Spinors and Unified Theories," *Conf. Proc.*, vol. C790927, pp. 315–321, 1979.

[65] F. F. Deppisch, J. Harz, M. Hirsch, W.-C. Huang, and H. Päs, "Falsifying High-Scale Baryogenesis with Neutrinoless Double Beta Decay and Lepton Flavor Violation," *Phys. Rev.*, vol. D92, p. 036005, 2015.

[66] J.-M. Frere, T. Hambye, and G. Vertongen, "Is leptogenesis falsifiable at LHC?," *JHEP*, vol. 01, p. 051, 2009.

[67] F. F. Deppisch, J. Harz, and M. Hirsch, "Falsifying High-Scale Leptogenesis at the LHC," *Phys. Rev. Lett.*, vol. 112, p. 221601, 2014.

[68] M. Yoshimura, "Unified Gauge Theories and the Baryon Number of the Universe," *Phys. Rev. Lett.*, vol. 41, pp. 281–284, 1978. [Erratum: Phys. Rev. Lett.42,746(1979)].

[69] S. P. Martin, "A Supersymmetry primer," 1997. [Adv. Ser. Direct. High Energy Phys.18,1(1998)].

[70] S. R. Coleman and J. Mandula, "All Possible Symmetries of the S Matrix," *Phys. Rev.*, vol. 159, pp. 1251–1256, 1967.

[71] R. Haag, J. T. Lopuszanski, and M. Sohnius, "All Possible Generators of Supersymmetries of the s Matrix," *Nucl. Phys.*, vol. B88, p. 257, 1975.

[72] P. Grothaus, S. P. Liew, and K. Sakurai, "A closer look at a hint of SUSY at the 8 TeV LHC," *JHEP*, vol. 05, p. 133, 2015.

[73] M. Fairbairn and P. Grothaus, "Baryogenesis and Dark Matter with Vector-like Fermions," *JHEP*, vol. 10, p. 176, 2013.

[74] P. Grothaus, M. Fairbairn, and J. Monroe, "Directional Dark Matter Detection Beyond the Neutrino Bound," *Phys. Rev.*, vol. D90, no. 5, p. 055018, 2014.

[75] G. Aad *et al.*, "Search for direct production of charginos and neutralinos in events with three leptons and missing transverse momentum in $\sqrt{s} = 8$TeV pp collisions with the ATLAS detector," *JHEP*, vol. 04, p. 169, 2014.

[76] G. Aad *et al.*, "Search for direct production of charginos, neutralinos and sleptons in final states with two leptons and missing transverse momentum in pp collisions at $\sqrt{s} = 8$ TeV with the ATLAS detector," *JHEP*, vol. 1405, p. 071, 2014.

[77] "ATLAS Supersymmetry (SUSY) searches." `https://twiki.cern.ch/twiki/bin/view/AtlasPublic/SupersymmetryPublicResults`, 2015. Accessed: 2015-08-14.

[78] C. Collaboration, "Search for physics beyond the standard model in events with two opposite-sign same-flavor leptons, jets, and missing transverse energy in pp collisions at sqrt[s] = 8 TeV," 2014.

[79] V. Khachatryan *et al.*, "Search for physics beyond the standard model in events with two leptons, jets, and missing transverse momentum in pp collisions at sqrt(s) = 8 TeV," *JHEP*, vol. 04, p. 124, 2015.

[80] G. Arnison *et al.*, "Experimental Observation of Isolated Large Transverse Energy Electrons with Associated Missing Energy at s**(1/2) = 540-GeV," *Phys. Lett.*, vol. B122, pp. 103–116, 1983.

[81] C. G. Lester and D. J. Summers, "Measuring masses of semiinvisibly decaying particles pair produced at hadron colliders," *Phys. Lett.*, vol. B463, pp. 99–103, 1999.

[82] A. Barr, C. Lester, and P. Stephens, "m(T2): The Truth behind the glamour," *J. Phys.*, vol. G29, pp. 2343–2363, 2003.

[83] G. Aad *et al.*, "The ATLAS Experiment at the CERN Large Hadron Collider," *JINST*, vol. 3, p. S08003, 2008.

[84] S. Chatrchyan *et al.*, "The CMS experiment at the CERN LHC," *JINST*, vol. 3, p. S08004, 2008.

[85] M. Kramer, A. Kulesza, R. van der Leeuw, M. Mangano, S. Padhi, T. Plehn, and X. Portell, "Supersymmetry production cross sections in *pp* collisions at $\sqrt{s} = 7$ TeV," 2012.

[86] V. N. Gribov and L. N. Lipatov, "Deep inelastic e p scattering in perturbation theory," *Sov. J. Nucl. Phys.*, vol. 15, pp. 438–450, 1972. [Yad. Fiz.15,781(1972)].

[87] G. Altarelli and G. Parisi, "Asymptotic Freedom in Parton Language," *Nucl. Phys.*, vol. B126, p. 298, 1977.

[88] Y. L. Dokshitzer, "Calculation of the Structure Functions for Deep Inelastic Scattering and e+ e- Annihilation by Perturbation Theory in Quantum Chromodynamics.," *Sov. Phys. JETP*, vol. 46, pp. 641–653, 1977. [Zh. Eksp. Teor. Fiz.73,1216(1977)].

[89] G. Aad *et al.*, "Search for supersymmetry using final states with one lepton, jets, and missing transverse momentum with the ATLAS detector in $\sqrt{s} = 7$ TeV *pp*," *Phys. Rev. Lett.*, vol. 106, p. 131802, 2011.

[90] W. Beenakker, M. Kramer, T. Plehn, M. Spira, and P. M. Zerwas, "Stop production at hadron colliders," *Nucl. Phys.*, vol. B515, pp. 3–14, 1998.

[91] W. Beenakker, S. Brensing, M. Kramer, A. Kulesza, E. Laenen, and I. Niessen, "Supersymmetric top and bottom squark production at hadron colliders," *JHEP*, vol. 08, p. 098, 2010.

[92] W. Beenakker, S. Brensing, M. n. Kramer, A. Kulesza, E. Laenen, L. Motyka, and I. Niessen, "Squark and Gluino Hadroproduction," *Int. J. Mod. Phys.*, vol. A26, pp. 2637–2664, 2011.

[93] B. Allanach, A. R. Raklev, and A. Kvellestad, "Interpreting a CMS excess in $lljj + missing$-transverse-momentum with the golden cascade of the minimal supersymmetric standard model," *Phys. Rev.*, vol. D91, no. 11, p. 115022, 2015.

[94] I. Hinchliffe, F. E. Paige, M. D. Shapiro, J. Soderqvist, and W. Yao, "Precision SUSY measurements at CERN LHC," *Phys. Rev.*, vol. D55, pp. 5520–5540, 1997.

[95] I. Hinchliffe and F. E. Paige, "Measurements in SUGRA models with large tan beta at CERN LHC," *Phys. Rev.*, vol. D61, p. 095011, 2000.

[96] H. Bachacou, I. Hinchliffe, and F. E. Paige, "Measurements of masses in SUGRA models at CERN LHC," *Phys. Rev.*, vol. D62, p. 015009, 2000.

[97] B. C. Allanach, C. G. Lester, M. A. Parker, and B. R. Webber, "Measuring sparticle masses in nonuniversal string inspired models at the LHC," *JHEP*, vol. 09, p. 004, 2000.

[98] G. Aad *et al.*, "Search for supersymmetry in events containing a same-flavour opposite-sign dilepton pair, jets, and large missing transverse momentum in $\sqrt{s} = 8$ TeV pp collisions with the ATLAS detector," *Eur. Phys. J.*, vol. C75, no. 7, p. 318, 2015.

[99] P. Huang and C. E. M. Wagner, "CMS kinematic edge from sbottoms," *Phys. Rev.*, vol. D91, no. 1, p. 015014, 2015.

[100] B. Allanach, A. Alves, F. S. Queiroz, K. Sinha, and A. Strumia, "Interpreting the CMS $\ell^+\ell^- jj\not{E}_T$ Excess with a Leptoquark Model," 2015.

[101] W. Porod, "SPheno, a program for calculating supersymmetric spectra, SUSY particle decays and SUSY particle production at e+ e- colliders," *Comput. Phys. Commun.*, vol. 153, pp. 275–315, 2003.

[102] W. Porod and F. Staub, "SPheno 3.1: Extensions including flavour, CP-phases and models beyond the MSSM," *Comput. Phys. Commun.*, vol. 183, pp. 2458–2469, 2012.

[103] I.W. Kim, M. Papucci, K. Sakurai and A. Weiler, "ATOM: Automated Testing Of Models," in preparation.

[104] T. Sjostrand, S. Mrenna, and P. Z. Skands, "PYTHIA 6.4 Physics and Manual," *JHEP*, vol. 05, p. 026, 2006.

[105] M. Papucci, J. T. Ruderman, and A. Weiler, "Natural SUSY Endures," *JHEP*, vol. 09, p. 035, 2012.

[106] M. Papucci, K. Sakurai, A. Weiler, and L. Zeune, "Fastlim: a fast LHC limit calculator," *Eur. Phys. J.*, vol. C74, no. 11, p. 3163, 2014.

[107] J. S. Kim, K. Rolbiecki, K. Sakurai, and J. Tattersall, "'Stop' that ambulance! New physics at the LHC?," *JHEP*, vol. 12, p. 010, 2014.

[108] M. Drees, H. Dreiner, D. Schmeier, J. Tattersall, and J. S. Kim, "CheckMATE: Confronting your Favourite New Physics Model with LHC Data," *Comput. Phys. Commun.*, vol. 187, pp. 227–265, 2014.

[109] T. A. collaboration, "Search for squarks and gluinos with the ATLAS detector in final states with jets and missing transverse momentum and 20.3 fb^{-1} of $\sqrt{s} = 8$ TeV proton-proton collision data," 2013.

[110] G. Aad *et al.*, "Search for squarks and gluinos with the ATLAS detector in final states with jets and missing transverse momentum using $\sqrt{s} = 8$ TeV proton–proton collision data," *JHEP*, vol. 09, p. 176, 2014.

[111] G. Aad *et al.*, "Search for direct third-generation squark pair production in final states with missing transverse momentum and two b-jets in $\sqrt{s} = 8$ TeV pp collisions with the ATLAS detector," *JHEP*, vol. 1310, p. 189, 2013.

[112] "Search for direct top squark pair production in final states with one isolated lepton, jets, and missing transverse momentum in $sqrts = 8$,TeV pp collisions using 21 fb^{-1} of ATLAS data," 2013.

[113] T. A. collaboration, "Search for squarks and gluinos in events with isolated leptons, jets and missing transverse momentum at $\sqrt{s} = 8$ TeV with the ATLAS detector," 2013.

[114] "Search for strongly produced superpartners in final states with two same sign leptons with the ATLAS detector using 21 fb-1 of proton-proton collisions at sqrt(s)=8 TeV.," 2013.

[115] T. A. collaboration, "Search for direct top squark pair production in final states with two leptons in $\sqrt{s} = 8$ TeV pp collisions using 20fb^{-1} of ATLAS data.," 2013.

[116] G. Aad *et al.*, "Search for direct top-squark pair production in final states with two leptons in pp collisions at $\sqrt{s} = 8$TeV with the ATLAS detector," *JHEP*, vol. 06, p. 124, 2014.

[117] G. Aad *et al.*, "Search for supersymmetry at $\sqrt{s}$=8 TeV in final states with jets and two same-sign leptons or three leptons with the ATLAS detector," *JHEP*, vol. 06, p. 035, 2014.

[118] V. Khachatryan *et al.*, "Searches for electroweak production of charginos, neutralinos, and sleptons decaying to leptons and W, Z, and Higgs bosons in pp collisions at 8 TeV," *Eur. Phys. J.*, vol. C74, no. 9, p. 3036, 2014.

[119] C. Collaboration, "A search for anomalous production of events with three or more leptons using 19.5/fb of sqrt(s)=8 TeV LHC data," 2013.

[120] S. Chatrchyan *et al.*, "Search for top-squark pair production in the single-lepton final state in pp collisions at $\sqrt{s}$ = 8 TeV," *Eur.Phys.J.*, vol. C73, no. 12, p. 2677, 2013.

[121] V. Khachatryan *et al.*, "Search for neutral MSSM Higgs bosons decaying to a pair of tau leptons in pp collisions," *JHEP*, vol. 10, p. 160, 2014.

[122] E. Fermi, "An attempt of a theory of beta radiation. 1.," *Z. Phys.*, vol. 88, pp. 161–177, 1934.

[123] Y. Nambu and G. Jona-Lasinio, "Dynamical Model of Elementary Particles Based on an Analogy with Superconductivity. 1.," *Phys. Rev.*, vol. 122, pp. 345–358, 1961.

[124] P. W. Anderson, "Plasmons, Gauge Invariance, and Mass," *Phys. Rev.*, vol. 130, pp. 439–442, 1963.

[125] F. Englert and R. Brout, "Broken Symmetry and the Mass of Gauge Vector Mesons," *Phys. Rev. Lett.*, vol. 13, pp. 321–323, 1964.

[126] P. W. Higgs, "Broken Symmetries and the Masses of Gauge Bosons," *Phys. Rev. Lett.*, vol. 13, pp. 508–509, 1964.

[127] G. S. Guralnik, C. R. Hagen, and T. W. B. Kibble, "Global Conservation Laws and Massless Particles," *Phys. Rev. Lett.*, vol. 13, pp. 585–587, 1964.

[128] S. Weinberg, "A Model of Leptons," *Phys. Rev. Lett.*, vol. 19, pp. 1264–1266, 1967.

[129] A. Salam, "Weak and Electromagnetic Interactions," *Conf. Proc.*, vol. C680519, pp. 367–377, 1968.

[130] S. L. Glashow, "Partial Symmetries of Weak Interactions," *Nucl. Phys.*, vol. 22, pp. 579–588, 1961.

[131] F. Abe *et al.*, "Observation of top quark production in $\bar{p}p$ collisions," *Phys. Rev. Lett.*, vol. 74, pp. 2626–2631, 1995.

[132] S. Abachi *et al.*, "Search for high mass top quark production in $p\bar{p}$ collisions at $\sqrt{s} = 1.8$ TeV," *Phys. Rev. Lett.*, vol. 74, pp. 2422–2426, 1995.

[133] P. P. Giardino, K. Kannike, I. Masina, M. Raidal, and A. Strumia, "The universal Higgs fit," *JHEP*, vol. 1405, p. 046, 2014.

[134] J. Ellis and T. You, "Updated Global Analysis of Higgs Couplings," *JHEP*, vol. 1306, p. 103, 2013.

[135] A. Falkowski, F. Riva, and A. Urbano, "Higgs at last," *JHEP*, vol. 1311, p. 111, 2013.

[136] "Measurements of the properties of the Higgs-like boson in the two photon decay channel with the ATLAS detector using 25 fb^{-1} of proton-proton collision data," *ATLAS-CONF-2013-012, ATLAS-COM-CONF-2013-015*, 2013.

[137] C. Collaboration, "Evidence for a new state decaying into two photons in the search for the standard model Higgs boson in pp collisions," *CMS-PAS-HIG-12-015*, 2012.

[138] J. R. Andersen *et al.*, "Handbook of LHC Higgs Cross Sections: 3. Higgs Properties," 2013.

[139] T. A. collaboration, "Measurements of the Higgs boson production and decay rates and coupling strengths using pp collision data at s = 7 and 8 TeV in the ATLAS experiment," *ATLAS-CONF-2015-007, ATLAS-COM-CONF-2015-011*, 2015.

[140] V. Khachatryan *et al.*, "Observation of the diphoton decay of the Higgs boson and measurement of its properties," *Eur.Phys.J.*, vol. C74, no. 10, p. 3076, 2014.

[141] J. R. Ellis, M. K. Gaillard, and D. V. Nanopoulos, "A Phenomenological Profile of the Higgs Boson," *Nucl.Phys.*, vol. B106, p. 292, 1976.

[142] A. Djouadi, "The Anatomy of electro-weak symmetry breaking. I: The Higgs boson in the standard model," *Phys.Rept.*, vol. 457, pp. 1–216, 2008.

[143] M. Carena, I. Low, and C. E. Wagner, "Implications of a Modified Higgs to Diphoton Decay Width," *JHEP*, vol. 1208, p. 060, 2012.

[144] N. Arkani-Hamed, K. Blum, R. T. D'Agnolo, and J. Fan, "2:1 for Naturalness at the LHC?," *JHEP*, vol. 1301, p. 149, 2013.

[145] L. G. Almeida, E. Bertuzzo, P. A. Machado, and R. Z. Funchal, "Does $H \to \gamma\gamma$ Taste like vanilla New Physics?," *JHEP*, vol. 1211, p. 085, 2012.

[146] J. Kearney, A. Pierce, and N. Weiner, "Vectorlike Fermions and Higgs Couplings," *Phys.Rev.*, vol. D86, p. 113005, 2012.

[147] M. Voloshin, "CP Violation in Higgs Diphoton Decay in Models with Vectorlike Heavy Fermions," *Phys.Rev.*, vol. D86, p. 093016, 2012.

[148] B. Batell, S. Jung, and H. M. Lee, "Singlet Assisted Vacuum Stability and the Higgs to Diphoton Rate," *JHEP*, vol. 1301, p. 135, 2013.

[149] W.-Z. Feng and P. Nath, "Higgs diphoton rate and mass enhancement with vectorlike leptons and the scale of supersymmetry," *Phys.Rev.*, vol. D87, no. 7, p. 075018, 2013.

[150] A. Joglekar, P. Schwaller, and C. E. Wagner, "Dark Matter and Enhanced Higgs to Di-photon Rate from Vector-like Leptons," *JHEP*, vol. 1212, p. 064, 2012.

[151] C. Arina, R. N. Mohapatra, and N. Sahu, "Co-genesis of Matter and Dark Matter with Vector-like Fourth Generation Leptons," *Phys.Lett.*, vol. B720, pp. 130–136, 2013.

[152] P. Fileviez Perez and M. B. Wise, "Baryon Asymmetry and Dark Matter Through the Vector-Like Portal," *JHEP*, vol. 1305, p. 094, 2013.

[153] P. Schwaller, T. M. P. Tait, and R. Vega-Morales, "Dark matter and vectorlike leptons from gauged lepton number," *Phys.Rev.*, vol. D88, no. 3, p. 035001, 2013.

[154] H. Davoudiasl, I. Lewis, and E. Ponton, "Electroweak Phase Transition, Higgs Diphoton Rate, and New Heavy Fermions," *Phys.Rev.*, vol. D87, no. 9, p. 093001, 2013.

[155] P. Fileviez Perez and M. B. Wise, "Breaking Local Baryon and Lepton Number at the TeV Scale," *JHEP*, vol. 1108, p. 068, 2011.

[156] M. Duerr, P. Fileviez Perez, and M. B. Wise, "Gauge Theory for Baryon and Lepton Numbers with Leptoquarks," *Phys.Rev.Lett.*, vol. 110, p. 231801, 2013.

[157] H. K. Dreiner, H. E. Haber, and S. P. Martin, "Two-component spinor techniques and Feynman rules for quantum field theory and supersymmetry," *Phys. Rept.*, vol. 494, pp. 1–196, 2010.

[158] G. Belanger, N. D. Christensen, A. Pukhov, and A. Semenov, "SLHAplus: a library for implementing extensions of the standard model," *Comput.Phys.Commun.*, vol. 182, pp. 763–774, 2011.

[159] B. Batell, S. Gori, and L.-T. Wang, "Higgs Couplings and Precision Electroweak Data," *JHEP*, vol. 1301, p. 139, 2013.

[160] R. Dermisek and A. Raval, "Explanation of the Muon g-2 Anomaly with Vectorlike Leptons and its Implications for Higgs Decays," *Phys.Rev.*, vol. D88, p. 013017, 2013.

[161] M. E. Peskin and T. Takeuchi, "Estimation of oblique electroweak corrections," *Phys.Rev.*, vol. D46, pp. 381–409, 1992.

[162] F. del Aguila, J. de Blas, and M. Perez-Victoria, "Effects of new leptons in Electroweak Precision Data," *Phys. Rev.*, vol. D78, p. 013010, 2008.

[163] G. Cynolter and E. Lendvai, "Electroweak Precision Constraints on Vector-like Fermions," *Eur. Phys. J.*, vol. C58, pp. 463–469, 2008.

[164] J. Beringer *et al.*, "Review of Particle Physics (RPP)," *Phys.Rev.*, vol. D86, p. 010001, 2012.

[165] P. Abreu *et al.*, "Searches for heavy neutrinos from Z decays," *Phys.Lett.*, vol. B274, pp. 230–238, 1992.

[166] A. Semenov, "LanHEP - a package for automatic generation of Feynman rules from the Lagrangian. Updated version 3.1," 2010.

[167] G. Belanger, F. Boudjema, P. Brun, A. Pukhov, S. Rosier-Lees, *et al.*, "Indirect search for dark matter with micrOMEGAs2.4," *Comput.Phys.Commun.*, vol. 182, pp. 842–856, 2011.

[168] E. Aprile *et al.*, "Dark Matter Results from 225 Live Days of XENON100 Data," *Phys.Rev.Lett.*, vol. 109, p. 181301, 2012.

[169] A. Belyaev, N. D. Christensen, and A. Pukhov, "CalcHEP 3.4 for collider physics within and beyond the Standard Model," *Comput.Phys.Commun.*, vol. 184, pp. 1729–1769, 2013.

[170] S. Coleman and E. Weinberg, "Radiative corrections as the origin of spontaneous symmetry breaking," *Phys. Rev. D*, vol. 7, pp. 1888–1910, Mar 1973.

[171] G. W. Anderson and L. J. Hall, "The Electroweak phase transition and baryogenesis," *Phys.Rev.*, vol. D45, pp. 2685–2698, 1992.

[172] G. F. Giudice, "Electroweak phase transition in supersymmetry," *Phys. Rev. D*, vol. 45, pp. 3177–3182, May 1992.

[173] M. Carena, A. Megevand, M. Quiros, and C. E. Wagner, "Electroweak baryogenesis and new TeV fermions," *Nucl.Phys.*, vol. B716, pp. 319–351, 2005.

[174] L. Dolan and R. Jackiw, "Symmetry Behavior at Finite Temperature," *Phys. Rev.*, vol. D9, pp. 3320–3341, 1974.

[175] E. Aprile *et al.*, "Limits on spin-dependent WIMP-nucleon cross sections from 225 live days of XENON100 data," *Phys.Rev.Lett.*, vol. 111, no. 2, p. 021301, 2013.

[176] N. F. Bell, J. B. Dent, T. D. Jacques, and T. J. Weiler, "Electroweak Bremsstrahlung in Dark Matter Annihilation," *Phys. Rev.*, vol. D78, p. 083540, 2008.

[177] F. Luo and T. You, "Enhancement of Majorana Dark Matter Annihilation Through Higgs Bremsstrahlung," *JCAP*, vol. 1312, p. 024, 2013.

[178] J. Elias-Miro, J. R. Espinosa, G. F. Giudice, G. Isidori, A. Riotto, *et al.*, "Higgs mass implications on the stability of the electroweak vacuum," *Phys.Lett.*, vol. B709, pp. 222–228, 2012.

[179] G. Degrassi, S. Di Vita, J. Elias-Miro, J. R. Espinosa, G. F. Giudice, *et al.*, "Higgs mass and vacuum stability in the Standard Model at NNLO," *JHEP*, vol. 1208, p. 098, 2012.

[180] D. Buttazzo, G. Degrassi, P. P. Giardino, G. F. Giudice, F. Sala, *et al.*, "Investigating the near-criticality of the Higgs boson," *JHEP*, vol. 1312, p. 089, 2013.

[181] A. Joglekar, P. Schwaller, and C. E. M. Wagner, "A Supersymmetric Theory of Vector-like Leptons," *JHEP*, vol. 1307, p. 046, 2013.

[182] B. Kyae and C. S. Shin, "Vector-like leptons and extra gauge symmetry for the natural Higgs boson," *JHEP*, vol. 1306, p. 102, 2013.

[183] J. D. Lewin and P. F. Smith, "Review of mathematics, numerical factors, and corrections for dark matter experiments based on elastic nuclear recoil," *Astropart. Phys.*, vol. 6, pp. 87–112, 1996.

[184] M. Weber and W. de Boer, "Determination of the Local Dark Matter Density in our Galaxy," *Astron.Astrophys.*, vol. 509, p. A25, 2010.

[185] R. Catena and P. Ullio, "A novel determination of the local dark matter density," *JCAP*, vol. 1008, p. 004, 2010.

[186] M. C. "Smith and others", "The rave survey: constraining the local galactic escape speed," *Monthly Notices of the Royal Astronomical Society*, vol. 379, no. 2, pp. 755–772, 2007.

[187] T. Piffl, C. Scannapieco, J. Binney, M. Steinmetz, R.-D. Scholz, *et al.*, "The RAVE survey: the Galactic escape speed and the mass of the Milky Way," *Astron.Astrophys.*, vol. 562, p. A91, 2014.

[188] M. Kamionkowski and A. Kinkhabwala, "Galactic halo models and particle dark matter detection," *Phys.Rev.*, vol. D57, pp. 3256–3263, 1998.

[189] M. Brhlik and L. Roszkowski, "WIMP velocity impact on direct dark matter searches," *Phys.Lett.*, vol. B464, pp. 303–310, 1999.

[190] A. M. Green, "Effect of halo modeling on WIMP exclusion limits," *Phys.Rev.*, vol. D66, p. 083003, 2002.

[191] M. Fairbairn and T. Schwetz, "Spin-independent elastic WIMP scattering and the DAMA annual modulation signal," *JCAP*, vol. 0901, p. 037, 2009.

[192] G. Jungman, M. Kamionkowski, and K. Griest, "Supersymmetric dark matter," *Phys. Rept.*, vol. 267, pp. 195–373, 1996.

[193] T. Falk, A. Ferstl, and K. A. Olive, "New contributions to neutralino elastic cross-sections from CP violating phases in the MSSM," *Phys. Rev.*, vol. D59, p. 055009, 1999. [Erratum: Phys. Rev.D60,119904(1999)].

[194] J. L. Feng, J. Kumar, D. Marfatia, and D. Sanford, "Isospin-Violating Dark Matter," *Phys. Lett.*, vol. B703, pp. 124–127, 2011.

[195] C. J. Horowitz and B. D. Serot, "Selfconsistent hartree description of finite nuclei in a relativistic quantum field theory," *Nucl. Phys.*, vol. A368, p. 503, 1981.

[196] "Dark Matter Research, An Introduction to Dark Matter." `https://www.hep.shef.ac.uk/research/dm/intro.php`, 2015. Accessed: 2015-08-28.

[197] C. McCabe, "The Earth's velocity for direct detection experiments," *JCAP*, vol. 1402, p. 027, 2014.

[198] E. Aprile, "The XENON1T Dark Matter Search Experiment," *Springer Proc.Phys.*, vol. C12-02-22, pp. 93–96, 2013.

[199] D. Malling, D. Akerib, H. Araujo, X. Bai, S. Bedikian, *et al.*, "After LUX: The LZ Program," 2011.

[200] M. Boulay, "DEAP-3600 Dark Matter Search at SNOLAB," *J.Phys.Conf.Ser.*, vol. 375, p. 012027, 2012.

[201] D. S. Akerib *et al.*, "The Large Underground Xenon (LUX) experiment," *Nuclear Instruments and Methods in Physics Research A*, vol. 704, pp. 111–126, Mar. 2013.

[202] V. Chepel and H. Araujo, "Liquid noble gas detectors for low energy particle physics," *JINST*, vol. 8, p. R04001, 2013.

[203] V. Lebedenko, H. Araujo, E. Barnes, A. Bewick, R. Cashmore, *et al.*, "Result from the First Science Run of the ZEPLIN-III Dark Matter Search Experiment," *Phys.Rev.*, vol. D80, p. 052010, 2009.

[204] A. M. Green and B. Morgan, "Optimizing WIMP directional detectors," *Astropart.Phys.*, vol. 27, pp. 142–149, 2007.

[205] J. Billard, F. Mayet, J. Macias-Perez, and D. Santos, "Directional detection as a strategy to discover galactic Dark Matter," *Phys.Lett.*, vol. B691, pp. 156–162, 2010.

[206] N. Bozorgnia, G. B. Gelmini, and P. Gondolo, "Ring-like features in directional dark matter detection," *JCAP*, vol. 1206, p. 037, 2012.

[207] J. Billard, F. Mayet, and D. Santos, "Markov Chain Monte Carlo analysis to constrain Dark Matter properties with directional detection," *Phys.Rev.*, vol. D83, p. 075002, 2011.

[208] B. J. Kavanagh, "New directional signatures from the non-relativistic effective field theory of dark matter," 2015.

[209] G. Sciolla, J. Battat, T. Caldwell, D. Dujmic, P. Fisher, *et al.*, "The DMTPC project," *J.Phys.Conf.Ser.*, vol. 179, p. 012009, 2009.

[210] J. P. Lopez *et al.*, "Rejection of Electronic Recoils with the DMTPC Dark Matter Search," *Phys. Procedia*, vol. 37, pp. 575–582, 2012.

[211] J. Monroe, "Status and Prospects of the DMTPC Directional Dark Matter Experiment," *AIP Conf.Proc.*, vol. 1441, pp. 515–517, 2012.

[212] L. M. Capparelli, G. Cavoto, D. Mazzilli, and A. D. Polosa, "Carbon Nanotubes Potentialities in Directional Dark Matter Searches," 2014.

[213] T. Naka, M. Kimura, M. Nakamura, O. Sato, T. Nakano, T. Asada, Y. Tawara, and Y. Suzuki, "R&D Status of Nuclear Emulsion For Directional Dark Matter Search," *EAS Publ. Ser.*, vol. 53, pp. 51–58, 2012.

[214] H. Sekiya, M. Minowa, Y. Shimizu, Y. Inoue, and W. Suganuma, "Measurements of anisotropic scintillation efficiency for carbon recoils in a stilbene crystal for dark matter detection," *Phys. Lett.*, vol. B571, pp. 132–138, 2003.

[215] J. Monroe and P. Fisher, "Neutrino Backgrounds to Dark Matter Searches," *Phys.Rev.*, vol. D76, p. 033007, 2007.

[216] A. Gutlein *et al.*, "Solar and atmospheric neutrinos: Background sources for the direct dark matter search," *Astropart. Phys.*, vol. 34, pp. 90–96, 2010.

[217] J. N. Bahcall, A. M. Serenelli, and S. Basu, "New solar opacities, abundances, helioseismology, and neutrino fluxes," *Astrophys. J.*, vol. 621, pp. L85–L88, 2005.

[218] B. T. Cleveland, T. Daily, R. Davis, Jr., J. R. Distel, K. Lande, C. K. Lee, P. S. Wildenhain, and J. Ullman, "Measurement of the solar electron neutrino flux with the Homestake chlorine detector," *Astrophys. J.*, vol. 496, pp. 505–526, 1998.

[219] S. N. Ahmed *et al.*, "Measurement of the total active B-8 solar neutrino flux at the Sudbury Neutrino Observatory with enhanced neutral current sensitivity," *Phys. Rev. Lett.*, vol. 92, p. 181301, 2004.

[220] T. K. Gaisser and M. Honda, "Flux of atmospheric neutrinos," *Ann. Rev. Nucl. Part. Sci.*, vol. 52, pp. 153–199, 2002.

[221] Y. Fukuda *et al.*, "Evidence for oscillation of atmospheric neutrinos," *Phys. Rev. Lett.*, vol. 81, pp. 1562–1567, 1998.

[222] P. Adamson *et al.*, "First observations of separated atmospheric nu(mu) and anti-nu(mu) events in the MINOS detector," *Phys. Rev.*, vol. D73, p. 072002, 2006.

[223] R. Abbasi *et al.*, "Measurement of the atmospheric neutrino energy spectrum from 100 GeV to 400 TeV with IceCube," *Phys. Rev.*, vol. D83, p. 012001, 2011.

[224] J. F. Beacom, "The Diffuse Supernova Neutrino Background," *Ann.Rev.Nucl.Part.Sci.*, vol. 60, pp. 439–462, 2010.

[225] J. N. Bahcall, M. Kamionkowski, and A. Sirlin, "Solar neutrinos: Radiative corrections in neutrino - electron scattering experiments," *Phys. Rev.*, vol. D51, pp. 6146–6158, 1995.

[226] D. Z. Freedman, D. N. Schramm, and D. L. Tubbs, "The Weak Neutral Current and Its Effects in Stellar Collapse," *Ann. Rev. Nucl. Part. Sci.*, vol. 27, pp. 167–207, 1977.

[227] A. Drukier and L. Stodolsky, "Principles and Applications of a Neutral Current Detector for Neutrino Physics and Astronomy," *Phys. Rev.*, vol. D30, p. 2295, 1984.

[228] K. Scholberg, "Prospects for measuring coherent neutrino-nucleus elastic scattering at a stopped-pion neutrino source," *Phys. Rev.*, vol. D73, p. 033005, 2006.

[229] C. J. Horowitz, K. J. Coakley, and D. N. McKinsey, "Supernova observation via neutrino - nucleus elastic scattering in the CLEAN detector," *Phys. Rev.*, vol. D68, p. 023005, 2003.

[230] B. Cabrera, L. M. Krauss, and F. Wilczek, "Bolometric Detection of Neutrinos," *Phys. Rev. Lett.*, vol. 55, p. 25, 1985.

[231] A. K. Drukier, K. Freese, and D. N. Spergel, "Detecting Cold Dark Matter Candidates," *Phys. Rev.*, vol. D33, pp. 3495–3508, 1986.

[232] D. Z. Freedman, "Coherent neutrino nucleus scattering as a probe of the weak neutral current," *Phys. Rev.*, vol. D9, pp. 1389–1392, 1974.

[233] S. Tilav, P. Desiati, T. Kuwabara, D. Rocco, F. Rothmaier, M. Simmons, and H. Wissing, "Atmospheric Variations as Observed by IceCube," 2010.

[234] C. Pena-Garay and A. Serenelli, "Solar neutrinos and the solar composition problem," 2008.

[235] M. Asplund, N. Grevesse, A. J. Sauval, and P. Scott, "The chemical composition of the Sun," *Ann.Rev.Astron.Astrophys.*, vol. 47, pp. 481–522, 2009.

[236] F. L. Villante, A. M. Serenelli, F. Delahaye, and M. H. Pinsonneault, "The Chemical Composition of the Sun from Helioseismic and Solar Neutrino Data," *apj*, vol. 787, p. 13, May 2014.

[237] J. Maneira, "The SNO+ experiment: status and overview," *J.Phys.Conf.Ser.*, vol. 447, p. 012065, 2013.

[238] K. Abe, T. Abe, H. Aihara, Y. Fukuda, Y. Hayato, *et al.*, "Letter of Intent: The Hyper-Kamiokande Experiment — Detector Design and Physics Potential —," 2011.

[239] J. Billard, L. Strigari, and E. Figueroa-Feliciano, "Solar neutrino physics with low-threshold dark matter detectors," *Phys. Rev.*, vol. D91, no. 9, p. 095023, 2015.

[240] J. F. Beacom, "Supernova neutrino detection," *Nucl. Phys. Proc. Suppl.*, vol. 235-236, pp. 395–401, 2013.

[241] M. Honda, T. Kajita, K. Kasahara, and S. Midorikawa, "Improvement of low energy atmospheric neutrino flux calculation using the JAM nuclear interaction model," *Phys.Rev.*, vol. D83, p. 123001, 2011.

[242] S. Ahlen, N. Afshordi, J. Battat, J. Billard, N. Bozorgnia, *et al.*, "The case for a directional dark matter detector and the status of current experimental efforts," *Int.J.Mod.Phys.*, vol. A25, pp. 1–51, 2010.

[243] D. Santos, J. Billard, G. Bosson, J. Bouly, O. Bourrion, *et al.*, "MIMAC : A micro-tpc matrix for directional detection of dark matter," *J.Phys.Conf.Ser.*, vol. 309, p. 012014, 2011.

[244] S. Ahlen, J. Battat, T. Caldwell, C. Deaconu, D. Dujmic, *et al.*, "First Dark Matter Search Results from a Surface Run of the 10-L DMTPC Directional Dark Matter Detector," *Phys.Lett.*, vol. B695, pp. 124–129, 2011.

[245] "CygnusA: Radio Galaxy." `http://campus.pari.edu/tw/SGRA/Catalog/cygnus_a/cygnus_a.html`, 2015. Accessed: 2015-11-01.

[246] K. Freese, J. A. Frieman, and A. Gould, "Signal Modulation in Cold Dark Matter Detection," *Phys.Rev.*, vol. D37, pp. 3388–3405, 1988.

[247] A. L. Read, "Modified frequentist analysis of search results (The CL(s) method)," 2000.

[248] J. H. Davis, "Dark Matter vs. Neutrinos: The effect of astrophysical uncertainties and timing information on the neutrino floor," *JCAP*, vol. 1503, no. 03, p. 012, 2015.

[249] F. Ruppin, J. Billard, E. Figueroa-Feliciano, and L. Strigari, "Complementarity of dark matter detectors in light of the neutrino background," *Phys.Rev.*, vol. D90, no. 8, p. 083510, 2014.

[250] D. Nygren, "Columnar recombination: a tool for nuclear recoil directional sensitivity in a xenon-based direct detection WIMP search," *J.Phys.Conf.Ser.*, vol. 460, p. 012006, 2013.

[251] L. Baudis, A. Ferella, A. Kish, A. Manalaysay, T. Marrodan Undagoitia, *et al.*, "Neutrino physics with multi-ton scale liquid xenon detectors," 2013.

[252] L. Baudis, A. Ferella, A. Kish, A. Manalaysay, T. Marrodan Undagoitia, and M. Schumann, "Neutrino physics with multi-ton scale liquid xenon detectors," *JCAP*, vol. 1401, p. 044, 2014.

[253] C. A. J. O'Hare, A. M. Green, J. Billard, E. Figueroa-Feliciano, and L. E. Strigari, "Readout strategies for directional dark matter detection beyond the neutrino background," 2015.